Fraunhofer Institut Techno- und Wirtschaftsmathematik

N. Marheineke, R. Wegener

# Fiber Dynamics in Turbulent Flows

Part I: General Modeling Framework
Part II: Specific Taylor Drag

Berichte des Fraunhofer ITWM, Nr. 81 (2005)

ISSN 1434-9973

Bericht 81 (2005)



Die Veröffentlichungen in der Berichtsreihe des Fraunhofer ITWM können bezogen werden über:

Fraunhofer-Institut für Techno- und
Wirtschaftsmathematik ITWM
Gottlieb-Daimler-Straße, Geb. 49

67663 Kaiserslautern
Germany

Telefon: +49 (0) 6 31/2 05-32 42
Telefax: +49 (0) 6 31/2 05-41 39
E-Mail: info@itwm.fraunhofer.de
Internet: www.itwm.fraunhofer.de

# Vorwort

Das Tätigkeitsfeld des Fraunhofer Instituts für Techno- und Wirtschaftsmathematik ITWM umfasst anwendungsnahe Grundlagenforschung, angewandte Forschung sowie Beratung und kundenspezifische Lösungen auf allen Gebieten, die für Techno- und Wirtschaftsmathematik bedeutsam sind.

In der Reihe »Berichte des Fraunhofer ITWM« soll die Arbeit des Instituts kontinuierlich einer interessierten Öffentlichkeit in Industrie, Wirtschaft und Wissenschaft vorgestellt werden. Durch die enge Verzahnung mit dem Fachbereich Mathematik der Universität Kaiserslautern sowie durch zahlreiche Kooperationen mit internationalen Institutionen und Hochschulen in den Bereichen Ausbildung und Forschung ist ein großes Potenzial für Forschungsberichte vorhanden. In die Berichtreihe sollen sowohl hervorragende Diplom- und Projektarbeiten und Dissertationen als auch Forschungsberichte der Institutsmitarbeiter und Institutsgäste zu aktuellen Fragen der Techno- und Wirtschaftsmathematik aufgenommen werden.

Darüberhinaus bietet die Reihe ein Forum für die Berichterstattung über die zahlreichen Kooperationsprojekte des Instituts mit Partnern aus Industrie und Wirtschaft.

Berichterstattung heißt hier Dokumentation darüber, wie aktuelle Ergebnisse aus mathematischer Forschungs- und Entwicklungsarbeit in industrielle Anwendungen und Softwareprodukte transferiert werden, und wie umgekehrt Probleme der Praxis neue interessante mathematische Fragestellungen generieren.

Dieter Prätzel-Wolters

Prof. Dr. Dieter Prätzel-Wolters
Institutsleiter

Kaiserslautern, im Juni 2001

# Fiber Dynamics in Turbulent Flows I
# General Modeling Framework

Nicole Marheineke    Raimund Wegener
marheineke@itwm.fhg.de    wegener@itwm.fhg.de
Fraunhofer-Institut für Techno- und Wirtschaftsmathematik (ITWM),
Gottlieb-Daimler-Str., Geb. 49, D-67663 Kaiserslautern, Germany

July 14, 2005

**Abstract**

The paper at hand deals with the modeling of turbulence effects on the dynamics of a long slender elastic fiber. Independent of the choice of the drag model, a general aerodynamic force concept is derived on the basis of the velocity field for the randomly fluctuating component of the flow. Its construction as centered differentiable Gaussian field complies thereby with the requirements of the stochastic $k$-$\epsilon$ turbulence model and Kolmogorov's universal equilibrium theory on local isotropy.

**Keywords:** Fiber-fluid interaction; Cosserat rod; Turbulence modeling; Kolmogorov's energy spectrum; Double-velocity correlations; Differentiable Gaussian fields

**AMS Classification:** 74F10, 76F60, 76F05, 60H40

## 1 Introduction

The understanding of fiber-fluid interactions is of great interest for research, development and production in the textiles manufacturing. In the melt-spinning process of nonwoven materials, hundreds of individual endless fibers being obtained by continuous extrusion of a melted polymer are stretched and entangled by highly turbulent air flows to finally form a web. The quality of this web and the resulting nonwoven material depends essentially on the dynamics of the fibers.

Fiber-turbulence interaction is hereby a complex phenomenon that is governed by many factors, including nature of flow field, turbulent length scales, concentration and size of fibers. Thin fibers decrease the turbulent intensity by increasing the apparent viscosity, whereas fibers whose thickness induces Reynolds numbers greater than some critical one intensify the turbulence due to vortex shedding [4]. Both mechanisms are strongly affected by the concentration. In the considered application, however, the turbulence is not significantly influenced by the fibers. Hence, the turbulent flow is here determined under neglect of suspended fibers, and its effect is theoretically studied on a single long, slender fiber using a general drag model.

The fiber dynamics is described by the Kirchhoff-Love equations for the motion of a Cosserat rod capable of large bending deformations in Sec 2. In terms of these the fiber slenderness allows the formulation of a wavelike system of nonlinear PDEs of $4^{\text{th}}$ order with the algebraic constraint of inextensibility. The behavior of this system relies on the model for the external force imposed on the fiber by the turbulent flow, in particular on the choice of the air drag coefficients. The modeling of a generally valid aerodynamic force in Sec 4 is based on the splitting of the flow velocity into mean and fluctuation part in the Reynolds-averaged Navier-Stokes equations. Thus, a centered differentiable Gaussian field for the randomly fluctuating component of the flow velocity is derived under the Global-from-Local Assumption of underlying locally isotropic and homogeneous turbulence in Sec 3. The construction of the initial condition for the respective local double-velocity correlation tensors satisfies thereby Kolmogorov's universal equilibrium theory as well as the local distribution of kinetic energy $k$ and dissipation $\epsilon$ provided by the stochastic $k$-$\epsilon$ turbulence model. The dynamic behavior of the local correlation tensors is described by an advection equation whose solution coincides with Taylor's hypothesis of frozen turbulence pattern.

The temporal change of the global coherences is included by the averaging procedure. In Sec 4 the developed local velocity fluctuation fields hand their properties to the corresponding correlated local stochastic forces along the fiber. Gluing them together yields the global aerodynamic force that represents the turbulence effects on the fiber motion. Considering a wide class of feasible air drag models, the stated Global-from-Local Force Concept in combination with a linearization ansatz enables a good $\mathcal{L}^2$ and $\mathcal{L}^\infty$-approximation of the correlated force by Gaussian white noise with flow-dependent amplitude in case of a macroscopic description of the fiber.

# 2 Fiber Dynamics

In the actual spinning process the fiber is endless and its deposition plays a crucial role for the generation of the nonwoven material. However, as this paper focuses exclusively on the description of its dynamics due to the turbulent flow, the following considerations are restricted on a long slender elastic polymer fiber that is fixed with one end, suspended in a highly turbulent air stream. Let $l$ denote its length and $d$ its diameter with slenderness ratio $\delta = d/l \ll 1$. To describe its motion an 1D-model is derived on the dynamical Kirchhoff-Love theory for a Cosserat rod being capable of large, geometrically nonlinear deformations [2].

## 2.1 Equations of Motion

Treat the fiber in the reference configuration as body $\mathcal{B}$ given within a fixed Cartesian frame $\mathbf{e_1}, \mathbf{e_2}, \mathbf{e_3}$. Define $\mathbf{p}(\mathbf{z}, t)$ to be the position of the material point $\mathbf{z} \in \mathcal{B}$ at time $t$, then $\mathbf{p}(., t)$ states the actual configuration of the closure $\mathrm{cl}\mathcal{B}$ of $\mathcal{B}$ at time $t$. Introduce the curvilinear coordinates $\mathbf{x} := (x_1, x_2, s) \in \mathbb{R}\times\mathbb{R}\times[0, l]$ on $\mathcal{B}$ with $s$ denoting the arc length. Then define $\tilde{\mathbf{p}}(\mathbf{x}, t) := \mathbf{p}(\tilde{\mathbf{z}}(\mathbf{x}), t)$ where $\tilde{\mathbf{z}}$ assigns $\mathbf{z} \in \mathrm{cl}\,\mathcal{B}$ to each $\mathbf{x}$. In particular, $\tilde{\mathbf{p}}(., ., s, t)$ describes the actual configuration of the cross-section $\mathcal{B}(s)$ at time $t$.

The fiber model is now developed under the assumption that the position field $\tilde{\mathbf{p}}$ is determined by three vector-valued functions $\mathbf{r}(s, t)$, $\mathbf{d_1}(s, t)$ and $\mathbf{d_2}(s, t)$, i.e.

$$\tilde{\mathbf{p}}(\mathbf{x}, t) = \mathbf{r}(s, t) + \mathbf{j}(\mathbf{r}(s, t), \mathbf{d_1}(s, t), \mathbf{d_2}(s, t), \mathbf{x}, t), \tag{1}$$

where the fiber line $\mathbf{r}(s, t)$ might be interpreted as the actual configuration of the center line at time $t$ and the orthonormal directors $\mathbf{d_1}(s, t)$ and $\mathbf{d_2}(s, t)$ state the orientation of the actual configuration of $\mathcal{B}(s)$ at time $t$. Let additionally $\mathbf{d_3}(s, t) = \mathbf{d_1}(s, t) \times \mathbf{d_2}(s, t)$. In terms of these functions, the feasible deformations of the fiber, e.g. flexure $\kappa_1, \kappa_2$, torsion $\tau$, shear $w_1, w_2$ and dilatation $w_3$, are then expressed using the relations $\partial_s \mathbf{d_i} = \mathbf{b} \times \mathbf{d_i}$, $\mathbf{b} = \kappa_1 \mathbf{d_1} + \kappa_2 \mathbf{d_2} + \tau \mathbf{d_3}$ and $\partial_s \mathbf{r} = \sum_{i=1}^3 w_i \mathbf{d_i}$. Thus,

$$\begin{aligned} &\kappa_1 = -\mathbf{d_2} \cdot \partial_s \mathbf{d_3}, \quad \kappa_2 = -\mathbf{d_3} \cdot \partial_s \mathbf{d_1}, \quad \tau = -\mathbf{d_1} \cdot \partial_s \mathbf{d_2}, \\ &w_i = \partial_s \mathbf{r} \cdot \mathbf{d_i}. \end{aligned}$$

According to Bernoulli's hypothesis that cross-sections never experience warping as consequence of deformation, the function $\mathbf{j}$ of Eq (1) can moreover be prescribed by $\mathbf{j}(\mathbf{r}, \mathbf{d_1}, \mathbf{d_2}, \mathbf{x}, t) = x_1 \mathbf{d_1} + x_2 \mathbf{d_2}$. Assuming the reference configuration $\mathcal{B}$ to be a homogeneous (with respect to the density distribution), cylindrical body with circular cross-sections of constant radius, the linear and angular impulse-momentum laws for $\mathcal{B}$ read [2]

$$\partial_s \mathbf{q} + \mathbf{f} = \rho A \partial_{tt} \mathbf{r}, \tag{2}$$

$$\partial_s \mathbf{m} + \partial_s \mathbf{r} \times \mathbf{q} + \mathbf{l} = \rho I \sum_{i=1}^{2} (\partial_{tt} \mathbf{d_i} \times \mathbf{d_i}). \tag{3}$$

Here, $\rho$ denotes density, $A = \pi d^2/4$ cross-sectional area and $I = \pi d^4/64$ moment of inertia. Closing the system by means of constitutive laws for inner force $\mathbf{q}$ and moment $\mathbf{m}$ as well as given outer line force $\mathbf{f}$ and moment $\mathbf{l}$, the Kirchhoff-Love equations (2), (3) yield the description for fiber line and directors $\mathbf{r}$, $\mathbf{d_1}$, $\mathbf{d_2}$. The orthonormality of $\mathbf{d_1}$ and $\mathbf{d_2}$ reduces hereby the number of unknowns down to six. As no outer moment is acting on the fiber, $\mathbf{l} = \mathbf{0}$.

Constitutive laws for elastic materials look in general like

$$\mathbf{m} = \mathbf{M}(\kappa_1, \kappa_2, \tau, w_1, w_2, w_3, s), \quad \mathbf{q} = \mathbf{Q}(\kappa_1, \kappa_2, \tau, w_1, w_2, w_3, s).$$

We apply here in particular Bernoulli-Euler beam theory that the inner moment $\mathbf{m}$ arises due to bending and torsion

$$\mathbf{m} = EI(\kappa_1 \mathbf{d_1} + \kappa_2 \mathbf{d_2}) + GJ\tau \mathbf{d_3} \tag{4}$$

with Young's modulus $E$, shear modulus $G$, polar moment of inertia $J = \pi d^4/32$. Moreover, we interpret $\mathbf{q}$ as vectorial Lagrangian multiplier and impose instead of a material law for $\mathbf{q}$ the following constraints on $\mathbf{d_3}$ and $\partial_s \mathbf{r}$

$$\mathbf{d_3} = \frac{\partial_s \mathbf{r}}{\|\partial_s \mathbf{r}\|_2}, \quad \|\partial_s \mathbf{r}\|_2 = 1. \tag{5}$$

This excludes shear and extensional deformation from the model. The restrictions are reasonable for a long slender fiber because shear and elongation are negligibly small in comparison to bending.

Apart from this, the slenderness enables a further simplification of system (2), (3). Non-dimensionalizing Eq (3) yields $\partial_s \mathbf{m} + \partial_s \mathbf{r} \times \mathbf{q} = \delta^2 D \sum_{i=1}^{2} (\partial_{tt}^2 \mathbf{d_i} \times \mathbf{d_i})$ with negligibly small right hand side as the slenderness ratio $\delta$ satisfies $\delta \ll 1$ and $D = \mathcal{O}(1)$. Setting the right hand side to zero, i.e.

$$\partial_s \mathbf{m} + \partial_s \mathbf{r} \times \mathbf{q} = \mathbf{0}, \tag{6}$$

and using Eq (5) we obtain $\partial_s \tau = 0$. Consequently, the torsion over the whole fiber equals the introduced torsion at the ends $\tau = \tau_0$. Rewriting Eq (4) gives thus $\mathbf{m} = EI(\mathbf{d_3} \times \partial_s \mathbf{d_3}) + GJ\tau_0 \mathbf{d_3}$ where $\partial_s \mathbf{d_3}$ represents the curvature vector $\partial_{ss}\mathbf{r} = \kappa\, \mathbf{n}$ with $\kappa = \sqrt{\kappa_1^2 + \kappa_2^2}$ and $\mathbf{n}$ normal vector. Splitting the inner force $\mathbf{q}$ into tangential and normal part with respect to the fiber position yields

$$\begin{aligned}
\mathbf{q} &= (\mathbf{q} \cdot \mathbf{d_3})\, \mathbf{d_3} + \mathbf{d_3} \times (\mathbf{q} \times \mathbf{d_3}) \\
&\overset{(6)}{=} (\mathbf{q} \cdot \mathbf{d_3} + EI\, (\partial_{ss}\mathbf{d_3} \cdot \mathbf{d_3}))\, \mathbf{d_3} - EI\, (\mathbf{d_3} \cdot \mathbf{d_3})\, \partial_{ss}\mathbf{d_3} + GJ\tau_0\, \mathbf{d_3} \times \partial_s \mathbf{d_3}.
\end{aligned}$$

Defining

$$\begin{aligned}
T :=&\ \mathbf{q} \cdot \mathbf{d_3} + EI\, (\partial_{ss}\mathbf{d_3} \cdot \mathbf{d_3}) \\
\overset{(5)}{=}&\ \underbrace{\mathbf{q} \cdot \partial_s \mathbf{r}}_{\text{tension}} - \underbrace{EI\, \|\partial_{ss}\mathbf{r}\|_2^2}_{\text{curvature due to bending}},
\end{aligned}$$

as modified tractive force, $\mathbf{q}$ depends exclusively on fiber line $\mathbf{r}$ and scalar Lagrangian multiplier $T$, and thus two more degrees of freedom vanish which is consistent with the removing of the unknown directors $\mathbf{d_i}$. Plugging

$$\partial_s \mathbf{q} \overset{(5)}{=} \partial_s (T\, \partial_s \mathbf{r}) - EI\ \partial_{ssss}\mathbf{r} + GJ\tau_0\, \partial_s \mathbf{r} \times \partial_{sss}\mathbf{r}$$

into Eq (2), the dynamics of a freely swinging fiber that is fixed at one end (cf. Fig 1) is described by

$$\begin{aligned}
\rho A\, \partial_{tt}\mathbf{r}(s,t) = &\ \partial_s [T(s,t)\, \partial_s \mathbf{r}(s,t)] - EI\, \partial_{ssss}\mathbf{r}(s,t) + GJ\tau_0\, \partial_s \mathbf{r}(s,t) \times \partial_{sss}\mathbf{r}(s,t) \\
&+ \mathbf{f}^{grav} + \mathbf{f}^{air}(\mathbf{r}(.), s, t), \qquad (7) \\
\|\partial_s \mathbf{r}(s,t)\|_2 = 1, \qquad (8)
\end{aligned}$$

for $(s,t) \in (0,l) \times \mathbb{R}^+$ with Dirichlet conditions at the fixed end ($s = l$) and Neumann at the free one ($s = 0$)

$$\begin{aligned}
\mathbf{r}(l,t) &= \mathbf{0}, & \partial_{ss}\mathbf{r}(0,t) &= \mathbf{0}, \\
\partial_s \mathbf{r}(l,t) &= \mathbf{e_3}, & \partial_{sss}\mathbf{r}(0,t) &= \mathbf{0}, \\
& & T(0,t) &= 0
\end{aligned}$$

as well as appropriate initial conditions ($t = 0$), e. g.

$$\mathbf{r}(s,0) = (s - l)\, \mathbf{e_3} \qquad \partial_t \mathbf{r}(s,0) = \mathbf{0}.$$

The Neumann conditions might be interpreted as natural boundary conditions, the ending $s = 0$ is free of stress. Thus, neither outer moment nor force are acting on it. Moreover, $T(0,t)$ viewed

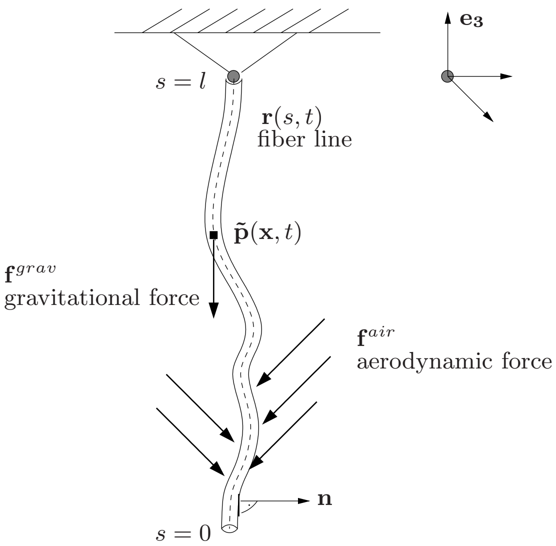


Figure 1: Fiber dynamics caused by external forces

as tractive force vanishes. The Lagrangian multiplier $T(s,t)$ is thereby related to the algebraic constraint (8) of conservation of length. The behavior of our fiber system (7), (8) – but definitely also of the original one (2), (3) – is strongly affected by the external line forces that arise due to gravitational $\mathbf{f}^{grav} = \rho A\,\mathbf{g}$ and aerodynamic forces $\mathbf{f}^{air}$. We prescribe the aerodynamic force as function depending on arc length $s$, time $t$ and additionally on the fiber line $\mathbf{r} : [0,l] \times \mathbb{R}_0^+ \to \mathbb{R}^3$ in a functional sense.

In this work, we initially introduce no twisting at the fiber ends, $\tau_0 = 0$, such that Eq (7) simplifies to a wavelike system of nonlinear partial differential equations of $4^{\text{th}}$ order, if the feasible functional dependence of the aerodynamic force is localized on the fiber point, e.g. $\mathbf{f}^{air}(\mathbf{r}(.), s, t) = \mathbf{f}^{air}(\mathbf{r}(s,t), \partial_s \mathbf{r}(s,t), \partial_t \mathbf{r}(s,t), s, t)$.

## 2.2 Air Drag

The description of the fiber dynamics in a turbulent flow relies essentially on the model for the aerodynamic force $\mathbf{f}^{air}$ that is imposed on the fiber by the fluid. Neglecting the fiber influence on the flow, a dimensionless air drag coefficient $c^{drag}$ based on Reynolds (Re), Mach and Froude number can be associated to $\mathbf{f}^{air}$ [14]. If just frictional and inertial forces occur in the flow around the fiber, $c^{drag}$ is particularly determined by

$$c^{drag} = \frac{\|\mathbf{f}^{air}\|_2}{0.5\,\rho^{air}\,d\,\|\mathbf{v}\|_2^2}$$

with air density $\rho^{air}$, fiber diameter $d$ and relative velocity between fluid flow and fiber $\mathbf{v} = \mathbf{u} - \partial_t \mathbf{r}$. Thus, the magnitude of the line force is proportional to Bernoulli's dynamic pressure $p = 0.5\rho^{air}\|\mathbf{v}\|_2^2$ acting along $d$. In general, we characterize a feasible air drag model by a function $\mathbf{f} : \mathbb{R}^3 \times \mathbb{R}^2 \to \mathbb{R}^3$ depending on a given velocity and a normalized direction. In this context, the aerodynamic force of Eq (7) reads

$$\mathbf{f}^{air}(\mathbf{r}(.), s, t) = \mathbf{f}(\mathbf{u}(\mathbf{r}(s,t),t) - \partial_t \mathbf{r}(s,t), \partial_s \mathbf{r}(s,t)) \tag{9}$$

where the flow velocity $\mathbf{u} : \mathbb{R}^3 \times \mathbb{R}_0^+ \to \mathbb{R}^3$ acts as outer input parameter to the fiber problem. However, as this instantaneous flow velocity is not available from a stochastic description of a turbulent flow, we derive a concept for a random Gaussian aerodynamic force in this work. Note that this concept utilizes exclusively the functional relation $\mathbf{f}$ and is hence generally applicable to a wide class of air drag models.

## 3 Model for Velocity Fluctuation Field

Consider the flow to be subsonic, highly turbulent with small pressure gradients and Mach number $\mathrm{Ma} < 1/3$. Then it can be modeled as an incompressible Newtonian fluid using the incompressible Navier-Stokes equations (NSE). Solving NSE by means of Direct Numerical Simulation (DNS) gives the exact velocity field needed for the determination of the force of Eq (9). However, DNS presupposes the resolution of all vortices ranging from the large energy-bearing ones of length $l_\mathrm{T}$ to the smallest, viscously determined Kolmogorov vortices of size $\eta$ with $l_\mathrm{T}/\eta = \mathrm{Re}^{3/4}$ [16]. Therefore, the number of grid points that are required for the refinement of a 3D domain is proportional to $\mathrm{Re}^{9/4}$. Though recent high speed performances, DNS is thus still restricted to simple, small Reynolds number flow. The stochastic turbulence models in contrast represent a reasonable compromise between accuracy and computational efficiency [5]. They are based on the Reynolds-averaged Navier-Stokes equations (RANS) where the instantaneous velocity $\mathbf{u} : \mathbb{R}^3 \times \mathbb{R}_0^+ \to \mathbb{R}^3$ is expressed as sum of a mean $\bar{\mathbf{u}}$ and a fluctuating part $\mathbf{u}'$

$$\mathbf{u}(\mathbf{x}, t) = \bar{\mathbf{u}}(\mathbf{x}, t) + \mathbf{u}'(\mathbf{x}, t).$$

Applying in particular the standard $k$-$\epsilon$ model [10] yields a deterministic description of mean velocity $\bar{\mathbf{u}} : \mathbb{R}^3 \times \mathbb{R}_0^+ \to \mathbb{R}^3$, turbulent kinetic energy $k : \mathbb{R}^3 \times \mathbb{R}_0^+ \to \mathbb{R}^+$ and dissipation rate $\epsilon : \mathbb{R}^3 \times \mathbb{R}_0^+ \to \mathbb{R}^+$. Hereby, the variables $k$ and $\epsilon$ might be interpreted as parameters of a $\mathbb{R}^3$-valued differentiable random field representing the fluctuations $(\mathbf{u}'_{\mathbf{x},t}, (\mathbf{x}, t) \in \mathbb{R}^3 \times \mathbb{R}_0^+)$

$$k(\mathbf{x}, t) = \frac{1}{2}\, \mathbb{E}[\mathbf{u}'(\mathbf{x}, t) \cdot \mathbf{u}'(\mathbf{x}, t)], \tag{10}$$

$$\epsilon(\mathbf{x}, t) = \nu\, \mathbb{E}[\nabla \mathbf{u}'(\mathbf{x}, t) : \nabla \mathbf{u}'(\mathbf{x}, t)]. \tag{11}$$

To conform the notations of probability theory and turbulence literature, note that the mean $\mathbb{E}[\mathbf{u}']$ equals the averaged quantity $\overline{\mathbf{u}'}$. Constructing a suitable fluctuation field requires the analysis of the turbulent behavior of the flow which is characterized by means of statistic quantities, i.e. double-velocity correlations revealing spatial and temporal relations within a domain.

**Definition 1 (Velocity Fluctuation Field)**
*Let $(\Omega, \mathcal{A}, \mathrm{P})$ be a probability space. The velocity fluctuation field of a turbulent flow is said to be a centered $\mathbb{R}^3$-valued random field $(\mathbf{\Phi}_{\mathbf{x},t}, (\mathbf{x}, t) \in \mathbb{R}^3 \times \mathbb{R}_0^+)$ with $\mathbf{\Phi}_{\mathbf{x},t} \in \mathcal{L}^2(\Omega, \mathcal{A}, \mathrm{P})$. Its correlation tensor reads*

$$\mathbf{\Gamma}(\mathbf{x}, t, \mathbf{y}, \tau) = \mathbb{E}[\mathbf{\Phi}(\mathbf{x}, t) \otimes \mathbf{\Phi}(\mathbf{y}, \tau)].$$

Classifying turbulence, we face shear turbulence in practice. Although it can be simulated via RANS models, this kind of flow is hardly understood. Physical interpreting and mathematical handling of the statistic quantities is extremely difficult. Therefore, it is helpful to consider approximations like homogeneous and/or isotropic turbulent flows. Isotropy has obviously a hypothetical character, but knowledge of its characteristics form a fundamental basis for the study of actual, anisotropic turbulent flows. Certain theoretical considerations concerning the energy transfer through the eddy-size spectrum from the larger to the smaller eddies lead to the conclusion that the fine structure of anisotropic turbulent flows is almost isotropic, Kolmogorov's local isotropy hypothesis [7]. Thus, many features of isotropic turbulence apply to phenomena in actual turbulence that are mainly determined by the fine-scale structure. Even if we consider the anisotropic large-scale structure of an actual turbulence, it is possible to treat such a turbulence for purposes of a first approximation as isotropic. The differences are mostly sufficiently small [8]. As velocity fluctuations in an isotropic flow are Gaussian [6], we restrict to Gaussian flows that are uniquely determined by their correlation tensor. This motivates our

**Global-from-Local Assumption**
*Let $(\Omega, \mathcal{A}, \mathrm{P})$ be a probability space. Let $\{(\mathbf{w}^{\mathbf{y},\tau}_{\mathbf{x},t}, (\mathbf{x}, t) \in \mathbb{R}^3 \times \mathbb{R}_0^+), (\mathbf{y}, \tau) \in \mathbb{R}^3 \times \mathbb{R}_0^+\}$ be a family of local velocity fluctuation fields that correspond to spatially and temporally homogeneous, isotropic and incompressible Gaussian flows with respect to the points $(\mathbf{y}, \tau)$. Let $\tilde{\boldsymbol{\gamma}}^{\mathbf{y},\tau} : (\mathbb{R}^3 \times \mathbb{R}_0^+)^2 \to \mathbb{R}^{3\times 3}$ denote their respective correlation tensors. For each local field the quantities $k = k(\mathbf{y}, \tau)$, $\epsilon = \epsilon(\mathbf{y}, \tau)$ and $\bar{\mathbf{u}} = \bar{\mathbf{u}}(\mathbf{y}, \tau)$ are taken as constant. Then we assume that our actual global fluctuation field $\mathbf{u}'$ can be constructed as*

$$\mathbf{u}'(\mathbf{x}, t) =< \mathbf{w}^{\mathbf{y},\tau}(\mathbf{x}, t) >_{M(\mathbf{x},t)} \tag{12}$$

*with* $M(\mathbf{x},t) = \{(\mathbf{y},\tau) \in \mathbb{R}^3 \times \mathbb{R}_0^+ \,|\, \|\mathbf{x}-\mathbf{y}-\bar{\mathbf{u}}(\mathbf{x},t)(t-\tau)\|_2 \leq l_\mathrm{T} \wedge |t-\tau| \leq t_\mathrm{T}\}$, $|M(\mathbf{x},t)| = \int_{M(\mathbf{x},t)} d\mathbf{y}\, d\tau$ *and turbulent large-scale length* $l_\mathrm{T}$ *and time* $t_\mathrm{T}$. *The brackets* $< . >$ *represent the Gaussian average that is uniquely prescribed by expectation and covariance resp. correlations according to*

$$
\begin{aligned}
\mathbb{E}[\mathbf{u}'(\mathbf{x},t)] &= \frac{1}{|M(\mathbf{x},t)|} \int\limits_{M(\mathbf{x},t)} \mathbb{E}[\mathbf{w}^{\mathbf{y},\tau}(\mathbf{x},t)]\; d\mathbf{y}\, d\tau = \mathbf{0} \\
\mathrm{Cov}(\mathbf{u}'(\mathbf{x_1},t_1), \mathbf{u}'(\mathbf{x_2},t_2)) &= \frac{1}{\sqrt{|M(\mathbf{x_1},t_1)||M(\mathbf{x_2},t_2)|}} \iint\limits_{M(\mathbf{x_1},t_1)\cap M(\mathbf{x_2},t_2)} \tilde{\gamma}^{\mathbf{y},\tau}(\mathbf{x_1},t_1,\mathbf{x_2},t_2)\; d\mathbf{y}\, d\tau \\
&= \mathbf{\Gamma}'(\mathbf{x_1},t_1,\mathbf{x_2},t_2).
\end{aligned}
$$

Note that the used terminology is explained in the course of this section. The construction rule (12) enables the realization of a globally inhomogeneous and anisotropic turbulent flow on the basis of a very limited number of data stemming from general turbulence theory and specific, case-dependent $k$-$\epsilon$ simulations. So far, it was not clear at all, if such a differentiable turbulent field exists. The underlying local fluctuation fields $\mathbf{w}^{\mathbf{y},\tau}$ that can be interpreted as fine-scale structure of the turbulence satisfy Kolmogorov's local isotropy hypothesis as well as the local kinetic energy $k$ and dissipation $\epsilon$ distribution of the $k$-$\epsilon$ model. Averaging their statistical parameters over a region $M$ where the local stochastic quantities only slightly differ glues them together to the global fluctuation field $\mathbf{u}'$, the anisotropic large-scale structure. The respective global quantities $k_{\mathbf{u}'}$ and $\epsilon_{\mathbf{u}'}$ are thus prescribed as averages of the hardly varying local ones. This is indicated by using the turbulent large-scale length $l_\mathrm{T}$ and time $t_\mathrm{T}$. Presuming global homogeneity, the global and local quantities coincide and obey Eqs (10), (11) as desired.

In the following, we deal with the generation of the centered local fluctuation fields by modeling their correlation tensors. Therefore we skip the superscript denoting the respective point. To determine the temporal behavior of the correlations, we firstly construct an initial condition for the correlation tensor satisfying the assumptions of homogeneity and isotropy as well as the requirements of the $k$-$\epsilon$ model and Kolmogorov's energy spectrum, Sec 3.1-3.4. This initial condition meets the smoothness demands and guarantees the differentiability of the actual global field. Then we formulate an advection equation for the dynamics whose solution coincides with Taylor's hypothesis of frozen turbulence, Sec 3.5. In Sec 3.6 we finally formulate the global fluctuation field as Ito-integral over the local fields which yields the positive definite correlation tensor proposed in the Global-from-Local Assumption.

## 3.1 Locally Homogeneous, Isotropic Turbulence

**Definition 2 (Homogeneous Turbulence)**
*Let* $(\Omega, \mathcal{A}, \mathrm{P})$ *be a probability space. Let* $(\mathbf{\Phi}_{\mathbf{x},t}, (\mathbf{x},t) \in \mathbb{R}^3 \times \mathbb{R}_0^+)$ *be a velocity fluctuation field with correlation tensor* $\mathbf{\Gamma}$. *A turbulent flow is said to be spatially homogeneous if* $\mathbf{\Gamma}$ *is invariant regarding spatial translations, i.e.*

$$\mathbf{\Gamma}(\mathbf{x},t,\mathbf{y},\tau) = \mathbf{\Gamma}(\mathbf{x}-\mathbf{a},t,\mathbf{y}-\mathbf{a},\tau) \quad \forall\, \mathbf{a} \in \mathbb{R}^3.$$

*A turbulent flow is said to be temporally homogeneous if* $\mathbf{\Gamma}$ *is invariant regarding time shifts, i.e.*

$$\mathbf{\Gamma}(\mathbf{x},t,\mathbf{y},\tau) = \mathbf{\Gamma}(\mathbf{x},t-a,\mathbf{y},\tau-a) \quad \forall\, a \in \mathbb{R}.$$

**Definition 3 (Isotropic Turbulence)**
*Let* $(\Omega, \mathcal{A}, \mathrm{P})$ *be a probability space. Let* $(\mathbf{\Phi}_{\mathbf{x},t}, (\mathbf{x},t) \in \mathbb{R}^3 \times \mathbb{R}_0^+)$ *be a velocity fluctuation field with correlation tensor* $\mathbf{\Gamma}$. *A turbulent flow is said to be isotropic if* $\mathbf{\Gamma}$ *is invariant regarding rotations and reflections, i.e.*

$$\mathbf{\Gamma}(\mathbf{x},t,\mathbf{y},t) = \mathbf{S}\; \mathbf{\Gamma}(\mathbf{S}^{-1}\mathbf{x},t,\mathbf{S}^{-1}\mathbf{y},t)\; \mathbf{S}^t \quad \forall\, \mathbf{S} \in \mathcal{O}(3). \tag{13}$$

The correlation tensor $\tilde{\gamma}$ corresponding to a local fluctuation field $\mathbf{w}$, $\tilde{\gamma}(\mathbf{x},t,\mathbf{y},\tau) = \mathbb{E}[\mathbf{w}(\mathbf{x},t) \otimes \mathbf{w}(\mathbf{y},\tau)]$, depends only on the spatial and temporal difference of its arguments due to homogeneity. Thus, we define

$$\gamma(\mathbf{z},\varsigma) = \tilde{\gamma}(\mathbf{x}+\mathbf{z},t+\varsigma,\mathbf{x},t). \tag{14}$$

To derive the structure of the initial correlation tensor in the following, we focus now on

$$\boldsymbol{\gamma}_0(\mathbf{z}) = \boldsymbol{\gamma}(\mathbf{z}, 0) \quad \text{or} \quad \tilde{\boldsymbol{\gamma}}_0(\mathbf{x}, \mathbf{y}) = \tilde{\boldsymbol{\gamma}}(\mathbf{x}, t, \mathbf{y}, t).$$

**Properties of the Initial Correlation Tensor**
*The correlation tensor corresponding to an homogeneous, isotropic turbulent flow has the following properties:*

$$\boldsymbol{\gamma}_0(\mathbf{z}) = \boldsymbol{\gamma}_0(-\mathbf{z}) \tag{15}$$

$$\boldsymbol{\gamma}_0(\mathbf{z}) \quad \textit{symmetric} \tag{16}$$

$$\boldsymbol{\gamma}_0(\mathbf{0}) = c\mathbf{I}, \quad c \neq 0 \tag{17}$$

$$\boldsymbol{\gamma}_0(\mathbf{z}) \quad \textit{has two different eigenvalues:} \tag{18}$$

$$c_1(z) \textit{ in } \frac{\mathbf{z}}{z} \textit{ and } c_2(z) \textit{ in the respective normal plane.}$$

$$\boldsymbol{\gamma}_0(\mathbf{z}) = \frac{c_1(z) - c_2(z)}{z^2} \mathbf{z} \otimes \mathbf{z} + c_2(z)\mathbf{I}, \quad z = \|\mathbf{z}\|_2 \tag{19}$$

Hereby, the symmetry of $\boldsymbol{\gamma}_0$ (16) results directly from its definition and the permutability of the arguments (15) that is concluded from the translation and reflection invariance. Applying additionally rotation invariance yields Eq (17) and Eq (18). The general form (19) is deduced from the spectral theorem using the eigenvalues of Eq (18).

The one-dimensional functions $c_1$ and $c_2 \in \mathcal{C}^\infty(\mathbb{R}_0^+)$ can be interpreted as longitudinal and lateral correlation [8]. In general $c_1 \neq c_2$, but for $z \to 0$ we have $c_2(z) \to c_1(z) \to c$ with $c$ given in Eq (17).

As a turbulent flow contains a continuous spectrum of scales, it is convenient to introduce the spectral density $\mathbf{M}$ depending on the wave vector $\boldsymbol{\kappa}$. Assuming absolute Lebesgue-continuity of the spectrum of the underlying fluctuation velocity field [3], the spectral density $\mathbf{M}$ is the Fourier transform of the correlation tensor $\boldsymbol{\gamma}_0$

$$\mathbf{M}(\boldsymbol{\kappa}) = \frac{1}{(2\pi)^3} \int_{\mathbb{R}^3} e^{-i\mathbf{z}\cdot\boldsymbol{\kappa}} \boldsymbol{\gamma}_0(\mathbf{z})\, d\mathbf{z}. \tag{20}$$

Then, the spectral energy distribution (energy spectrum) $E$ is defined by

$$E(\kappa) = \frac{1}{2}\kappa^2 \oint_{S^2} \operatorname{tr}(\mathbf{M}(\kappa\mathbf{e}))\, d\mathbf{e} \tag{21}$$

with $\kappa = \|\boldsymbol{\kappa}\|_2$, unit sphere $S^2$ and unit vector $\mathbf{e} \in S^2$.

**Properties of the Spectral Density**
*The spectral density corresponding to an homogeneous, isotropic turbulent flow has the following properties:*

$$\mathbf{M}(\boldsymbol{\kappa}) = \frac{e_1(\kappa) - e_2(\kappa)}{\kappa^2} \boldsymbol{\kappa} \otimes \boldsymbol{\kappa} + e_2(\kappa)\mathbf{I} \tag{22}$$

$$\operatorname{tr}\mathbf{M}(\kappa) = \frac{1}{2\pi} \frac{E(\kappa)}{\kappa^2}. \tag{23}$$

Due to the Fourier relation (20), $\mathbf{M}$ inherits the isotropic property (13) from $\boldsymbol{\gamma}_0$ and has therefore an analogous representation with the one-dimensional spectral functions $e_1$, $e_2 \in \mathcal{C}^\infty(\mathbb{R}_0^+)$. The connection (23) between trace $\operatorname{tr}\mathbf{M}$ and energy spectrum $E$ can be concluded from Eq (21). Because of isotropy the sphere integral becomes $\int_{S^2} \operatorname{tr}(\mathbf{M}(\kappa\mathbf{e}))d\mathbf{e} = 4\pi \operatorname{tr}\mathbf{M}(\kappa)$.

In our case of an incompressible local flow field $\mathbf{w}$, the presented characteristics and dependencies of correlation and spectral functions can be simplified which halves the number of unknowns and results in a well-structured Sine-Fourier relation between $c_1$ and $E$.

**Influence of Incompressibility on Correlations and Spectral Density**
*Assuming incompressibility, the following relation for the correlation functions $c_1$ and $c_2 : \mathbb{R}_0^+ \to \mathbb{R}$ is valid:*

$$c_1(z) + \frac{z}{2}\partial_z c_1(z) = c_2(z). \tag{24}$$

*Moreover, the spectral functions $e_1$ and $e_2 : \mathbb{R}_0^+ \to \mathbb{R}$ are given by*

$$e_1(\kappa) = 0, \qquad e_2(\kappa) = \frac{1}{4\pi}\frac{E(\kappa)}{\kappa^2}. \tag{25}$$

Relation (24) is concluded from the incompressibility using

$$\mathbf{0} = \mathbb{E}[(\nabla_{\mathbf{x}} \cdot \mathbf{w}(\mathbf{x},t))\, \mathbf{w}(\mathbf{y},t)] = \nabla_{\mathbf{x}} \cdot \tilde{\gamma}_0(\mathbf{x},\mathbf{y}) \overset{\mathbf{z}:=\mathbf{x}-\mathbf{y}}{=} \nabla_{\mathbf{z}} \cdot \boldsymbol{\gamma}_0(\mathbf{z})$$

and substituting Eq (19). Analogously to the correlation functions, the number of unknown spectral functions can be reduced to one. In particular, Eq (25) is deduced by combining $\mathbf{0} = \nabla_{\mathbf{z}} \cdot \boldsymbol{\gamma}_0(\mathbf{z}) = i \int_{\mathbb{R}^3} e^{i\boldsymbol{\kappa}\cdot\mathbf{z}}\, \mathbf{M}(\boldsymbol{\kappa})\boldsymbol{\kappa}\, d\boldsymbol{\kappa}$ and thus $\mathbf{M}(\boldsymbol{\kappa})\boldsymbol{\kappa} = \mathbf{0}$ for all $\boldsymbol{\kappa} \in \mathbb{R}^3$ with Eq (23).

For an incompressible isotropic and homogeneous turbulent flow, the correlation tensor $\boldsymbol{\gamma}_0$ of $2^{\text{nd}}$ order can thus be expressed by the single one-dimensional correlation function $c_1$. In particular,

$$\mathrm{tr}\boldsymbol{\gamma}_0(z) = 3c_1(z) + z\,\partial_z c_1(z) = \frac{1}{z^2}\,\partial_z\,(z^3\, c_1(z)). \tag{26}$$

Consequently, the whole local fluctuation velocity field is uniquely determined by $c_1$ whose relation to $E$ will be useful for the further realization of the initial correlations.

**Relation between Correlation Function and Energy Spectrum**
*Let $c_1$ be the correlation function and $E$ the energy spectrum corresponding to an homogeneous, isotropic and incompressible turbulent flow. This implies their finiteness over the whole definition range. Then the following relations are valid:*

$$c_1(z) = \frac{2}{z^3}\int_0^\infty \frac{1}{\kappa}\,\partial_\kappa\left(\frac{E(\kappa)}{\kappa}\right)\sin(\kappa z)\,d\kappa \tag{27}$$

$$E(\kappa) = \frac{\kappa}{\pi}\int_0^\infty \frac{1}{z}\,\partial_z\,(z^3\, c_1(z))\,\sin(\kappa z)\,dz. \tag{28}$$

The Sine-Fourier relations follow from the respective connections of $c_1$ and $E$ to the Fourier transforms $\gamma_0$ and $\mathbf{M}$. Plugging Eqs (26) and (23) into

$$\mathrm{tr}\boldsymbol{\gamma}_0(z) = \int_0^\infty\left(\int_0^{2\pi}\int_{-1}^{1} e^{i\kappa z q}\kappa^2\,\mathrm{tr}\mathbf{M}(\kappa)\,dq\,d\phi\,d\kappa = \frac{4\pi}{z}\int_0^\infty \kappa\,\mathrm{tr}\mathbf{M}(\kappa)\sin(\kappa z)\,d\kappa\right.$$

gives $\partial_z(z^3\, c_1(z)) = 2z\int_0^\infty E(\kappa)/\kappa\,\sin(\kappa z)\,d\kappa$ and consequently after some algebraic manipulations Eq (27).

**Further Decisive Coherences**
*Further relevant relations between longitudinal correlation function $c_1$ and energy spectrum $E$ are formulated as*

$$c_1(0) = \frac{2}{3}\int_0^\infty\left(E(\kappa)d\kappa\right. \tag{29}$$

$$\partial_{zz}c_1(0) = -\frac{2}{15}\int_0^\infty E(\kappa)\kappa^2 d\kappa. \tag{30}$$

By means of partial integration, Eq (27) can be rewritten as

$$c_1(z) = 2\int_0^\infty E(\kappa)\frac{\sin(\kappa z) - \kappa z\cos(\kappa z)}{k^3 z^3}\,d\kappa,$$

from that L'Hospitale yields directly Eqs (29) and (30).

Finally, the differentiability of an homogeneous Gaussian flow can be concluded from

$$\int_{\mathbb{R}^3} (\ln(1+\kappa))^\alpha \ \kappa^{2p} \, \mathbf{M}(\boldsymbol{\kappa}) d\boldsymbol{\kappa} < \infty, \quad \text{for } \alpha > 3. \tag{31}$$

According to [9], Eq (31) ensures the existence of an almost surely $p$-times sample differentiable modification that we equate to the considered flow for purposes of an intuitive notation. As for our isotropic incompressible local flow field, the differentiability can thus be formulated as an requirement on the decay of the energy spectrum $E$ by rewriting the volume integral of Eq (31) with help of Eqs (22), (25) as

$$\int_0^\infty \int_{S^2} (\ln(1+\kappa))^\alpha \ \kappa^{2p} \, \frac{E(\kappa)}{4\pi} \, (\mathbf{I} - \mathbf{e} \otimes \mathbf{e}) \, d\mathbf{e} \, d\kappa = \int_0^\infty \frac{2}{3} \, (\ln(1+\kappa))^\alpha \ \kappa^{2p} \, E(\kappa) d\kappa \, \mathbf{I}. \tag{32}$$

## 3.2 Parameters from $k$-$\epsilon$ Model

The kinetic turbulent energy $k$ and the dissipation rate $\epsilon$ stemming from the $k$-$\epsilon$ turbulence model act as parameters for the differentiable local fluctuation fields. Presupposing an isotropic, homogeneous and incompressible Gaussian flow, they can be expressed in terms of the correlation $c_1$ resp. the energy function $E$.

With $\mathbb{E}[\mathbf{w}(\mathbf{x}, t) \cdot \mathbf{w}(\mathbf{x}, t)] = \mathrm{tr}\boldsymbol{\gamma}_0(0) \overset{(26)}{=} 3\, c_1(0)$, we obtain

$$k = \frac{1}{2}\mathbb{E}[\mathbf{w}(\mathbf{x}, t) \cdot \mathbf{w}(\mathbf{x}, t)] = \frac{3}{2} c_1(0) \overset{(29)}{=} \int_0^\infty E(\kappa) d\kappa. \tag{33}$$

As for $\epsilon$, we consider $\mathbb{E}[\nabla \mathbf{w}(\mathbf{x}, t) \otimes \nabla \mathbf{w}(\mathbf{y}, t)] = \nabla_{\mathbf{x}} \nabla_{\mathbf{y}} \tilde{\boldsymbol{\gamma}}_0(\mathbf{x}, \mathbf{y}) = -\nabla_{\mathbf{z}} \nabla_{\mathbf{z}} \boldsymbol{\gamma}_0(\mathbf{z})$ with $\mathbf{z} = \mathbf{x} - \mathbf{y}$. Thus, the dissipation reads

$$\epsilon = \nu \, \mathbb{E}[\nabla \mathbf{w}(\mathbf{x}, t) : \nabla \mathbf{w}(\mathbf{x}, t)] = -\nu \, \nabla_{\mathbf{z}} \cdot \nabla_{\mathbf{z}} \mathrm{tr}(\boldsymbol{\gamma}_0(\mathbf{z}))|_{\mathbf{z}=\mathbf{0}} = -3\nu \, \partial_{zz} \mathrm{tr}\boldsymbol{\gamma}_0(z)|_{z=0}$$

and with Eq (26) and the differentiability of $c_1$

$$\epsilon = -15\nu \, \partial_{zz} c_1(0) \overset{(30)}{=} 2\nu \int_0^\infty E(\kappa) \kappa^2 d\kappa \tag{34}$$

The even extension $c_1(z) = c_1(-z)$ for $z \leq 0$ in combination with the Fourier relation (27) results in a global differentiability of $c_1$ on $\mathbb{R}$ such that its odd derivatives vanish at $z = 0$. Therefore, the parameters $k$ and $\epsilon$ describe the behavior of $c_1$ for small $z$ by a Taylor expansion up to $4^{\text{th}}$ order

$$c_1(z) = \frac{2}{3}k - \frac{1}{30}\frac{\epsilon}{\nu} z^2 + \mathcal{O}(z^4).$$

## 3.3 Kolmogorov's Energy Spectrum

For the construction of the complete correlation function $c_1$, we need additional physical information about the flow that can be gained from the energy spectrum $E$. The energy spectrum of isotropic turbulence was a well studied topic of research during the last century (see references in [7, 8]). In particular, Kolmogorov's work (1941) was trend setting. Based on dimensional analysis he derived not only the characteristic ranges but also the typical run of the spectrum which agree with later coming physical concepts and experiments [1]. In the following, we briefly state Kolmogorov's 5/3-Law and his hypothesis of local isotropy.

By Eq (21), the energy spectrum depends on the wave number $\kappa$. Moreover, observing that turbulence is strongly driven by the large eddies, $E$ can certainly be expected to be a function of the length $l_{\mathrm{T}}$ of the larger energy-containing eddies and the mean strain rate feeding the turbulence through direct interaction between mean flow and large eddies. Since turbulence is dissipative it should additionally depend on $\nu$ and $\epsilon$. Assuming a wide separation of energy $\kappa_e$ and dissipation $\kappa_d$ scales, Kolmogorov formulated his

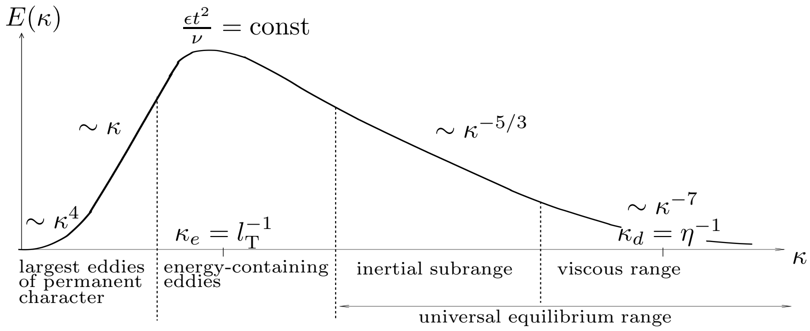


Figure 2: Sketch of energy spectrum for isotropic turbulence

**Universal Equilibrium Theory** [7]

1. *If $\kappa_e < \kappa_d$, there exists a range for wave numbers $\kappa > \kappa_e$, in which the turbulence is in a statistic equilibrium and exclusively determined by dissipation $\epsilon$ and kinematic viscosity $\nu$. This equilibrium state is universal, i.e. it occurs in isotropic as well as anisotropic turbulence. (Local isotropy hypothesis)*
2. *If $\kappa_e \ll \kappa_d$, there exists an inertial subrange for wave numbers $\kappa_e < \kappa < \kappa_d$ in which the energy spectrum is just a function of dissipation $\epsilon$ and wave number $\kappa$.*

By means of dimensional analysis the first hypothesis leads to the Kolmogorov scales for length $\eta$, time $t_\mathrm{K}$ and velocity $v_\mathrm{K}$

$$\eta = \left(\frac{\nu^3}{\epsilon}\right)^{1/4}, \qquad t_\mathrm{K} = \left(\frac{\nu}{\epsilon}\right)^{1/2}, \qquad v_\mathrm{K} = (\nu\,\epsilon)^{1/4}$$

with characteristic wave number $\kappa_\mathrm{K} = \eta^{-1} \approx \kappa_d$. The Kolmogorov length $\eta$ is the smallest characteristic turbulence length. The second hypothesis yields Kolmogorov's 5/3-Law

$$E(\kappa) = C_\mathrm{K}\,\epsilon^{2/3}\kappa^{-5/3}, \qquad \kappa_e < \kappa < \kappa_d \tag{35}$$

with Kolmogorov constant $C_\mathrm{K}$. Here, $C_\mathrm{K} = 0.5$ is supposed to be an appropriate estimate according to the experiments of Yeung et al. [17].

The form of the energy spectrum sketched in Fig 2 is also designed by Batchelor and Proudman (1956). They derived that $E(\kappa) \sim \kappa^4$ for $\kappa \to 0$, whereas Heisenberg (1948) deduced $E(\kappa) \sim \kappa^{-7}$ for $\kappa \to \infty$.

## 3.4 Initial Local Correlations

Having provided the mathematical and physical fundamental ideas, we model now the initial correlation tensor of a local, homogeneous, $\mathcal{L}^2$-continuous and differentiable Gaussian fluctuation field that satisfies the $k$-$\epsilon$ model and Kolmogorov's 5/3-Law. For this purpose, we introduce an admissible underlying spectral energy distribution function.

**Model for the Initial Local Correlation Tensor**
*Let $(\Omega, \mathcal{A}, \mathrm{P})$ be a probability space. Let $(\mathbf{w}_{\mathbf{x},t}, (\mathbf{x},t) \in \mathbb{R}^3 \times \mathbb{R}_0^+)$ be the Gaussian velocity fluctuation field of an isotropic, homogeneous and incompressible turbulent flow with $\mathbf{w}_{\mathbf{x},t} \in \mathcal{L}^2(\Omega, \mathcal{A}, \mathcal{P})$. Let kinetic energy $k$ and dissipation rate $\epsilon$ be constant. Construct the initial correlation function $c_1 \in \mathcal{C}^\infty(\mathbb{R}_0^+)$*

$$c_1(z) = \frac{2}{z^3} \int_0^\infty \frac{1}{\kappa}\,\partial_\kappa\left(\frac{E(\kappa)}{\kappa}\right) \sin(\kappa z)\,d\kappa$$

*by choosing $E \in \mathcal{C}^2(\mathbb{R}_0^+)$ as*

$$E(\kappa) = \begin{cases} K\kappa_1^{-5/3}\ \sum_{j=4}^{6} a_j\,(\frac{\kappa}{\kappa_1})^j & \kappa < \kappa_1 \\ K\kappa^{-5/3} & \kappa_1 \le \kappa \le \kappa_2 \\ K\kappa_2^{-5/3}\ \sum_{j=7}^{9} b_j\,(\frac{\kappa}{\kappa_2})^{-j} & \kappa > \kappa_2 \end{cases} \tag{36}$$

*where $\kappa_1$ and $\kappa_2$ are implicitly given by*

$$\int_0^\infty E(\kappa)\, d\kappa = k \quad \textit{and} \quad \int_0^\infty E(\kappa)\kappa^2\, d\kappa = \frac{\epsilon}{2\nu}. \tag{37}$$

*The parameters are fixed as $a_4 = 230/9$, $a_5 = -391/9$, $a_6 = 170/9$, $b_7 = 209/9$, $b_8 = -352/9$, $b_9 = 152/9$, $K = C_\mathrm{K}\, \epsilon^{2/3}$, $C_\mathrm{K} = 0.5$ and viscosity $\nu$.*

*Then, $(\mathbf{w}_{\mathbf{x},t}, (\mathbf{x}, t) \in \mathbb{R}^3 \times \mathbb{R}_0^+)$ is differentiable and fulfills the requirements of the Kolmogorov's 5/3-Law as well as of the $k$-$\epsilon$ model*

$$k = \frac{1}{2}\, \mathbb{E}[\mathbf{w}(\mathbf{x}, t) \cdot \mathbf{w}(\mathbf{x}, t)], \qquad \epsilon = \nu\, \mathbb{E}[\nabla\mathbf{w}(\mathbf{x}, t) : \nabla\mathbf{w}(\mathbf{x}, t)].$$

According to Eq (27), the presented nonnegative function $E$ satisfies the requirements on a spectral energy distribution function. Furthermore, it coincides with the run of Kolmogorov's energy spectrum (35). The differentiability of the local flow field, i.e. $(\ln(1 + \kappa))^\alpha\, \kappa^2\, E(\kappa) \in \mathcal{L}^1(\mathbb{R}_0^+)$ for $\alpha > 3$ (cf. Eq (32)), is ensured by the constructed decay of $E(\kappa) \sim \kappa^{-7}$ for $\kappa \to \infty$. The information coming from the $k$-$\epsilon$ model are finally included in the defined moments of $E$ on basis of Eqs (33) and (34).

Alternatively, also smoother variants of the energy spectrum are imaginable, but $E$ given by Eqs (36), (37) turns out to satisfy successfully our demands.

## 3.5 Dynamics of Local Correlations

The dynamics of a local correlation tensor $\boldsymbol{\gamma}$ might be described by an advection equation according to the observation that the decay of the mean properties is rather slow with respect to the time scale of the fluctuating fine-scale structures

$$\partial_\varsigma \boldsymbol{\gamma}(\mathbf{z}, \varsigma) + \bar{\mathbf{u}} \cdot \nabla_\mathbf{z} \boldsymbol{\gamma}(\mathbf{z}, \varsigma) = 0.$$

Its solution

$$\boldsymbol{\gamma}(\mathbf{z}, \varsigma) = \boldsymbol{\gamma}_0(\mathbf{z} - \bar{\mathbf{u}}\varsigma). \tag{38}$$

coincides with Taylor's hypothesis of frozen turbulence [15], i.e. fluctuations arise due to so-called frozen turbulence pattern that are transported by the mean flow without changing their structure.

Equation (38) completes the construction of the local correlation tensor $\boldsymbol{\gamma}$. Consequently, we deal here locally with homogeneous, isotropic, incompressible turbulence moving with the mean flow velocity $\bar{\mathbf{u}}$, whose spectral energy distribution $E$ fulfills the demands of the $k$-$\epsilon$ model as well as of Kolmogorov's universal equilibrium theory.

## 3.6 Construction of Global Turbulence

The Global-from-Local Assumption (12) prescribes the actual global fluctuation field $(\mathbf{u}'_{\mathbf{x},t}, (\mathbf{x}, t) \in \mathbb{R}^3 \times \mathbb{R}_0^+)$ on the basis of the family of underlying parameterized local fields $\{(\mathbf{w}^{\mathbf{y},\tau}_{\mathbf{x},t}, (\mathbf{x}, t) \in \mathbb{R}^3 \times \mathbb{R}_0^+), (\mathbf{y}, \tau) \in \mathbb{R}^3 \times \mathbb{R}_0^+\}$. However, so far the positive definiteness of its proposed correlation tensor $\boldsymbol{\Gamma}'$ is not proved, but it might be concluded from an explicit formulation of $\mathbf{u}'$.

**Explicit Formulation of the Global Fluctuation Field**
*Let the global fluctuation field $(\mathbf{u}'_{\mathbf{x},t}, (\mathbf{x}, t) \in \mathbb{R}^3 \times \mathbb{R}_0^+)$ be given as Ito-integral over the family of the local fields $\{(\mathbf{w}^{\mathbf{y},\tau}_{\mathbf{x},t}, (\mathbf{x}, t) \in \mathbb{R}^3 \times \mathbb{R}_0^+), (\mathbf{y}, \tau) \in \mathbb{R}^3 \times \mathbb{R}_0^+\}$*

$$\mathbf{u}'(\mathbf{x}, t) = \frac{1}{\sqrt{|M(\mathbf{x}, t)|}} \int_{M(\mathbf{x},t)} \mathbf{w}^{\mathbf{y},\tau}(\mathbf{x}, t)\; d\mathcal{W}_{\mathbf{y},\tau}, \tag{39}$$

$$M(\mathbf{x}, t) = \{(\mathbf{y}, \tau) \in \mathbb{R}^3 \times \mathbb{R}_0^+ \mid \|\mathbf{x} - \mathbf{y} - \bar{\mathbf{u}}(\mathbf{x}, t)(t - \tau)\|_2 \leq l_\mathrm{T} \,\wedge\, |t - \tau| \leq t_\mathrm{T}\},$$

*where $(\mathcal{W}_{\mathbf{y},\tau}, (\mathbf{y}, t) \in \mathbb{R}^3 \times \mathbb{R}_0^+)$ represents a Wiener process (Brownian motion). Then the field of Eq (39) satisfies the probability distribution, expectation and covariance structure of the averaging procedure $< . >$ in the Global-from-Local Assumption.*

The global field results from linear superpositions of joint Gaussians and is thus also Gaussian. Due to the permutability of expectation and integration with respect to space and time following from

Fubini's Theorem, it inherits the centered property from the local fields so that the constructed $(\mathbf{u}'_{\mathbf{x},t}, (\mathbf{x}, t) \in \mathbb{R}^3 \times \mathbb{R}_0^+)$ satisfies the definition of a turbulent Gaussian flow. Additionally, it is differentiable. Its correlation tensor reads

$$\begin{aligned}\mathbf{\Gamma}'(\mathbf{x_1}, t_1, \mathbf{x_2}, t_2) = &\frac{1}{\sqrt{|M(\mathbf{x_1}, t_1)|\,|M(\mathbf{x_2}, t_2)|}} \\ &\mathbb{E}\Big[\iint\limits_{M(\mathbf{x_1},t_1)} \mathbf{w}^{\mathbf{y_1},\tau_1}(\mathbf{x_1}, t_1)\, d\mathcal{W}_{\mathbf{y_1},\tau_1} \otimes \iint\limits_{M(\mathbf{x_2},t_2)} \mathbf{w}^{\mathbf{y_2},\tau_2}(\mathbf{x_2}, t_2)\, d\mathcal{W}_{\mathbf{y_2},\tau_2}\Big].\end{aligned} \tag{40}$$

By means of the Ito-calculus, the expectation of the dyadic product of the integrals can be expressed by

$$\begin{aligned}&\mathbb{E}\Big[\iint\limits_{M(\mathbf{x_1},t_1)} \mathbf{w}^{\mathbf{y_1},\tau_1}(\mathbf{x_1}, t_1)\, d\mathcal{W}_{\mathbf{y_1},\tau_1} \otimes \iint\limits_{M(\mathbf{x_2},t_2)} \mathbf{w}^{\mathbf{y_2},\tau_2}(\mathbf{x_2}, t_2)\, d\mathcal{W}_{\mathbf{y_2},\tau_2}\Big] \\ &\qquad = \mathbb{E}\Big[\iint\limits_{M(\mathbf{x_1},t_1)\cap M(\mathbf{x_2},t_2)} \mathbf{w}^{\mathbf{y},\tau}(\mathbf{x_1}, t_1) \otimes \mathbf{w}^{\mathbf{y},\tau}(\mathbf{x_2}, t_2)\, d\mathbf{y}\, d\tau\Big].\end{aligned}$$

Plugging this relation into Eq (40), we obtain the proposed covariance of the Global-from-Local Assumption for the in general inhomogeneous, anisotropic global flow

$$\mathbf{\Gamma}'(\mathbf{x_1}, t_1, \mathbf{x_2}, t_2) = \frac{1}{\sqrt{|M(\mathbf{x_1}, t_1)|\,|M(\mathbf{x_2}, t_2)|}} \iint\limits_{M(\mathbf{x_1},t_1)\cap M(\mathbf{x_2},t_2)} \tilde{\boldsymbol{\gamma}}^{\mathbf{y},\tau}(\mathbf{x_1}, t_1, \mathbf{x_2}, t_2)\; d\mathbf{y}\; d\tau.$$

Due to its derivation from the random field of Eq (39), $\mathbf{\Gamma}'$ is undoubtedly a positive definite function which is necessary for the numerical realization of $\mathbf{u}'$.

The global quantities for kinetic energy $k_{\mathbf{u}'}$ and dissipation rate $\epsilon_{\mathbf{u}'}$ are the averages over a region $M$ where the local, RANS-based quantities $k$ and $\epsilon$ only slightly differ. This region is determined by means of the turbulent large-scale length $l_\mathrm{T}$ and time $t_\mathrm{T}$ and under regard of the advective influence of the mean flow in Eq (38)

$$\begin{aligned}k_{\mathbf{u}'}(\mathbf{x}, t) &= \frac{1}{|M(\mathbf{x}, t)|} \int\limits_{M(\mathbf{x},t)} k(\mathbf{y}, \tau)\; d\mathbf{y}\; d\tau, \\ \epsilon_{\mathbf{u}'}(\mathbf{x}, t) &= \frac{1}{|M(\mathbf{x}, t)|} \int\limits_{M(\mathbf{x},t)} \epsilon(\mathbf{y}, \tau)\; d\mathbf{y}\; d\tau.\end{aligned}$$

In case of global homogeneity we achieve in particular the conformity of the global and local statistic quantities.

In spite of weaking the conditions on the global turbulent flow, $\mathbf{\Gamma}'$ still keeps the correlation structure of the local fields. Let $\lambda_\mathrm{T}$ be the turbulent fine-scale length, then $\boldsymbol{\gamma}_0^{\mathbf{y},\tau}(\mathbf{x_1} - \mathbf{x_2} - \bar{\mathbf{u}}(\mathbf{y}, \tau)(t_1 - t_2)) \approx \mathbf{0}$ for $\|\mathbf{x_1} - \mathbf{x_2} - \bar{\mathbf{u}}(\mathbf{y}, \tau)(t_1 - t_2)\|_2 > \lambda_\mathrm{T}$, $(\mathbf{y}, \tau) \in \mathbb{R}^3 \times \mathbb{R}_0^+$. Gluing the local correlations together yields $\mathbf{\Gamma}'(\mathbf{x_1}, t_1, \mathbf{x_2}, t_2) \approx \mathbf{0}$, even if $M(\mathbf{x_1}, t_1) \cap M(\mathbf{x_2}, t_2) \neq \emptyset$ as $\lambda_\mathrm{T} \ll l_\mathrm{T}$. Thus, $\mathbf{\Gamma}'$ states no wrong, absurd correlations.

# 4 General Aerodynamic Force Concept

In the course of this section, the aerodynamic force that is acting on the fiber is modeled on top of the RANS-based description for the turbulent flow. Thus, we introduce the mean relative velocity $\bar{\mathbf{v}}(s, t) = \bar{\mathbf{u}}(\mathbf{r}(s, t), t) - \partial_t \mathbf{r}(s, t)$. Then,

$$\tilde{\mathbf{f}}^{air}(s, t) = \mathbf{f}(\bar{\mathbf{v}}(s, t) + \mathbf{u}'(\mathbf{r}(s, t), t), \partial_s \mathbf{r}(s, t)) \tag{41}$$

prescribes a stochastic force $(\tilde{\mathbf{f}}^{air}_{s,t}, (s, t) \in [0, l] \times \mathbb{R}_0^+)$ as – generally nonlinear – function on the derived global fluctuation field $\mathbf{u}'$. However, the efficient numerical handling of this inhomogeneous construct (41) seems to be hopeless because of its complexity. Thus, we follow the Global-from-Local ansatz once more.

**Global-from-Local Force Concept**
*Let* $\mathbf{f} : \mathbb{R}^3 \times \mathbb{R}^2 \to \mathbb{R}^3$ *be an arbitrary chosen air drag model. Let* $\{(\mathbf{g}^{\sigma,\tau}_{s,t}, (s, t) \in [0, l] \times \mathbb{R}_0^+), (\sigma, \tau) \in$

*$[0,l]\times\mathbb{R}_0^+\}$ be a family of homogeneous local aerodynamic forces that are imposed by local Gaussian velocity fluctuation fields on the locally linear fiber around the respective fiber points $(\sigma,\tau)$. Then, the global aerodynamic force is constructed as Gaussian*

$$\mathbf{f}^{air}(\mathbf{r}(.),s,t) = <\mathbf{g}^{\sigma,\tau}(s,t)>_{N(\mathbf{r}(.),s,t)} \tag{42}$$

*with*

$$\begin{aligned} N(\mathbf{r}(.),s,t) =& \{(\sigma,\tau)\in[0,l]\times\mathbb{R}_0^+ \,| \\ & \|\mathbf{r}(s,t)-\mathbf{r}(\sigma,\tau)-\bar{\mathbf{u}}(\mathbf{r}(s,t),t)(t-\tau)\|_2 \le l_\mathrm{T} \wedge |t-\tau|\le t_\mathrm{T}\}, \end{aligned} \tag{43}$$

*and mean flow velocity $\bar{\mathbf{u}}$, turbulent large-scale length $l_\mathrm{T}$ and time $t_\mathrm{T}$ as well as averaging brackets $<.>$ defined analogously to Eq (12).*

In analogy to the velocity fluctuations in Sec 3, this concept (42) realizes a Gaussian global aerodynamic force along the fiber on the basis of a family of homogeneous local random forces. Focusing on the construction of these forces, correlated local forces are deduced from the restriction of our derived Gaussian local velocity fields on the fiber in Sec 4.1. The proposed linearization approach of Sec 4.2 enables their approximation by Gaussian white noise with flow-dependent amplitude for a macroscopic description of the fiber. Therefor, $\mathcal{L}^2$ and $\mathcal{L}^\infty$-similarity estimates are stated in Sec 4.3. In Sec 4.4 we finally present the corresponding correlated global aerodynamic force and its uncorrelated asymptotic limit.

## 4.1 Correlated Local Force

Define the family $\{(\mathbf{g}^{\sigma,\tau}_{s,t},(s,t)\in[0,l]\times\mathbb{R}_0^+),(\sigma,\tau)\in[0,l]\times\mathbb{R}_0^+\}$ of local aerodynamic forces by

$$\mathbf{g}^{\sigma,\tau}(s,t) = \mathbf{f}(\bar{\mathbf{v}}(\sigma,\tau)+\mathbf{w}_f^{\sigma,\tau}(s,t),\partial_s\mathbf{r}(\sigma,\tau)) \tag{44}$$

$$\mathbf{w}_f^{\sigma,\tau}(s,t) = \mathbf{w}^{\mathbf{r}(\sigma,\tau),\tau}(\mathbf{r}(\sigma,\tau)+(s-\sigma)\partial_s\mathbf{r}(\sigma,\tau)+(t-\tau)\partial_t\mathbf{r}(\sigma,\tau),t). \tag{45}$$

Presupposing a linear fiber around the point $(\sigma,\tau)$, the centered local Gaussian velocity fluctuation fields of Sec 3 keep their homogeneous correlation structure for their respective restrictions on the fiber in Eq (45)

$$\begin{aligned} \mathbb{E}[\mathbf{w}_f^{\sigma,\tau}(s_1,t_1)\otimes\mathbf{w}_f^{\sigma,\tau}(s_2,t_2)] &= \boldsymbol{\gamma}_0^{\mathbf{r}(\sigma,\tau),\tau}((s_1-s_2)\partial_s\mathbf{r}(\sigma,\tau)-(t_1-t_2)\bar{\mathbf{v}}(\sigma,\tau)) \\ &= \boldsymbol{\gamma}_f^{\sigma,\tau}(s_1-s_2,t_1-t_2). \end{aligned} \tag{46}$$

Locally, for small spatial and temporal differences, the assumption of the fiber linearity is reasonable, whereas for large ones $\boldsymbol{\gamma}_f^{\sigma,\tau}\approx\mathbf{0}$ anyway due to the decay of the correlations. By means of the transformation theorem of random variables, the homogeneous property is handed on $\mathbf{g}^{\sigma,\tau}$ for all feasible drag models $\mathbf{f}$ in Eq (44). Indeed, the chosen drag model determines the probability distributions of $\mathbf{g}^{\sigma,\tau}$ that are in general not Gaussian. Averaging over the prescribed homogeneous local forces along the fiber in Eq (42) results in a correlated global aerodynamic force that represents the turbulence effects on the fiber motion in Eq (7). Be aware that the stated Global-from-Local Force Concept generates here a functional dependence between $\mathbf{f}^{air}$ and $\mathbf{r}$ so that the fiber dynamics is not modeled by a system of partial differential equations as in the deterministic flow case of Eq (9).

## 4.2 Linearization Approach

The numerical realization of the correlated Gaussian global aerodynamic force $\mathbf{f}^{air}$ depends crucially on the determination of the probability distributions of $\mathbf{g}^{\sigma,\tau}$, in particular on the computation of the integrals for expectation and covariance according to the definition of the averaging brackets $<.>$, cf. Eq (12). The degree of difficulty is thereby mainly determined by the air drag model. For practical reasons, we hence propose an linearization ansatz for $\mathbf{g}^{\sigma,\tau}$ that yields Gaussian local forces

$$\begin{aligned} \mathbf{g}^{\sigma,\tau}(s,t) &= \mathbf{f}(\bar{\mathbf{v}}(\sigma,\tau)+\mathbf{w}_f^{\sigma,\tau}(s,t),\partial_s\mathbf{r}(\sigma,\tau)) \\ &\approx \mathbf{f}(\bar{\mathbf{v}}(\sigma,\tau),\partial_s\mathbf{r}(\sigma,\tau))+\mathbf{L}^\mathbf{f}(\sigma,\tau)\;\mathbf{w}_f^{\sigma,\tau}(s,t) \\ &= \mathbf{g}_{cc}^{\sigma,\tau}(s,t). \end{aligned} \tag{47}$$

where the linear operator $\mathbf{L}^{\mathbf{f}}$ is induced by the air drag model $\mathbf{f}$. The finite-dimensional distributions of $\mathbf{g}_{cc}^{\sigma,\tau}$ are uniquely given by expectation and covariance

$$\begin{aligned}\mathbb{E}[\mathbf{g}_{cc}^{\sigma,\tau}(s,t)] &= \mathbf{f}(\bar{\mathbf{v}}(\sigma,\tau), \partial_s \mathbf{r}(\sigma,\tau)) = \boldsymbol{\mu}^{\sigma,\tau}, \\ \mathrm{Cov}(\mathbf{g}_{cc}^{\sigma,\tau}(s_1,t_1), \mathbf{g}_{cc}^{\sigma,\tau}(s_2,t_2)) &= \mathbf{L}^{\mathbf{f}}(\sigma,\tau)\ \boldsymbol{\gamma}_f^{\sigma,\tau}(s_1-s_2, t_1-t_2)\ (\mathbf{L}^{\mathbf{f}}(\sigma,\tau))^t \\ &= \boldsymbol{\Gamma}_{\mathbf{g},cc}^{\sigma,\tau}(s_1-s_2, t_1-t_2) \end{aligned} \tag{48}$$

whose evaluation is directly deduced from the centered, homogeneous Gaussian $\mathbf{w}_f^{\sigma,\tau}$, see Eq (46).

## 4.3 Limit to Uncorrelated Local Force

The correlated Gaussian local forces $\mathbf{g}_{cc}^{\sigma,\tau}$ contain all turbulent coherences explicitely in their covariance function $\boldsymbol{\Gamma}_{\mathbf{g},cc}^{\sigma,\tau} : [0,l] \times \mathbb{R}_0^+ \to \mathbb{R}^{3\times 3}$ of Eq (48). Alternatively, uncorrelated generalized Gaussian local forces $\mathbf{g}_{uc}^{\sigma,\tau}$ might be introduced whose flow-dependent amplitude represents the mean turbulent coherences. Their covariance functions read

$$\boldsymbol{\Gamma}_{\mathbf{g},uc}^{\sigma,\tau}(s,t) = \int_{\mathbb{R}^2} \boldsymbol{\Gamma}_{\mathbf{g},cc}^{\sigma,\tau}(\xi,\varsigma)\ d\xi\, d\varsigma \quad \delta_0(s)\,\delta_0(t) \tag{49}$$

with the real one-dimensional Dirac function $\delta_0$. If their effects, i.e. their correlations, are compared on a macroscopic fiber scale that includes the whole covariance structure of $\mathbf{g}_{cc}^{\sigma,\tau}$, the family of the uncorrelated forces $\mathbf{g}_{uc}^{\sigma,\tau}$ is a good approximation for the one of the correlated $\mathbf{g}_{cc}^{\sigma,\tau}$. In the following, $\mathcal{L}^2$ and $\mathcal{L}^\infty$-estimates for their similarity take center stage.

Define the family $\{((\mathbf{g}_{uc}^{\sigma,\tau})_{s,t}, (s,t) \in [0,l] \times \mathbb{R}_0^+), (\sigma,\tau) \in [0,l] \times \mathbb{R}_0^+\}$ of local uncorrelated aerodynamic forces by

$$\mathbf{g}_{uc}^{\sigma,\tau}(s,t) = \mathbf{f}(\bar{\mathbf{v}}(\sigma,\tau), \partial_s \mathbf{r}(\sigma,\tau)) + \mathbf{L}^{\mathbf{f}}(\sigma,\tau)\ \mathbf{z}^{\sigma,\tau}(s,t) \tag{50}$$

$$\mathbf{z}^{\sigma,\tau}(s,t) = \mathbf{D}^{\sigma,\tau}\ \mathbf{p}^{\sigma,\tau}(s,t). \tag{51}$$

The centered uncorrelated local velocity fluctuation fields $(\mathbf{z}_{s,t}^{\sigma,\tau}, (s,t) \in [0,l] \times \mathbb{R}_0^+)$ along the fiber are particularly given by Gaussian white noise $(\mathbf{p}_{s,t}^{\sigma,\tau}, (s,t) \in [0,l] \times \mathbb{R}_0^+)$ with flow-dependent amplitude

$$\mathbf{D}^{\sigma,\tau} = \sqrt{\int_{\mathbb{R}^2} \boldsymbol{\gamma}_f^{\sigma,\tau}(\xi,\varsigma)\ d\xi\, d\varsigma} \tag{52}$$

that contains the integral correlations of $\mathbf{w}_f^{\sigma,\tau}$. The existence of $\mathbf{D}^{\sigma,\tau}$ presupposes the linear independence of the fiber tangent $\partial_s \mathbf{r}(\sigma,\tau)$ and the relative velocity $\bar{\mathbf{v}}(\sigma,\tau)$ as it can be concluded from the definition of $\boldsymbol{\gamma}_f^{\sigma,\tau}$ in Eq (46). The velocity correlations are then described by

$$\begin{aligned}\mathbb{E}[\mathbf{z}^{\sigma,\tau}(s_1,t_1) \otimes \mathbf{z}^{\sigma,\tau}(s_2,t_2)] &= (\mathbf{D}^{\sigma,\tau})^2\, \delta_0(s_1-s_2)\, \delta_0(t_1-t_2) \\ &= \boldsymbol{\delta}_f^{\sigma,\varsigma}(s_1-s_2, t_1-t_2) \end{aligned} \tag{53}$$

with the real one-dimensional Dirac function $\delta_0$. In this sense, $\boldsymbol{\delta}_f^{\sigma,\tau}$ is the uncorrelated analogon to $\boldsymbol{\gamma}_f^{\sigma,\tau}$ and induces the desired integral dependence (49) between $\boldsymbol{\Gamma}_{\mathbf{g},uc}^{\sigma,\tau}$ and $\boldsymbol{\Gamma}_{\mathbf{g},cc}^{\sigma,\tau}$ due to the linear construction in Eqs (50) and (47).

Focusing on an arbitrarily chosen fiber point $(\sigma,\tau)$, we skip the superscripts of the quantities in the following and deduce a formulation for the force amplitude $\mathbf{D}$ in terms of the manageable energy spectrum $E$ of Eq (21). Therefor, we presume the linear independence of fiber tangent $\mathbf{t} = \partial_s \mathbf{r}$ and mean relative velocity $\bar{\mathbf{v}}$, so that they induce the intuitive choice of a right-hand orthonormal basis, i.e. $\mathbf{t}$, $\mathbf{n} = (\bar{\mathbf{v}} - (\bar{\mathbf{v}}\cdot\mathbf{t})\mathbf{t})/\|\bar{\mathbf{v}} - (\bar{\mathbf{v}}\cdot\mathbf{t})\mathbf{t}\|_2$, $\mathbf{b} = \mathbf{t} \times \mathbf{n}$.

**Relation between Local Fiber Correlations and Spectral Quantities**
*Assume $\mathbf{t}$ and $\bar{\mathbf{v}}$ to be linearly independent, Let $\boldsymbol{\gamma}_f(\xi,\varsigma) = \boldsymbol{\gamma}_0(\xi\mathbf{t} - \varsigma\bar{\mathbf{v}})$, $(\xi,\varsigma) \in \mathbb{R}^2$ be the local velocity correlation tensor along the fiber. Then, its negative Fourier transform $\mathbf{m} = \mathcal{F}_{\boldsymbol{\gamma}_f}$ is expressed by the spectral density $\mathbf{M}$ of Eq (20)*

$$\mathbf{m}(\lambda_1,\lambda_2) = \int_{\mathbb{R}^3} \mathbf{M}(\boldsymbol{\kappa})\ \delta_0(\lambda_1 - \mathbf{t}\cdot\boldsymbol{\kappa})\ \delta_0(\lambda_2 + \bar{\mathbf{v}}\cdot\boldsymbol{\kappa})\ d\boldsymbol{\kappa}. \tag{54}$$

*The integral correlations are prescribed by* $\mathbf{m}(0,0) = (2\pi)^{-2} \int \boldsymbol{\gamma}_f(\xi,\varsigma)\, d\xi\, d\varsigma = \mathcal{F}_{\boldsymbol{\delta}_f}$. *In particular,*

$$\mathbf{m}(0,0) = \frac{1}{2\pi\bar{v}_\mathrm{n}} \int_0^\infty \frac{E(\kappa)}{\kappa^2} d\kappa\, \mathbf{P}_{\mathbf{t},\mathbf{n}}, \tag{55}$$

*where* $\mathbf{P}_{\mathbf{t},\mathbf{n}} := \mathbf{t}\otimes\mathbf{t}+\mathbf{n}\otimes\mathbf{n}$ *denotes the projector onto the plane spanned by* $\mathbf{t}$ *and* $\mathbf{n}$, *and* $\bar{v}_\mathrm{n} := \bar{\mathbf{v}}\cdot\mathbf{n}$.

Inserting the Fourier relation (20) for $\boldsymbol{\gamma}_0$ and $\mathbf{M}$ into the definition of $\mathbf{m}$ and evaluating the two-dimensional integral over the exponential function yields relation (54). Using isotropy and incompressibility of $\mathbf{M}$, Eqs (22), (25), the dependence on the energy spectrum follows

$$\mathbf{m}(\lambda_1,\lambda_2) = \frac{1}{4\pi} \int_{\mathbb{R}^3} \frac{E(\kappa)}{\kappa^2} (\mathbf{I} - \frac{1}{\kappa^2}\boldsymbol{\kappa}\otimes\boldsymbol{\kappa})\ \delta_0(\lambda_1 - \mathbf{t}\cdot\boldsymbol{\kappa})\ \delta_0(\lambda_2 + \bar{\mathbf{v}}\cdot\boldsymbol{\kappa})\ d\boldsymbol{\kappa}, \tag{56}$$

with $\kappa = \|\boldsymbol{\kappa}\|_2$. Consider the matrix $\mathbf{m}^{\mathbf{t},\mathbf{n},\mathbf{b}}$ that represents the tensor $\mathbf{m}$ in the $(\mathbf{t},\bar{\mathbf{v}})$-induced basis and substitute $\mathbf{t}\cdot\boldsymbol{\kappa} = \kappa_\mathrm{t}$, $\mathbf{n}\cdot\boldsymbol{\kappa} = \kappa_\mathrm{n}$ and $\mathbf{b}\cdot\boldsymbol{\kappa} = \kappa_\mathrm{b}$. Integration over $\kappa_\mathrm{t}$ and $\kappa_\mathrm{n}$ gives then $\mathbf{m}^{\mathbf{t},\mathbf{n},\mathbf{b}}(0,0) = \int_0^\infty E(\kappa)/\kappa^2 d\kappa/(2\pi\bar{v}_\mathrm{n})\ \mathrm{diag}(1,1,0)$ and with the spectral theorem on the eigenvalues the invariant form (55) of the tensor.

**Relation between Force Amplitude and Energy Spectrum**
*Let* $\mathbf{D}$ *be the force amplitude and* $E$ *the energy spectrum corresponding to an homogeneous, isotropic and incompressible local velocity fluctuation field. Then the following relation holds:*

$$\mathbf{D} = \sqrt{\frac{2\pi}{\bar{v}_\mathrm{n}} \int_0^\infty \frac{E(\kappa)}{\kappa^2} d\kappa}\ \mathbf{P}_{\mathbf{t},\mathbf{n}} \tag{57}$$

Relation (57) results directly from Eqs (52) and (55). It allows the interesting observation that the uncorrelated local velocity fluctuation field $\mathbf{z}$ of Eq (51) has no component in the binormal direction $\mathbf{b}$ of the fiber. The reason for this behavior is the incompressibility of the underlying flow field, since

$$\mathbf{P}_\mathbf{b} \int_{\mathbb{R}^2} \boldsymbol{\gamma}_f(\xi,\varsigma)\ d\xi\, d\varsigma = \mathbf{P}_\mathbf{b} \int_0^\infty z c_2(z)\, dz = \mathbf{P}_\mathbf{b} \int_0^\infty e_1(\kappa)\, d\kappa = \mathbf{0}, \qquad \mathbf{P}_\mathbf{b} = \mathbf{b}\otimes\mathbf{b}$$

due to Eq (25) or respectively to Eq (24) and partial integration.

Proceeding with the general similarity estimates for the correlated and uncorrelated local force, it is sufficient to study the effects of the centered local velocity fluctuation fields on a macroscopic fiber scale because of their linear relation, Eqs (47), (50). For this purpose, we consider the respective macroscopic velocity fields that are gained from spatially and temporally smoothing along the fiber and compare their correlation tensors.

Let $\mathbf{w}_f$ and $\mathbf{z}$ be a correlated and uncorrelated local velocity fluctuation field. The introduction of the normalized spatial and temporal smoothing functions $G_{\boldsymbol{\alpha}} : \mathbb{R}^2 \to \mathbb{R}$, $\boldsymbol{\alpha} = (\alpha_s, \alpha_t) \in (\mathbb{R}_0^+)^2$ enables then the definition of two families of macroscopic velocity fields along the fiber

$$\mathbf{W}_{\boldsymbol{\alpha}}(s,t) = \int G_{\boldsymbol{\alpha}}(s-\phi, t-\psi)\ \mathbf{w}_f(\phi,\psi)\ d\psi\ d\phi, \tag{58}$$

$$\mathbf{Z}_{\boldsymbol{\alpha}}(s,t) = \int G_{\boldsymbol{\alpha}}(s-\phi, t-\psi)\ \ \mathbf{z}(\phi,\psi)\ \ d\psi\ d\phi \tag{59}$$

with their correlation tensors

$$\boldsymbol{\Gamma}_{\mathbf{W}_{\boldsymbol{\alpha}}}(\xi,\varsigma) = \int H_{\boldsymbol{\alpha}}(\xi-\phi, \varsigma-\psi)\ \boldsymbol{\gamma}_f(\phi,\psi)\ d\psi\, d\phi, \tag{60}$$

$$\boldsymbol{\Gamma}_{\mathbf{Z}_{\boldsymbol{\alpha}}}(\xi,\varsigma) = \int H_{\boldsymbol{\alpha}}(\xi-\phi, \varsigma-\psi)\ \boldsymbol{\delta}_f(\phi,\psi)\ d\psi\, d\phi, \tag{61}$$

where $H_{\boldsymbol{\alpha}}(\xi,\varsigma) = \int G_{\boldsymbol{\alpha}}(\xi-\phi,\varsigma-\psi)\ G_{\boldsymbol{\alpha}}(\phi,\psi)\ d\psi\, d\phi$ are also normalized smoothing functions. Taking the convolution keeps the properties of the local fields so that $\mathbf{W}_{\boldsymbol{\alpha}}$ and $\mathbf{Z}_{\boldsymbol{\alpha}}$ are Gaussian, centered and homogeneous for all smoothing parameters $\boldsymbol{\alpha} \in (\mathbb{R}_0^+)^2$. The Gaussian property follows thereby directly from the linear superposition of joint Gaussians. The centered and homogeneous property are deduced by using the permutability of expectation and integration according to Fubini's Theorem.

**Choice of Smoothing Operators**
*Let the smoothing functions $G_{\boldsymbol{\alpha}} : \mathbb{R}^2 \to \mathbb{R}$, $\boldsymbol{\alpha} = (\alpha_s, \alpha_t) \in (\mathbb{R}_0^+)^2$ be defined as products of spatial and temporal characteristic functions*

$$G_{\boldsymbol{\alpha}}(\xi, \varsigma) = \alpha_s \alpha_t \; \chi_{[\frac{-1}{2\alpha_s}, \frac{1}{2\alpha_s}]}(\xi)\, \chi_{[\frac{-1}{2\alpha_t}, \frac{1}{2\alpha_t}]}(\varsigma). \tag{62}$$

*Then, $H_{\boldsymbol{\alpha}} : \mathbb{R}^2 \to \mathbb{R}$ are given by the products of the hat functions, and their respective negative Fourier transforms are*

$$\begin{aligned} H_{\boldsymbol{\alpha}}(\xi, \varsigma) &= \alpha_s\, \alpha_t\; (1 - |\alpha_s\, \xi|)\,(1 - |\alpha_t\, \varsigma|)\; \chi_{[\frac{-1}{\alpha_s}, \frac{1}{\alpha_s}]}(\xi)\, \chi_{[\frac{-1}{\alpha_t}, \frac{1}{\alpha_t}]}(\varsigma) \\ \mathcal{F}_{H_{\boldsymbol{\alpha}}}(\kappa_1, \kappa_2) &= \mathcal{F}_{H_{\mathbf{1}}}\left(\frac{\kappa_1}{\alpha_s}, \frac{\kappa_2}{\alpha_t}\right) = \frac{1}{\pi^2}\; \frac{1 - \cos(\kappa_1/\alpha_s)}{(\kappa_1/\alpha_s)^2}\; \frac{1 - \cos(\kappa_2/\alpha_t)}{(\kappa_2/\alpha_t)^2}. \end{aligned} \tag{63}$$

The relation between $\mathcal{F}_{H_{\boldsymbol{\alpha}}}$ and $\mathcal{F}_{H_{\mathbf{1}}}$ results directly from their definition by using $H_{\boldsymbol{\alpha}}(\xi, \varsigma) = \alpha_s\, \alpha_t\, H_{\mathbf{1}}(\alpha_s\, \xi, \alpha_t\, \varsigma)$.

The derivation of the similarity estimates depends decisively on the behavior of the symmetric, nonnegative, differentiable function $\mathcal{E} : \mathbb{R}^2 \to \mathbb{R}_0^+$ that is defined by means of the energy spectrum $E$

$$\mathcal{E}(\kappa_1, \kappa_2) := \int_{\mathbb{R}} \frac{E(\|(\kappa_1, \kappa_2, l)\|_2)}{(\kappa_1, \kappa_2, l)^2}\; dl. \tag{64}$$

It is radially decaying with maximum in the origin, i.e. $\max_{\boldsymbol{\kappa}} \mathcal{E}(\kappa_1, \kappa_2) = \mathcal{E}(0, 0)$ and $g(\kappa) := \mathcal{E}(\kappa, a\kappa), \kappa \in \mathbb{R}_0^+$ strictly monotonically decreasing for $a \in \mathbb{R}$.

**Similarity Estimates**
*Choose the smoothing functions $G_{\boldsymbol{\alpha}} : \mathbb{R}^2 \to \mathbb{R}$, $\boldsymbol{\alpha} = (\alpha_s, \alpha_t) \in (\mathbb{R}_0^+)^2$ of Eq (62) for the definition of the families of macroscopic velocity fields according to Eqs (58) and (59). Then the following estimates hold:*
*$\mathcal{L}^2$-similarity:*

$$\begin{aligned} \mathcal{I}_{\mathcal{L}^2} &:= \|\boldsymbol{\Gamma}_{\mathbf{W}_{\boldsymbol{\alpha}}} - \boldsymbol{\Gamma}_{\mathbf{Z}_{\boldsymbol{\alpha}}}\|_{\mathcal{L}^2(l^2(\mathbb{R}^2))} \\ &\leq \frac{\sqrt{\alpha_s\, \alpha_t}}{\sqrt{6}\, \pi\, \bar{v}_{\mathrm{n}}}\; \sqrt{\mathcal{S}^2 \left(\alpha_s^2\, (1 + \frac{\bar{v}_{\mathrm{t}}^2}{\bar{v}_{\mathrm{n}}^2}) + \frac{\alpha_t^2}{\bar{v}_{\mathrm{n}}^2}\right) + \frac{8\mathcal{E}_0^2}{3\pi} \left(\alpha_s^3 + \frac{\alpha_t^3}{(\bar{v}_{\mathrm{n}} + |\bar{v}_{\mathrm{t}}|)^3}\right)} \end{aligned} \tag{65}$$

*$\mathcal{L}^\infty$-similarity:*

$$\begin{aligned} \mathcal{I}_{\mathcal{L}^\infty} &:= \|\boldsymbol{\Gamma}_{\mathbf{W}_{\boldsymbol{\alpha}}} - \boldsymbol{\Gamma}_{\mathbf{Z}_{\boldsymbol{\alpha}}}\|_{\mathcal{L}^\infty(l^2(\mathbb{R}^2))} \\ &\leq \frac{\sqrt{2}\, \alpha_s\, \alpha_t}{\pi^2\, \bar{v}_{\mathrm{n}}} \left[\mathcal{S} \left(\alpha_s\, (1 + \frac{\bar{v}_{\mathrm{t}}}{\bar{v}_{\mathrm{n}}}) \left(\frac{c}{2} + \ln(\frac{1}{\alpha_s})\right) + \frac{\alpha_t}{\bar{v}_{\mathrm{n}}} \left(\frac{c}{2} + \ln(\frac{\bar{v}_{\mathrm{n}} + |\bar{v}_{\mathrm{t}}|}{\alpha_t})\right)\right) \right. \\ &\qquad \left. + \mathcal{E}_0 \left(\alpha_s + \frac{\alpha_t}{\bar{v}_{\mathrm{n}} + |\bar{v}_{\mathrm{t}}|}\right)\right] \end{aligned} \tag{66}$$

*where*

$$\begin{aligned} \|\boldsymbol{\Gamma}\|_{\mathcal{L}^2(l^2(\mathbb{R}^2))} &:= (\int_{\mathbb{R}^2} \boldsymbol{\Gamma}(\xi, \varsigma) : \boldsymbol{\Gamma}(\xi, \varsigma)\; d\xi\, d\varsigma)^{1/2} \\ \|\boldsymbol{\Gamma}\|_{\mathcal{L}^\infty(l^2(\mathbb{R}^2))} &:= \sup_{(\xi, \varsigma) \in \mathbb{R}^2} (\boldsymbol{\Gamma}(\xi, \varsigma) : \boldsymbol{\Gamma}(\xi, \varsigma))^{1/2}. \end{aligned}$$

*The quantities $\mathcal{E}_0 = \mathcal{E}(0, 0)$ and $\mathcal{S} = \sup_{\boldsymbol{\kappa} \in [0,1]^2} \|\nabla_{\boldsymbol{\kappa}} \mathcal{E}(\kappa_1, \kappa_2)\|_2$ are defined by the energy moment of Eq (64). Moreover, $\bar{v}_{\mathrm{t}} = \bar{\mathbf{v}} \cdot \mathbf{t}$, $\bar{v}_{\mathrm{n}} = \bar{\mathbf{v}} \cdot \mathbf{n}$ and $c = \int_0^1 (1 - \cos \iota)/\iota\, d\iota$.*

**Proof**
ad $\mathcal{L}^2$-similarity:
The norm in $\mathcal{L}^2(l^2(\mathbb{R}^2))$ is conserved under the Fourier transformation according to the Plancherel Theorem as the operator : induces a scalar product in the $l^2$-space. Using the fact that the Fourier transform of a convolution equals the product of the respective Fourier transforms gives then

$$\begin{aligned}\|\boldsymbol{\Gamma}\mathbf{W}_{\boldsymbol{\alpha}} - \boldsymbol{\Gamma}\mathbf{Z}_{\boldsymbol{\alpha}}\|^2_{\mathcal{L}^2(l^2(\mathbb{R}^2))} &= (2\pi)^2 \,\|(\mathcal{F}_{\boldsymbol{\gamma}_f} - \mathcal{F}_{\boldsymbol{\delta}_f})\,\mathcal{F}_{H_{\boldsymbol{\alpha}}}\|^2_{\mathcal{L}^2(l^2(\mathbb{R}^2))} \\ &= (2\pi)^2 \iint_{\mathbb{R}^2} \|\mathbf{m}(\lambda_1,\lambda_2) - \mathbf{m}(0,0)\|^2_{l^2}\, \mathcal{F}^2_{H_{\boldsymbol{\alpha}}}(\lambda_1,\lambda_2)\, d\lambda_1 d\lambda_2.\end{aligned} \tag{67}$$

With Eq (56) and

$$(\mathbf{I} - \frac{1}{\boldsymbol{\kappa}^2}\boldsymbol{\kappa}\otimes\boldsymbol{\kappa}) : (\mathbf{I} - \frac{1}{\boldsymbol{\iota}^2}\boldsymbol{\iota}\otimes\boldsymbol{\iota}) = 1 + \frac{(\boldsymbol{\kappa}\cdot\boldsymbol{\iota})^2}{\boldsymbol{\kappa}^2\boldsymbol{\iota}^2} \le 2, \tag{68}$$

we obtain

$$\begin{aligned}\|\mathbf{m}(\lambda_1,\lambda_2) - \mathbf{m}(0,0)\|^2_{l^2} =& \frac{1}{(4\pi)^2} \int_{\mathbb{R}^3}\int_{\mathbb{R}^3} \frac{E(\|\boldsymbol{\kappa}\|_2)}{\boldsymbol{\kappa}^2}\frac{E(\|\boldsymbol{\iota}\|_2)}{\boldsymbol{\iota}^2}\left(1 + \frac{(\boldsymbol{\kappa}\cdot\boldsymbol{\iota})^2}{\boldsymbol{\kappa}^2\boldsymbol{\iota}^2}\right) \\ &(\delta_0(\lambda_1 - \mathbf{t}\cdot\boldsymbol{\kappa})\delta_0(\lambda_2 + \bar{\mathbf{v}}\cdot\boldsymbol{\kappa}) - \delta_0(\mathbf{t}\cdot\boldsymbol{\kappa})\delta_0(\bar{\mathbf{v}}\cdot\boldsymbol{\kappa})) \\ &(\delta_0(\lambda_1 - \mathbf{t}\cdot\boldsymbol{\iota})\delta_0(\lambda_2 + \bar{\mathbf{v}}\cdot\boldsymbol{\iota}) - \delta_0(\mathbf{t}\cdot\boldsymbol{\iota})\delta_0(\bar{\mathbf{v}}\cdot\boldsymbol{\iota}))\; d\boldsymbol{\kappa}\, d\boldsymbol{\iota}.\end{aligned}$$

Inserting this relation in (67) and integrating over $\lambda_1$ and $\lambda_2$ kills two Dirac functions. The other two vanish after choosing the $(\mathbf{t},\bar{\mathbf{v}})$-induced basis. Applying Eqs (64) and (68) yields with $\bar{v}_{\mathrm{t}} = \bar{\mathbf{v}}\cdot\mathbf{t}$ and $\bar{v}_{\mathrm{n}} = \bar{\mathbf{v}}\cdot\mathbf{n} = \|\bar{\mathbf{v}} - (\bar{\mathbf{v}}\cdot\mathbf{t})\mathbf{t}\|_2 > 0$

$$\begin{aligned}\mathcal{I}^2_{\mathcal{L}^2} \le& \frac{1}{2\bar{v}_{\mathrm{n}}}[\iint_{\mathbb{R}^2} (\mathcal{E}^2(\kappa_1,\kappa_2) - 2\mathcal{E}(\kappa_1,\kappa_2)\mathcal{E}(0,0))\, \mathcal{F}^2_{H_{\boldsymbol{\alpha}}}(\kappa_1, -(\bar{v}_{\mathrm{t}}\kappa_1 + \bar{v}_{\mathrm{n}}\kappa_2))\, d\kappa_1\, d\kappa_2 \\ &+ \int_{\mathbb{R}^2} \frac{1}{\bar{v}_{\mathrm{n}}}\mathcal{E}^2(0,0)\; \mathcal{F}^2_{H_{\boldsymbol{\alpha}}}(\lambda_1,\lambda_2)\, d\lambda_1\, d\lambda_2] \\ =& \frac{\alpha_s\alpha_t}{2\bar{v}_{\mathrm{n}}^2}\iint_{\mathbb{R}^2}\left(\mathcal{E}(\alpha_s\iota_1, \frac{1}{\bar{v}_{\mathrm{n}}}(\alpha_t\iota_2 - \alpha_s\bar{v}_{\mathrm{t}}\iota_1)) - \mathcal{E}(0,0)\right)^2 \mathcal{F}^2_{H_{\mathbf{1}}}(\iota_1,\iota_2)\, d\iota_1\, d\iota_2.\end{aligned} \tag{69}$$

The latter calculation is based on the substitution $\kappa_1 = \alpha_s\iota_1$, $\bar{v}_{\mathrm{t}}\kappa_1 + \bar{v}_{\mathrm{n}}\kappa_2 = \alpha_t\iota_2$, $\lambda_1 = \alpha_s\iota_1$, $\lambda_2 = \alpha_t\iota_2$ and the properties of the even smoothing functions (63). Positivity and radial decay of $\mathcal{E}$ induce the splitting of the integral in Eq (69)

$$\mathcal{I}^2_{\mathcal{L}^2} \le \frac{\alpha_s\alpha_t}{2\bar{v}_{\mathrm{n}}^2}\;(J_U + J_{\mathbb{R}^2\setminus U}). \tag{70}$$

with regard to the domain decomposition $\mathbb{R}^2 = U \cup (\mathbb{R}^2 \setminus U)$ where

$$U := \{(\iota_1,\iota_2) \mid \iota_1 \in [-\alpha_s^{-1}, \alpha_s^{-1}] \wedge \iota_2 \in [-\alpha_t^{-1}(\bar{v}_{\mathrm{n}} + |\bar{v}_{\mathrm{t}}|), \alpha_t^{-1}(\bar{v}_{\mathrm{n}} + |\bar{v}_{\mathrm{t}}|)]\}.$$

The energy difference in $J_U$ can be estimated by means of its differentiability, for $(\mathcal{E}(\alpha_s\iota_1, \bar{v}_{\mathrm{n}}^{-1}(\alpha_t\iota_2 - \alpha_s\bar{v}_{\mathrm{t}}\iota_1)) - \mathcal{E}(0,0))^2 \le S^2\,\|(\alpha_s\iota_1, \bar{v}_{\mathrm{n}}^{-1}(\alpha_t\iota_2 - \alpha_s\bar{v}_{\mathrm{t}}\iota_1))\|_2^2$. Thus,

$$J_U \le \mathcal{S}^2 \iint_U \left(\alpha_s^2(1 + \frac{\bar{v}_{\mathrm{t}}^2}{\bar{v}_{\mathrm{n}}^2})\iota_1^2 + \frac{\alpha_t^2}{\bar{v}_{\mathrm{n}}^2}\iota_2^2 - 2\alpha_s\alpha_t\frac{\bar{v}_{\mathrm{t}}}{\bar{v}_{\mathrm{n}}^2}\iota_1\iota_2\right)\; \mathcal{F}^2_{H_{\mathbf{1}}}(\iota_1,\iota_2)\; d\iota_1\, d\iota_2$$

The odd term vanishes by the integration. Using the equivalence of the integrand in the four quadrants we obtain with Eq (63)

$$\begin{aligned}J_U \le& 4\mathcal{S}^2 \int_0^{\alpha_t^{-1}(\bar{v}_{\mathrm{n}}+|\bar{v}_{\mathrm{t}}|)}\int_0^{\alpha_s^{-1}} \left(\alpha_s^2(1 + \frac{\bar{v}_{\mathrm{t}}^2}{\bar{v}_{\mathrm{n}}^2})\,\iota_1^2 + \frac{\alpha_t^2}{\bar{v}_{\mathrm{n}}^2}\,\iota_2^2\right)\mathcal{F}^2_{H_{\mathbf{1}}}(\iota_1,\iota_2)\; d\iota_1\, d\iota_2 \\ \le& \frac{\mathcal{S}^2}{3\pi^2}\;\left(\alpha_s^2(1 + \frac{\bar{v}_{\mathrm{t}}^2}{\bar{v}_{\mathrm{n}}^2}) + \frac{\alpha_t^2}{\bar{v}_{\mathrm{n}}^2}\right),\end{aligned} \tag{71}$$

where the compact integration domain is replaced by $(\mathbb{R}_0^+)^2$. On the other hand, the energy difference in $J_{\mathbb{R}^2\setminus U}$ can be estimated by its maximum $\mathcal{E}_0$ due to the strict decay of $\mathcal{E}$. The equivalence of the integrand in the quadrants leads then to

$$\begin{aligned} J_{\mathbb{R}^2\setminus U} &\leq 4\mathcal{E}_0^2 \left( \int_0^\infty \int_{\alpha_s^{-1}}^\infty \mathcal{F}^2_{H_\mathbf{1}}(\iota_1,\iota_2)\, d\iota_1\, d\iota_2 + \int_{\alpha_t^{-1}(\bar{v}_\mathrm{n}+|\bar{v}_\mathrm{t}|)}^\infty \int_0^{\alpha_s^{-1}} \mathcal{F}^2_{H_\mathbf{1}}(\iota_1,\iota_2)\, d\iota_1\, d\iota_2 \right) \\ &\leq \frac{8\mathcal{E}_0^2}{9\pi^3} \left( \alpha_s^3 + \frac{\alpha_t^3}{(\bar{v}_\mathrm{n}+|\bar{v}_\mathrm{t}|)^3} \right) \end{aligned} \tag{72}$$

where the integration interval of $\iota_1$ in the second summand is replaced by $\mathbb{R}_0^+$. Inserting Eqs (71) and (72) in Eq (70) yields the $\mathcal{L}^2$-estimate.

ad $\mathcal{L}^\infty$-similarity:
The $\mathcal{L}^\infty$-estimate is derived in analogy to the $\mathcal{L}^2$-estimate. Consider therefor

$$\begin{aligned} \|(\mathbf{\Gamma}\mathbf{w}_{\boldsymbol{\alpha}} - \mathbf{\Gamma}\mathbf{z}_{\boldsymbol{\alpha}})(\boldsymbol{\sigma})\|_{l^2}^2 &= \| \int_{\mathbb{R}^2} e^{i\boldsymbol{\lambda}\cdot\boldsymbol{\sigma}}\, (\mathbf{m}(\boldsymbol{\lambda}) - \mathbf{m}(\mathbf{0}))\, \mathcal{F}_{H_{\boldsymbol{\alpha}}}(\boldsymbol{\lambda})\, d\boldsymbol{\lambda} \|_{l^2}^2 \\ &= \frac{1}{(4\pi)^2} \int_{\mathbb{R}^2}\int_{\mathbb{R}^2}\int_{\mathbb{R}^3}\int_{\mathbb{R}^3} e^{i(\boldsymbol{\lambda}+\boldsymbol{\mu})\cdot\boldsymbol{\sigma}}\, \mathcal{F}_{H_{\boldsymbol{\alpha}}}(\boldsymbol{\lambda})\, \mathcal{F}_{H_{\boldsymbol{\alpha}}}(\boldsymbol{\mu}) \frac{E(\|\boldsymbol{\kappa}\|_2)}{\boldsymbol{\kappa}^2} \frac{E(\|\boldsymbol{\iota}\|_2)}{\boldsymbol{\iota}^2} \left( 1 + \frac{(\boldsymbol{\kappa}\cdot\boldsymbol{\iota})^2}{\boldsymbol{\kappa}^2\boldsymbol{\iota}^2} \right) \\ &\qquad (\delta_0(\lambda_1 - \mathbf{t}\cdot\boldsymbol{\kappa})\delta_0(\lambda_2 + \bar{\mathbf{v}}\cdot\boldsymbol{\kappa}) - \delta_0(\mathbf{t}\cdot\boldsymbol{\kappa})\delta_0(\bar{\mathbf{v}}\cdot\boldsymbol{\kappa})) \\ &\qquad (\delta_0(\mu_1 - \mathbf{t}\cdot\boldsymbol{\iota})\delta_0(\mu_2 + \bar{\mathbf{v}}\cdot\boldsymbol{\iota}) - \delta_0(\mathbf{t}\cdot\boldsymbol{\iota})\delta_0(\bar{\mathbf{v}}\cdot\boldsymbol{\iota}))\; d\boldsymbol{\kappa}\, d\boldsymbol{\iota}\, d\boldsymbol{\lambda}\, d\boldsymbol{\mu} \end{aligned}$$

according to Eqs (56) and (68). Following the calculations of the $\mathcal{L}^2$-estimate gives

$$\begin{aligned} &\|(\mathbf{\Gamma}\mathbf{w}_{\boldsymbol{\alpha}} - \mathbf{\Gamma}\mathbf{z}_{\boldsymbol{\alpha}})(\boldsymbol{\sigma})\|_{l^2}^2 \\ &\leq \frac{\alpha_s^2\,\alpha_t^2}{8\pi^2\,\bar{v}_\mathrm{n}^2} \left( \int_{\mathbb{R}^2} e^{i(\alpha_s\iota_1, -\alpha_t\iota_2)\cdot\boldsymbol{\sigma}} \left( \mathcal{E}(\alpha_s\iota_1, \frac{1}{\bar{v}_\mathrm{n}}(\alpha_t\iota_2 - \alpha_s\bar{v}_\mathrm{t}\iota_1)) - \mathcal{E}(0,0) \right) \mathcal{F}_{H_\mathbf{1}}(\boldsymbol{\iota}) d\boldsymbol{\iota} \right)^2 \\ &\leq \frac{\alpha_s^2\,\alpha_t^2}{8\pi^2\,\bar{v}_\mathrm{n}^2} \left( \int_{\mathbb{R}^2} \left| \mathcal{E}(\alpha_s\iota_1, \frac{1}{\bar{v}_\mathrm{n}}(\alpha_t\iota_2 - \alpha_s\bar{v}_\mathrm{t}\iota_1)) - \mathcal{E}(0,0) \right| \mathcal{F}_{H_\mathbf{1}}(\boldsymbol{\iota})\, d\boldsymbol{\iota} \right)^2 \end{aligned}$$

Repeating then the splitting ansatz for the integral and the estimation arguments for the energy difference in $J_U$ and $J_{\mathbb{R}^2\setminus U}$ yields

$$\begin{aligned} J_U &\leq \frac{4\mathcal{S}}{\pi^2} \int_0^{\alpha_t^{-1}(\bar{v}_\mathrm{n}+|\bar{v}_\mathrm{t}|)} \int_0^{\alpha_s^{-1}} \left( \alpha_s(1 + \frac{|\bar{v}_\mathrm{t}|}{\bar{v}_\mathrm{n}})\,\iota_1 + \frac{\alpha_t}{\bar{v}_\mathrm{n}}\,\iota_2 \right) \mathcal{F}_{H_\mathbf{1}}(\iota_1,\iota_2)\, d\iota_1\, d\iota_2 \\ &\leq \frac{4\mathcal{S}}{\pi^2} \int_0^\infty \frac{1-\cos\iota}{\iota^2} d\iota \left( \alpha_s\,(1 + \frac{|\bar{v}_\mathrm{t}|}{\bar{v}_\mathrm{n}}) \left( \int_0^1 \frac{1-\cos\iota}{\iota} d\iota + \int_1^{\alpha_s^{-1}} \frac{1-\cos\iota}{\iota} d\iota \right) \right. \\ &\qquad\qquad \left. + \frac{\alpha_t}{\bar{v}_\mathrm{n}} \left( \int_0^1 \frac{1-\cos\iota}{\iota} d\iota + \int_1^{\alpha_t^{-1}(\bar{v}_\mathrm{n}+|\bar{v}_\mathrm{t}|)} \frac{1-\cos\iota}{\iota} d\iota \right) \right) \\ &\leq \frac{2\mathcal{S}}{\pi} \left( \alpha_s\,(1 + \frac{\bar{v}_\mathrm{t}}{\bar{v}_\mathrm{n}}) \left( c + 2\ln(\frac{1}{\alpha_s}) \right) + \frac{\alpha_t}{\bar{v}_\mathrm{n}} \left( c + 2\ln(\frac{\bar{v}_\mathrm{n}+|\bar{v}_\mathrm{t}|}{\alpha_t}) \right) \right) \end{aligned}$$

with $c = \int_0^1 (1-\cos\iota)/\iota\, d\iota$ and

$$\begin{aligned} J_{\mathbb{R}^2\setminus U} &\leq 4\mathcal{E}_0 \left( \int_0^\infty \int_{\alpha_s^{-1}}^\infty \mathcal{F}_{H_\mathbf{1}}(\iota_1,\iota_2)\, d\iota_1\, d\iota_2 + \int_{\alpha_t^{-1}(\bar{v}_\mathrm{n}+|\bar{v}_\mathrm{t}|)}^\infty \int_0^{\alpha_s^{-1}} \mathcal{F}_{H_\mathbf{1}}(\iota_1,\iota_2)\, d\iota_1\, d\iota_2 \right) \\ &\leq \frac{4\mathcal{E}_0}{\pi} \left( \alpha_s + \frac{\alpha_t}{(\bar{v}_\mathrm{n}+|\bar{v}_\mathrm{t}|)} \right). \end{aligned}$$

□

In the limit $\alpha_i \to 0$, $i = s, t$, the support of the smoothing function $G_{\boldsymbol{\alpha}}$ tends to be the whole $\mathbb{R}^2$. This is unrealistic as the fiber length $l$ prescribes a natural upper bound for the spatial smoothing parameter $\alpha_s$. Thus, $\alpha_s = l_{\rm T}/l$ is certainly a reasonable value for the macroscopic smoothing of the turbulent flow effects on the fiber. The temporal flow and fiber scales are related to the spatial ones by the respective velocities $\bar{\mathbf{u}}$ and $\partial_t \mathbf{r}$. The choice of $\alpha_t = \alpha_s \|\partial_t \mathbf{r}\|_2/\|\bar{\mathbf{u}}\|_2$ seems likely. Consequently, the actual quality of the similarity estimates (65) and (66) is determined by the scales of the considered fiber-flow problem. Moreover, it depends crucially on the relation between fiber direction $\mathbf{t}$ and mean relative velocity $\bar{\mathbf{v}}$. Be aware that the estimates do not hold for linear dependence, because the amplitude $\mathbf{D}$ of the underlying uncorrelated velocity fluctuation field $\mathbf{z}$ is then not defined, cf. Eqs (51), (57). However, these events might be viewed as elements of a nullset, since the perturbing influence of the turbulence and the fiber inertia prevents the fiber from moving continuously within the mean streamlines.

## 4.4 Correlated and Uncorrelated Global Force

After having provided the correlated local forces $\mathbf{g}_{cc}^{\sigma,\tau}$ and their uncorrelated asymptotic limits $\mathbf{g}_{uc}^{\sigma,\tau}$, we conclude this section with the statement of the corresponding global forces. According to the Global-from-Local Force Concept (42) and the linearization approach of Eq (47), the correlated and uncorrelated global aerodynamic forces read

$$\begin{aligned}
\mathbf{f}_{cc}^{air}(\mathbf{r}(.), s, t) &= \langle \mathbf{g}_{cc}^{\sigma,\tau}(s,t)\rangle_{N(\mathbf{r}(.),s,t)} \qquad (73)\\
&= \langle \mathbf{f}(\bar{\mathbf{v}}(\sigma,\tau), \partial_s \mathbf{r}(\sigma,\tau))\rangle_{N(\mathbf{r}(.),s,t)} + \langle \mathbf{L}^{\mathbf{f}}(\sigma,\tau)\ \mathbf{w}_f^{\sigma,\tau}(s,t)\rangle_{N(\mathbf{r}(.),s,t)},\\
\mathbf{f}_{uc}^{air}(\mathbf{r}(.), s, t) &= \langle \mathbf{g}_{uc}^{\sigma,\tau}(s,t)\rangle_{N(\mathbf{r}(.),s,t)} \qquad (74)\\
&= \langle \mathbf{f}(\bar{\mathbf{v}}(\sigma,\tau), \partial_s \mathbf{r}(\sigma,\tau))\rangle_{N(\mathbf{r}(.),s,t)} + \langle \mathbf{L}^{\mathbf{f}}(\sigma,\tau)\ \mathbf{z}^{\sigma,\tau}(s,t)\rangle_{N(\mathbf{r}(.),s,t)}
\end{aligned}$$

where

$$\begin{aligned}
\langle \mathbf{L}^{\mathbf{f}}(\sigma,\tau)\ \mathbf{z}^{\sigma,\tau}(s,t)\rangle_{N(\mathbf{r}(.),s,t)} &= \sqrt{\langle \mathbf{L}^{\mathbf{f}}(\sigma,\tau)(\mathbf{D}^{\sigma,\tau})^2(\mathbf{L}^{\mathbf{f}}(\sigma,\tau))^t\rangle_{N(\mathbf{r}(.),s,t)}}\ \mathbf{p}(s,t)\\
&= \sqrt{\frac{1}{|N(\mathbf{r}(.),s,t)|}\int_{N(\mathbf{r}(.),s,t)} \mathbf{L}^{\mathbf{f}}(\sigma,\tau)(\mathbf{D}^{\sigma,\tau})^2(\mathbf{L}^{\mathbf{f}}(\sigma,\tau))^t\, d\sigma\, d\tau}\ \ \mathbf{p}(s,t)
\end{aligned}$$

by means of Ito-calculus and the integration rule of independent Gaussian random fields. Here, $(\mathbf{p}_{s,t}, (s,t) \in [0,l] \times \mathbb{R}_0^+)$ describes as $\mathbb{R}^3$-valued Gaussian white noise a centered homogeneous generalized Gaussian random field on a two-dimensional parameter set, i.e.

$$\lim_{(\triangle s, \triangle t)\to \mathbf{0}} \sqrt{\triangle s\, \triangle t}\ \mathbf{p}(s,t) \sim \mathcal{N}(\mathbf{0}, \mathbf{I}).$$

The global forces (73), (74) inherit thereby the proven approximation quality of the local forces on a macroscopic fiber scale because of the applied linear averaging procedure $< . >$.

The local flow quantities hardly ever differ in the fiber region $N$, since it is contained in the turbulence domain $M$ of Eq (12). This fact in combination with the assumption of a locally linear fiber motivates the skipping of the averaging procedure. For the further theoretical and numerical treatment in [12] it is hence convenient to consider the following approximative forces

$$\hat{\mathbf{f}}_{cc}^{air}(\mathbf{r}(.), s, t) = \mathbf{f}(\bar{\mathbf{v}}(s,t), \partial_s \mathbf{r}(s,t)) + \mathbf{L}^{\mathbf{f}}(s,t)\ \langle \mathbf{w}_f^{\sigma,\tau}(s,t)\rangle_{N(\mathbf{r}(.),s,t)}, \qquad (75)$$

$$\hat{\mathbf{f}}_{uc}^{air}(\mathbf{r}(.), s, t) = \mathbf{f}(\bar{\mathbf{v}}(s,t), \partial_s \mathbf{r}(s,t)) + \mathbf{L}^{\mathbf{f}}(s,t)\ \mathbf{D}^{s,t}\ \mathbf{p}(s,t). \qquad (76)$$

Analogously to Eq (39), the averaging brackets in Eq (75) can be explicitly formulated as Ito-integral with the Wiener process / Brownian motion $(\mathcal{W}_{\sigma,\tau}, (\sigma,\tau) \in [0,l] \times \mathbb{R}_0^+)$

$$\langle \mathbf{w}_f^{\sigma,\tau}(s,t)\rangle_{N(\mathbf{r}(.),s,t)} = \frac{1}{\sqrt{|N(\mathbf{r}(.),s,t)|}} \int_{N(\mathbf{r}(.),s,t)} \mathbf{w}_f^{\sigma,\tau}(s,t)\ d\mathcal{W}_{\sigma,\tau}.$$

Whereas the functional dependence between $\hat{\mathbf{f}}_{cc}^{air}$ and $\mathbf{r}$ remains as consequence of the realization of the correlation structure of the underlying local velocity fluctuation fields $\mathbf{w}_f^{\sigma,\tau}$, the applied simplification localizes the uncorrelated global force in Eq (76), i.e. $\hat{\mathbf{f}}_{uc}^{air}(\mathbf{r}(.), s, t) = \hat{\mathbf{f}}_{uc}^{air}(\mathbf{r}(s,t), \partial_s \mathbf{r}(s,t), \partial_t \mathbf{r}(s,t), s, t)$. Thus, the resulting fiber motion is given by a wavelike system of stochastic partial differential equations with algebraic constraint.

# 5 Conclusions and Outlook

Our presented Global-from-Local Force Concept in combination with the linearization approach (47) allows the approximation of the constructed correlated random aerodynamic force by Gaussian white noise with flow-dependent amplitude in case of a macroscopic description of the fiber dynamics. The stated general results are applicable to concrete practical problems with fiber-turbulence interaction scales that yield negligibly small deviations in the $\mathcal{L}^2$ and $\mathcal{L}^\infty$-estimates of Eqs (65), (66). Choose therefor a specific air drag model $\mathbf{f}$ and derive an appropriate linear drag operator $\mathbf{L}^{\mathbf{f}}$, then the global aerodynamic force $\hat{\mathbf{f}}^{air}_{uc}$ of Eq (76) leads to a stochastic partial differential system with additive white noise for the fiber dynamics, Eq (7), that can efficiently be handled numerically. For the exemplary choice of an empirically motivated, nearly quadratic drag model in a melt-spinning process, the effects of the correlated global force and its uncorrelated asymptotic limit that are imposed on the fiber by the turbulent flow are quantified and numerically compared in [12].

# References


[1] N. Afzal and R. Narasimha, *Axisymmetric turbulent boundary layer along a circular cylinder*, Journal of Fluid Mechanics, 74 (1976), pp. 113–128.

[2] S. S. Antman, *Nonlinear Problems of Elasticity*, Springer Verlag, New York, 1995.

[3] A. J. Chorin, *Vorticity and Turbulence*, Springer Verlag, New York, 1994.

[4] R. Core and C. Crowe, *Effect of particle size on modulating turbulent intensity*, International Journal of Multiphase Flow, 15 (1989), pp. 279–285.

[5] J. H. Ferziger and M. Perié, *Computational Methods for Fluid Dynamics*, Springer, Berlin, 3 ed., 2002.

[6] F. N. Frenkiel and P. S. Klebanoff, *Higher order correlations in a turbulent field*, Physics of Fluids A, 10 (1967), pp. 507–520.

[7] U. Frisch, *Turbulence. The Legacy of A. N. Kolmogorov*, Cambridge University Press, 1995.

[8] O. Hinze, *Turbulence*, McGraw-Hill, New York, 2 ed., 1975.

[9] S. Kruse, *A Generalized Parametrix Method, Smoothness of Random Fields and Applications to Parabolic Stochastic Partial Differential Equations*, PhD thesis, Universität Mannheim, 2001.

[10] B. E. Launder and B. I. Sharma, *Application of the energy dissipation model of turbulence to the calculation of flow near a spinning disc*, Letters in Heat and Mass Transfer, 1 (1974), pp. 131–138.

[11] N. Marheineke, *Turbulent Fibers – On the Motion of Long, Flexible Fibers in Turbulent Flows*, PhD thesis, Technische Universität Kaiserslautern, 2005.

[12] N. Marheineke and R. Wegener, *Fiber dynamics in tubulent flows II: Specific Taylor drag.* Fraunhofer-ITWM, Preprint, 2005.

[13] J. A. Olsen and R. J. Kerekes, *The motion of fibres in turbulent flow*, Journal of Fluid Mechanics, 337 (1998), pp. 47–64.

[14] H. Schlichting, *Grenzschicht-Theorie*, Verlag G. Braun, Karlsruhe, 1982.

[15] G. I. Taylor, *The spectrum of turbulence*, Proceedings of the Royal Society London, A, 164 (1938), pp. 476–490.

[16] D. C. Wilcox, *Turbulence Modeling for CFD*, DCW Industries, 2 ed., 1998.

[17] P. K. Yeung and Y. Zhou, *On the universality of the Kolmogorov constant in numerical simulations of turbulence.* NASA CR-97-206251 ICASE Report, 97-64, 1997.

# Fiber Dynamics in Turbulent Flows II
# Specific Taylor Drag


Nicole Marheineke  Raimund Wegener
marheineke@itwm.fhg.de  wegener@itwm.fhg.de
Fraunhofer-Institut für Techno- und Wirtschaftsmathematik (ITWM),
Gottlieb-Daimler-Str., Geb. 49, D-67663 Kaiserslautern, Germany


July 14, 2005


**Abstract**

In [12], an aerodynamic force concept for a general air drag model is derived on top of a stochastic $k$-$\epsilon$ description for a turbulent flow field. The turbulence effects on the dynamics of a long slender elastic fiber are particularly modeled by a correlated random Gaussian force and in its asymptotic limit on a macroscopic fiber scale by Gaussian white noise with flow-dependent amplitude. The paper at hand now presents quantitative similarity estimates and numerical comparisons for the concrete choice of a Taylor drag model in a given application.



**Keywords:** Flexible fibers; $k$-$\epsilon$ turbulence model; Fiber-turbulence interaction scales; Air drag; Random Gaussian aerodynamic force; White noise; Stochastic differential equations; ARMA process

**AMS Classification:** 74F10, 76F60, 35R60, 65C20


## 1 Introduction

The understanding of the motion of long flexible fibers suspended in highly turbulent air flows is of great interest for textiles manufacturing in the melt-spinning process of nonwoven materials. Neglecting the fiber's influence on the flow, a stochastic partial differential system that describes the dynamics of a single slender elastic fiber in a turbulent flow is stated in [12]. Thereby, the turbulence effects are modeled by a correlated Gaussian aerodynamic force. Applying a Global-from-Local Force Concept for general air drag models, it is particularly derived on basis of homogeneous Gaussian fields for the randomly fluctuating local velocity components of the flow. Their construction satisfies the requirements of the stochastic $k$-$\epsilon$ turbulence model and Kolmogorov's universal equilibrium theory on local isotropy. On macroscopic scales, white noise with flow-dependent amplitude turns out be a good approximation for the original correlated force according to $\mathcal{L}^2$ and $\mathcal{L}^\infty$-similarity estimates. In the following, we show the applicability of this general force concept under conditions of a real melt-spinning process by choosing exemplarily an empirically motivated Taylor drag. Then, the simplified force model satisfies the demands of accuracy on the relevant fiber scale while facilitates drastically the numerical computations at the same time.

For convenience we start with a brief summary of the models for fiber dynamics and aerodynamic force. Dimensional analysis of turbulence and fiber behavior reveals the characteristic interaction scales for our application in Sec 2. On the fiber macro scale the mean flow dominates the swinging of the fiber whereas the energy-bearing turbulent vortices of the meso scale cause the entanglement and fine loop forming on the fiber that are crucial for the quality of the resulting nonwoven materials. The interest in a macroscopic description of the fiber dynamics justifies the use of the simplified force model as it contains all crucial correlation informations of the meso scale according to the stated quantitative similarity estimates. From the choice of the Taylor drag model, we derive a linear drag operator and thus the concrete correlated and uncorrelated global forces in Sec 3. Their effects on the fiber dynamics are numerically compared in Sec 4 by using an introduced curvature measure which yields very convincing results.

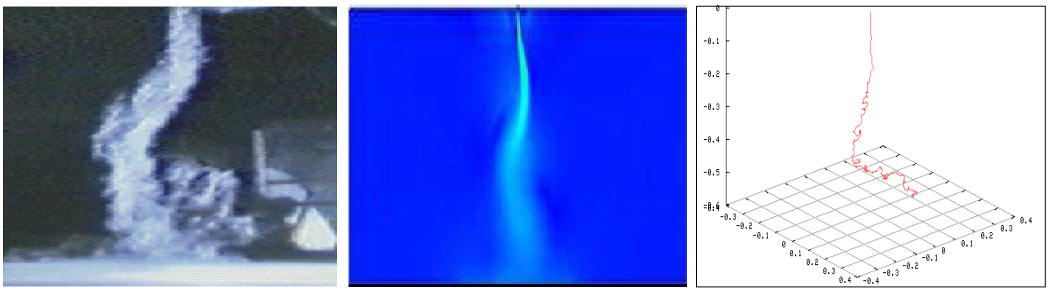

Figure 1: From left to right: Turbulent flow in melt-spinning process, mean velocity flow field by $k$-$\epsilon$ model, turbulence effects on fiber dynamics. Photo by industrial partner

### 1.1 General Aerodynamic Force Model

In the following, we recall the basic models from [12] that are crucially for the description of the fiber dynamics in a turbulent flow. Consider a single long flexible fiber that is fixed at one end, suspended in a subsonic highly turbulent air flow with small pressure gradients and Mach number Ma $< 1/3$. Let $l$ denote the fiber length and $d$ its diameter with slenderness ratio $d/l \ll 1$. Whereas the fiber influence on the turbulence is negligibly small due to the slender geometry, the turbulent flow determines essentially the dynamics of the fiber. The motion is particularly modeled by a system of stochastic partial differential equations with algebraic constraint of inextensibility that is deduced from the dynamical Kirchhoff-Love equations for a Cosserat rod being capable of large, geometrically nonlinear deformations

$$\rho A\, \partial_{tt}\mathbf{r}(s,t) = \partial_s[T(s,t)\, \partial_s\mathbf{r}(s,t)] - EI\, \partial_{ssss}\mathbf{r}(s,t) + \rho A\, \mathbf{g} + \mathbf{f}^{air}(\mathbf{r}(.),s,t) \tag{1}$$

$$\|\partial_s\mathbf{r}(s,t)\|_2 = 1, \tag{2}$$

with Dirichlet boundary conditions at the fixed end, Neumann at the free one and the position of rest as initial condition. Here, $\mathbf{r} : [0,l] \times \mathbb{R}_0^+ \to \mathbb{R}^3$ might be interpreted as center line of the fiber with arc length $s$ and time $t$, its constant line weight is denoted by $\rho A$. The internal line forces stem from bending stiffness indicated by Young's modulus $E$ and moment of inertia $I$ as well as from traction. In this spirit, the Lagrangian multiplier $T : [0,l] \times \mathbb{R}_0^+ \to \mathbb{R}$ can be viewed as modified tractive force $T = T_t + EI\|\partial_{ss}\mathbf{r}\|_2^2$ containing tension $T_t$ and curvature $\|\partial_{ss}\mathbf{r}\|_2^2$ due to bending. The external line forces acting on the fiber arise from gravity $\mathbf{g}$ and aerodynamics $\mathbf{f}^{air}$.

The aerodynamic force term acts as additive Gaussian noise in Eq (1) due to the applied general Global-from-Local Force Concept that is based on the stochastic $k$-$\epsilon$ description of the underlying turbulent flow. In particular, we consider here a correlated Gaussian aerodynamic force $\mathbf{f}_{cc}^{air}$ and its uncorrelated asymptotic limit on macroscopic scales $\mathbf{f}_{uc}^{air}$

$$\mathbf{f}_{cc}^{air}(\mathbf{r}(.),s,t) = \mathbf{f}(\bar{\mathbf{v}}(s,t), \partial_s\mathbf{r}(s,t)) + \mathbf{L}^{\mathbf{f}}(s,t)\, \frac{\int_{N(\mathbf{r}(.),s,t)} \mathbf{w}_f^{\sigma,\tau}(s,t)\, d\mathcal{W}_{\sigma,\tau}}{(\int_{N(\mathbf{r}(.),s,t)} d\sigma\, d\tau)^{1/2}} \tag{3}$$

$$\mathbf{f}_{uc}^{air}(\mathbf{r}(.),s,t) = \mathbf{f}(\bar{\mathbf{v}}(s,t), \partial_s\mathbf{r}(s,t)) + \mathbf{L}^{\mathbf{f}}(s,t)\; \mathbf{D}^{s,t}\; \mathbf{p}(s,t) \tag{4}$$

that depend on the chosen air drag model $\mathbf{f} : \mathbb{R}^3 \times \mathbb{R}^2 \to \mathbb{R}^3$ and its respective linear drag operator $\mathbf{L}^{\mathbf{f}}$. A feasible air drag model is prescribed as function of the mean relative velocity between fluid and fiber, i.e. $\bar{\mathbf{v}}(s,t) = \bar{\mathbf{u}}(\mathbf{r}(s,t),t) - \partial_t\mathbf{r}(s,t)$, and the fiber tangent $\partial_s\mathbf{r}(s,t)$. In analogy to the $k$-$\epsilon$ turbulence model, the forces are split into a deterministic part $\bar{\mathbf{f}}$ resulting from the mean flow velocity $\bar{\mathbf{u}} : \mathbb{R}^3 \times \mathbb{R}_0^+ \to \mathbb{R}^3$ and a stochastic part $\mathbf{f}'$ coming from the turbulent fluctuations that are characterized by the turbulent kinetic energy $k : \mathbb{R}^3 \times \mathbb{R}_0^+ \to \mathbb{R}^+$ and the dissipation rate $\epsilon : \mathbb{R}^3 \times \mathbb{R}_0^+ \to \mathbb{R}^+$. In Eq (3) the random fluctuations are modeled as Ito-integral over a family of locally isotropic, homogeneous, incompressible Gaussian velocity fields along the fiber $\{(\mathbf{w}_f^{\sigma,\tau})_{s,t}, (s,t) \in [0,l] \times \mathbb{R}_0^+), (\sigma,\tau) \in [0,l] \times \mathbb{R}_0^+\}$, where $(\mathcal{W}_{\sigma,\tau}, (\sigma,\tau) \in [0,l] \times \mathbb{R}_0^+)$ denotes a Wiener process (Brownian motion). The underlying fiber region $N(\mathbf{r}(.),s,t) = \{(\sigma,\tau) \in [0,l] \times \mathbb{R}_0^+ |\; \|\mathbf{r}(s,t) - \mathbf{r}(\sigma,\tau) - \bar{\mathbf{u}}(\mathbf{r}(s,t),t)(t-\tau)\|_2 \leq l_{\mathrm{T}} \wedge |t-\tau| \leq t_{\mathrm{T}}\}$ is determined by the turbulent large-scale length $l_{\mathrm{T}}$ and time $t_{\mathrm{T}}$. Moreover, the construction of the correlation tensors $\boldsymbol{\gamma}_0^{\sigma,\tau}$ that correspond to the centered velocity fields complies with the requirements of the $k$-$\epsilon$

| Fiber | | | |
|---|---|---|---|
| diameter | $d$ | $3.0 \cdot 10^{-5}$ | m |
| length | $l$ | 2.5 | m |
| line weight | $\rho A$ | $9.0 \cdot 10^{-7}$ | kg/m |
| bending stiffness | $EI$ | $4.7 \cdot 10^{-10}$ | Nm$^2$ |
| absolute velocity | $W$ | $1.0 \cdot 10^{1}$ | m/s |
| acceleration of gravity | $g$ | 9.81 | m/s$^2$ |
| suspended height | $H$ | 1 | m |
| **Flow** | | | |
| density | $\rho^{air}$ | 1.22 | kg/m$^3$ |
| absolute mean velocity | $\bar{u}$ | $1.0 \cdot 10^{2}$ | m/s |
| turbulent kinetic energy | $k$ | $1.0 \cdot 10^{2}$ | m$^2$/s$^2$ |
| dissipation rate | $\epsilon$ | $1.0 \cdot 10^{5}$ | m$^2$/s$^3$ |
| viscosity | $\nu$ | $1.5 \cdot 10^{-5}$ | m$^2$/s |

Table 1: Typical fiber and flow parameter values in melt-spinning processes

model, Kolmogorov's universal equilibrium theory on local isotropy as well as Taylor's hypothesis of frozen turbulence pattern by choosing the following energy spectra $E^{\sigma,\tau} \in \mathcal{C}^2(\mathbb{R}_0^+)$

$$E^{\sigma,\tau}(\kappa) = \begin{cases} K^{\sigma,\tau}\, \kappa_1^{-5/3}\, \sum_{j=4}^{6} a_j\, (\frac{\kappa}{\kappa_1})^j & \kappa < \kappa_1 \\ K^{\sigma,\tau}\, \kappa^{-5/3} & \kappa_1 \leq \kappa \leq \kappa_2 \\ K^{\sigma,\tau}\, \kappa_2^{-5/3}\, \sum_{j=7}^{9} b_j\, (\frac{\kappa}{\kappa_2})^{-j} & \kappa > \kappa_2 \end{cases} \tag{5}$$

$$\int_0^\infty E^{\sigma,\tau}(\kappa)\, d\kappa = k(\mathbf{r}(\sigma,\tau),\tau), \qquad \int_0^\infty E^{\sigma,\tau}(\kappa)\, \kappa^2\, d\kappa = \frac{\epsilon(\mathbf{r}(\sigma,\tau),\tau)}{2\nu} \tag{6}$$

with viscosity $\nu$, Kolmogorov constant $K^{\sigma,\tau} = C_{\mathrm{K}}\, \epsilon(\mathbf{r}(\sigma,\tau),\tau)^{2/3}$ and further prescribed constant fitting parameters $a_j$, $b_j$. In Eq (4) in contrast, the integral effects of the localized random fluctuations are incorporated in the amplitude $\mathbf{D}^{s,t}$ of the Gaussian white noise $(\mathbf{p}_{s,t}, (s,t) \in [0,l] \times \mathbb{R}_0^+)$. In particular,

$$\mathbf{D}^{s,t} = \left( \frac{2\pi}{\bar{v}_{\mathrm{n}}(s,t)} \int_0^\infty \frac{E^{s,t}(\kappa)}{\kappa^2}\, d\kappa \right)^{1/2} \mathbf{P}_{\mathbf{t},\mathbf{n}(s,t)} \tag{7}$$

is proportional to the projector onto the plane spanned by fiber tangent $\mathbf{t} = \partial_s \mathbf{r}$ and normal $\mathbf{n} = (\bar{\mathbf{v}} - (\bar{\mathbf{v}} \cdot \mathbf{t})\mathbf{t})/\|\bar{\mathbf{v}} - (\bar{\mathbf{v}} \cdot \mathbf{t})\mathbf{t}\|_2$, where $\bar{v}_{\mathrm{n}} = \bar{\mathbf{v}} \cdot \mathbf{n}$. Note that the existence of the amplitude in Eq (7) and thus of the uncorrelated force in Eq (4) presupposes the linear independence of fiber tangent and mean relative velocity.

# 2 Fluid-Fiber Interaction Scales

The handling of fiber-turbulence interaction is very difficult as it is governed by many complex factors, including nature of flow field, turbulent length scales, size and behavior of the fiber. The applicability of the uncorrelated aerodynamic force $\mathbf{f}_{uc}^{air}$ particularly depends on the characteristic interaction scales of the considered fiber-flow problem. In a typical melt-spinning process, fiber and flow are specified by the parameter values of Tab 1. These yield the following quantitative scales and similarity estimates between the correlated and the uncorrelated force by using dimensional analysis.

## 2.1 Turbulence Scales

Turbulence is characterized by its wide range of length and time scales. As their significance plays a decisive role in the coming analysis we focus on them and their interpretation.

Due to the underlying $k$-$\epsilon$ turbulence model we already distinguish between the length and time scales of the mean motion and the ones of the fluctuations. The mean motion and its scales are concluded from the boundary conditions (geometry) and the absolute mean flow velocity $\bar{u}$. On the other hand, the fluctuations might be interpreted as the turbulent effects of overlapping vortices of different sizes that are indicated by the turbulent kinetic energy $k$, dissipation rate $\epsilon$ and viscosity $\nu$. The smallest, viscously determined vortices are given by the Kolmogorov scales

$$\eta = \left(\frac{\nu^3}{\epsilon}\right)^{1/4}, \qquad t_{\mathrm{K}} = \left(\frac{\nu}{\epsilon}\right)^{1/2}.$$

Apart from that, the local correlation tensor $\boldsymbol{\gamma}_0$ [11, 12] provides additional information about the size of the present turbulent structures. The structures in the dissipation area (small lengths, thus high frequencies) are determined by the run of the one-dimensional longitudinal correlation function $c_1(z) = 2/z^3 \int_0^\infty \partial_\kappa(E(\kappa)/\kappa)\sin(\kappa z)\,d\kappa$, $z \in \mathbb{R}_0^+$ around the origin and hence by $k$ and $\epsilon$, see Eq (6). For $z \ll 1$, then $c_1(z) = 2/3k - \epsilon/(30\,\nu)\,z^2 + \mathcal{O}(z^4)$ describes a parabola that intersects the $z$-axis at the dissipation length $\lambda_{\mathrm{T}}$, i.e. $c_1(\lambda_{\mathrm{T}}) = 0$. Thus,

$$\lambda_{\mathrm{T}} = \left(\frac{20k\nu}{\epsilon}\right)^{1/2}$$

represents as turbulent fine or micro scale the decay of the correlations.

The large, macro or integral scale

$$\Lambda_{\mathrm{T}} = \frac{\int_0^\infty \mathrm{tr}\boldsymbol{\gamma}_0(z)\,dz}{\mathrm{tr}\boldsymbol{\gamma}_0(0)} = \frac{\pi}{2}\frac{\int_0^\infty E(\kappa)/\kappa\,d\kappa}{\int_0^\infty E(\kappa)\,d\kappa}$$

in contrast, characterizes the mean coherence scale independently of longitudinal and lateral correlations and can be be interpreted as typical size of the energy-bearing vortices. In this context, the turbulent length proposed by the $k$-$\epsilon$ model

$$l_{\mathrm{T}} = \frac{k^{3/2}}{\epsilon}$$

can be understood as the leading order term of $\Lambda_{\mathrm{T}}$. Consider therefor the modeled energy spectrum of Eq (5), it gives

$$\Lambda_{\mathrm{T}} = \frac{\pi\,C_{\mathrm{K}}}{2}\frac{\epsilon^{2/3}}{k}\left(A_1\kappa_1^{-5/3} + B_1\kappa_2^{-5/3}\right)\Big($$

where $\kappa_1$ and $\kappa_2$ with $\kappa_2 > \kappa_1 > 0$ are the solutions of the nonlinear system

$$\begin{aligned} A_k\kappa_1^{-2/3} + B_k\kappa_2^{-2/3} &= \frac{k}{C_{\mathrm{K}}\epsilon^{2/3}} = f_k, \\ A_\epsilon\kappa_1^{4/3} + B_\epsilon\kappa_2^{4/3} &= \frac{\epsilon^{1/3}}{2C_{\mathrm{K}}\nu} = f_\epsilon = \frac{f_k}{\delta^2}, \end{aligned} \tag{8}$$

stemming from Eq (6). After non-dimensionalizing, $\delta = (2k\nu/\epsilon)^{1/2} \sim \mathcal{O}(\lambda_{\mathrm{T}})$ with $\lambda_{\mathrm{T}}/H \ll 1$ turns out to be small, whereas the other coefficients $A_i, B_i, f_k \sim \mathcal{O}(1)$. Thereby, $A_i$, $B_i$, $i = 1, k, \epsilon$ denote linear combinations of the fitting parameters arising in Eq (5) and $C_{\mathrm{K}} = 0.5$ the Kolmogorov constant. Substituting $x_i = \kappa_i^{2/3}$, $i = 1, 2$, we write $x_1 = f_k/A_k - B_k/A_k\,x_2$. Plugging this expression into Eq (8) yields a $4^{\text{th}}$ order equation for $x_2$ that has two complex, a negative and a positive solution. The feasible positive solution can be expanded in $\delta$ as $x_2 = x_2^{(1)}\delta + x_2^{(3)}\delta^3 + \mathcal{O}(\delta^4)$ which results straightforward in a $\delta$-series for $\Lambda_{\mathrm{T}}$

$$\Lambda_{\mathrm{T}} = F_1\,l_{\mathrm{T}} + \mathcal{O}(\delta), \qquad \text{with } F_1 = \frac{\pi}{2}\frac{A_1}{C_{\mathrm{K}}^{3/2}\,A_k^{5/2}} \approx 1.05. \tag{9}$$

Though the use of $A_i$ in Eq (9), the magnitude of $F_1$ can be treated as independent of the differentiability order of the underlying chosen energy model. An ansatz for a smoother energy spectrum, $E \in \mathcal{C}^l(\mathbb{R}_0^+)$, $l \geq 3$, contains certainly more fitting parameters but their influence cancels out in the definition of $F_1$. In this work, we refer to $l_{\mathrm{T}}$ as turbulent large-scale length.

Concerning the turbulent time scale for the decay of the energy-bearing vortices, the length $l_{\mathrm{T}}$ and velocity scale $u_{\mathrm{T}} = k^{1/2}$ of the $k$-$\epsilon$ model imply

$$t_{\mathrm{T}} = \frac{k}{\epsilon}.$$

As this scale disregards the advective influence of the mean flow, we suggest additionally

$$t_{\mathrm{A}} = \frac{l_{\mathrm{T}}}{\bar{u}} = \frac{k^{3/2}}{\epsilon\,\bar{u}}.$$

Moreover, the amplitude $\mathbf{D}$ of the uncorrelated force in Eq (7) might be also expressed by $k$ and $\epsilon$, since it contains a moment of the energy spectrum. In our case, we get $\int_0^\infty E(\kappa)/\kappa^2\,d\kappa = C_{\mathrm{K}}\epsilon^{2/3}(A_2\kappa_1^{-8/3} + B_2\kappa_2^{-8/3})$, where $A_2$, $B_2 \sim \mathcal{O}(1)$ are linear combinations of the fitting parameters. Following the approach above and introducing the small parameter $\delta$, the expansion for the energy moment reads

$$\int_0^\infty \frac{E(\kappa)}{\kappa^2}\,d\kappa = F_2\,\frac{k^4}{\epsilon^2} + \mathcal{O}(\delta), \qquad \text{with } F_2 = \frac{A_2}{C_{\mathrm{K}}^3\,A_k^4} \approx 0.80, \tag{10}$$

In leading order, the amplitude is consequently given by

$$\mathbf{D}^{(0)} = \left(\frac{2\pi F_2}{\bar{v}_{\mathrm{n}}}\right)^{1/2} \frac{k^2}{\epsilon} \quad \mathbf{P}_{\mathbf{t},\mathbf{n}} \tag{11}$$

Thus, the resulting correlations along the fiber $(\mathbf{D}^{(0)})^2\,\delta_0(s)\,\delta_0(t)$ can be interpreted to be proportional to the turbulent energy $k$ acting over the mean coherence length $l_{\mathrm{T}}$ and over the characteristic turbulent fiber time $\tau_{\mathrm{T}}^f = l_{\mathrm{T}}/\bar{v}_{\mathrm{n}}$ that depends on the geometrical relation between fiber orientation and mean relative velocity.

## 2.2 Fiber Scales

For a better understanding of the fiber behavior in the turbulent flow, dimensional analysis is applied on the fiber system (1), (2). Therefor, we introduce a dimensionless zooming parameter $h = L/H$ as ratio of the typical varying length of interest $L$ and the fixed height of the suspended fiber $H$.

Apart from $H$, the problem contains nine further parameters: diameter $d$, line weight $\rho A$, bending stiffness $EI$, fiber velocity $W$, acceleration of gravity $g$, flow density $\rho^{air}$, mean flow velocity $\bar{u}$, mean relative velocity between flow and fiber $\bar{v}$ and kinetic turbulent energy $k$. The number of parameters can be reduced to four dimensionless

$$\mathrm{Fr} = \frac{W^2}{g\,H}, \quad \mathrm{Gr} = \frac{\rho A\,g\,H^3}{EI}, \quad \bar{\mathrm{P}} = \frac{d\,\rho^{air}\,H^3\,\bar{v}^2}{EI}, \quad \mathrm{P}' = \frac{d\,\rho^{air}\,H^3\,k^{1/2}\,\bar{v}}{EI}.$$

The Froude number Fr states the ratio of kinetic and gravitational potential energy, the dimensionless gravity Gr the ratio of gravitational and flexural energies and the dimensionless mean $\bar{\mathrm{P}}$ resp. fluctuating aerodynamic force $\mathrm{P}'$ the ratio of aerodynamic and flexural energies. Introducing dimensionless variables gives

$$\mathbf{r}(s,t) = H\ r^*(s^*,t^*), \qquad T_t(s,t) = \frac{EI}{L\,H}\ T_t^*(s^*,t^*),$$

$$\bar{\mathbf{f}}(s,t) = d\,\rho^{air}\left(\frac{\bar{v}}{h}\right)^2 \bar{\mathbf{f}}^*(s^*,t^*), \qquad \mathbf{f}'(s,t) = d\,\rho^{air}k^{1/2}\left(\frac{\bar{v}}{h}\right)\ \mathbf{f}'^*(s^*,t^*),$$

with $s = L\,s^*$ and $t = (L/W)\,t^*$. The use of different length scalings for $\mathbf{r}$ and $s$ are motivated from our interest to keep the whole spatial domain of the fiber line while focusing on the fiber behavior arising on typical lengths. Hence, the interplay of fixed outer $H$ and varying inner length $L$ appears also in the factor of the tension part $T_t$. The bending part is treated separately due to the composed structure of $T$. For the scaling of the aerodynamic force $\mathbf{f}^{air}$, it is sufficient to utilize its proportionality to the dynamic pressure, since $\|\mathbf{f}^{air}\|_2 \sim d\rho^{air}\|\mathbf{v}\|_2^2$ in the following. Thereby, the deterministic force part $\bar{\mathbf{f}}$ is based on the quadratic mean relative velocity and the stochastic part $\mathbf{f}'$ on the product of mean relative velocity and flow fluctuations that are expressed by $k^{1/2}$. The magnitude of the mean relative velocity $\bar{v}$ depends particularly on the direction of mean flow and fiber velocity according to

$$\bar{\mathbf{v}}(s,t) = \|\bar{u}\,\bar{\mathbf{u}}^* - W/h\ \partial_{t^*}\mathbf{r}^*\|_2\ \bar{\mathbf{v}}^*(s^*,t^*) = (\bar{v}/h)\,\bar{\mathbf{v}}^*(s^*,t^*). \tag{12}$$

It is minimal if $\bar{\mathbf{u}}^\star$ and $\partial_{t^\star}\mathbf{r}^\star$ are similar directed, maximal if they are opposite directed, thus $\bar{v} \in [\,|h\bar{u} - W|, |h\bar{u} + W|\,]$. The time scaling in Eq (12) that is chosen with respect to the fiber dynamics of the typical length $L$ incorporates here the zooming ratio $h$ in the definition of $\bar{v}$. Then, the dimensionless fiber system reads

$$\begin{aligned}
\mathrm{Fr}\,\mathrm{Gr}\,\partial_{tt^\star}\mathbf{r}^\star &= \partial_{s^\star}((h^{-1}\,T_t^\star + h^{-4}\,\|\partial_{ss^\star}\mathbf{r}^\star\|_2^2)\,\partial_{s^\star}\mathbf{r}^\star) - h^{-2}\,\partial_{ssss^\star}\mathbf{r}^\star - h^2\,\mathrm{Gr}\,\mathbf{e_3}\\
&\quad + \bar{\mathrm{P}}\,\bar{\mathbf{f}}^\star + h\,\mathrm{P}'\,\mathbf{f}'^\star\\
(\partial_{s^\star}\mathbf{r}^\star)^2 &= h^2.
\end{aligned}$$

For a melt-spinning process, the typical fiber and flow parameter values listed in Tab 1 yield

$$\mathrm{Fr} \sim 10^1, \quad \mathrm{Gr} \sim 10^4, \quad \bar{\mathrm{P}} \sim \begin{cases} 10^8 - 10^9, & h \sim 1\\ 10^6 - 10^7, & h \ll 1 \end{cases}, \quad \mathrm{P}' \sim \begin{cases} 10^7 - 10^8, & h \sim 1\\ 10^6 - 10^7, & h \ll 1 \end{cases}$$

where the aerodynamic similarity quantities $\bar{\mathrm{P}}$ and $\mathrm{P}'$ are roughly estimated by means of the range of $\bar{v}$.

Varying the length of interest $L$ and thus the zooming parameter $h$ reveals three characteristic scales that are worth to consider in more detail, cf. Fig 2. In the following we suppress the superscript $^*$ to keep the expressions short.

**Macro scale:** $1 \geq h > 10^{-1}$

$$\mathrm{Fr}\,\mathrm{Gr}\,\partial_{tt}\mathbf{r} = -h^2\,\mathrm{Gr}\,\mathbf{e_3} + \bar{\mathrm{P}}\,\bar{\mathbf{f}} + h\,\mathrm{P}'\,\mathbf{f}'$$

Over the whole length of the fiber $l$, the fiber dynamics is caused by the external forces. In particular, the mean flow affects the fiber swinging.

**Meso scale:** $10^{-1} \geq h > 10^{-3}$

$$\mathrm{Fr}\,\mathrm{Gr}\,\partial_{tt}\mathbf{r} = \partial_s((h^{-1}T_t + h^{-4}\|\partial_{ss}\mathbf{r}\|_2^2)\,\partial_s\mathbf{r}) - h^{-2}\,\partial_{ssss}\mathbf{r} + \bar{\mathrm{P}}\,\bar{\mathbf{f}} + h\,\mathrm{P}'\,\mathbf{f}'$$

This fiber scale coincides with the turbulent large-scale $l_\mathrm{T}$ of the energy-bearing vortices. Here, the inner and outer forces acting on the fiber balance each other. But the fluctuating part of the aerodynamic force $\mathbf{f}'$ causes entanglement and fine-loop forming which crucially determine the fiber dynamics.

**Micro scale:** $h \leq 10^{-3}$

$$\partial_s(h^{-4}\|\partial_{ss}\mathbf{r}\|_2^2\,\partial_s\mathbf{r}) = \mathbf{0}, \qquad \mathrm{Fr}\,\mathrm{Gr}\,\partial_{tt}\mathbf{r} = -h^{-2}\,\partial_{ssss}\mathbf{r} + \bar{\mathrm{P}}\,\bar{\mathbf{f}}$$

The inner forces, in particular the bending stiffness, dominate the total fiber behavior. In contrast, the effects of the fine-scale $\lambda_\mathrm{T}$ and Kolmogorov vortices of size $\eta$ are irrelevant for the fiber dynamics, here $\eta < d$.

The time scales of the problem provide no further information as they are related to the length scales using the reciprocal of the fiber velocity $W$ as proportionality factor. Due to its inertia, the fiber shows thus no reaction to turbulent structures decaying faster than $t_{inertia} \sim 10^{-4}$ s which includes the whole fine-scale turbulence. The natural decay of the large-scale vortices in contrast is indicated by $t_\mathrm{T} \sim 10^{-3}$ s and under consideration of advection by the mean flow by $t_\mathrm{A} \sim 10^{-4}$ s.

Summing up, fine-scale vortices do absolutely not affect a fiber in the melt-spinning process due to its bending stiffness. Thus, their influence (correlations) might be neglected in the model of the stochastic aerodynamic force. The turbulent large-scale vortices in contrast cause entanglement and loop-forming that play a decisive role for the fiber behavior. But instead of resolving their effects explicitely, it is sufficient to model them on the macro scale, as our interest focuses exclusively on a macroscopic description for the fiber dynamics. This motivates the idea of approximating the correlated force by an integrated – still correlated – force. In the following, the introduced uncorrelated aerodynamic force $\mathbf{f}_{uc}^{air}$ of Eq (4) that contains the mean turbulent coherences (integral correlations) turns out to satisfy the stated demands on approximability.

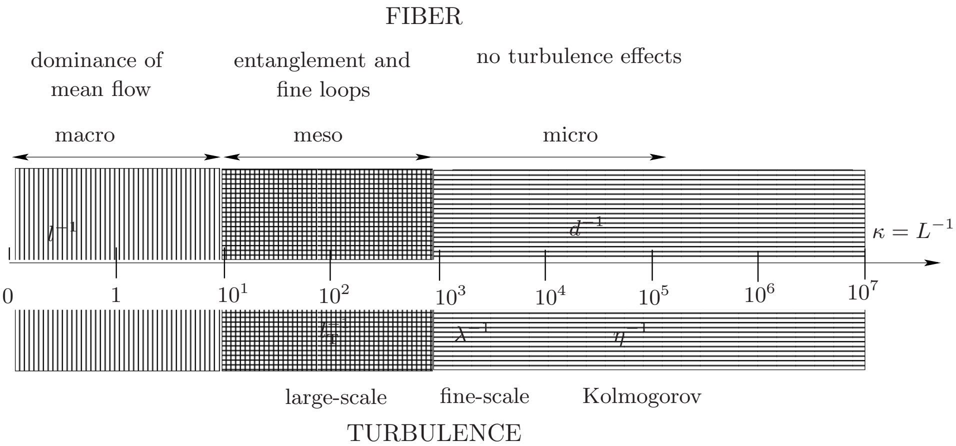


Figure 2: Scales of fiber-turbulence interactions

## 2.3 Quantitative Similarity Estimates

To justify the applicability of the uncorrelated force as substitute of the original correlated force in our problem, we analyze its approximation properties by means of the similarity estimates taken from [12].

**Similarity Estimates**
*Let $\alpha_s$ and $\alpha_t \in \mathbb{R}_0^+$ be spatial and temporal smoothing parameters of the fiber-flow problem. Define $\mathcal{E}(\kappa_1,\kappa_2) := \int_{\mathbb{R}} E(\|\kappa_1,\kappa_2,l\|_2)/(\kappa_1,\kappa_2,l)^2\, dl$ with $\mathcal{E}_0 := \mathcal{E}(0,0)$ and $\mathcal{S} := \sup_{\boldsymbol{\kappa}\in[0,1]^2} \|\nabla_{\boldsymbol{\kappa}} \mathcal{E}(\kappa_1,\kappa_2)\|_2$. Then, the approximability of the correlated by the uncorrelated aerodynamic force given in Eqs (3), (4) is expressed by the following estimates:*
*$\mathcal{L}^2$-similarity:*

$$\mathcal{I}_{\mathcal{L}^2} \leq \frac{\sqrt{\alpha_s\,\alpha_t}}{\sqrt{6}\,\pi\,\bar{v}_\mathrm{n}} \sqrt{\mathcal{S}^2\left(\alpha_s^2\,(1+\frac{\bar{v}_\mathrm{t}^2}{\bar{v}_\mathrm{n}^2}) + \frac{\alpha_t^2}{\bar{v}_\mathrm{n}^2}\right) + \frac{8\mathcal{E}_0^2}{3\pi}\left(\alpha_s^3 + \frac{\alpha_t^3}{(\bar{v}_\mathrm{n}+|\bar{v}_\mathrm{t}|)^3}\right)} \tag{13}$$

*$\mathcal{L}^\infty$-similarity:*

$$\begin{aligned}\mathcal{I}_{\mathcal{L}^\infty} \leq \frac{\sqrt{2}\,\alpha_s\,\alpha_t}{\pi^2\,\bar{v}_\mathrm{n}} \Bigg[ & \mathcal{S}\left(\alpha_s\,(1+\frac{\bar{v}_\mathrm{t}}{\bar{v}_\mathrm{n}})\left(\frac{c}{2}+\ln(\frac{1}{\alpha_s})\right) + \frac{\alpha_t}{\bar{v}_\mathrm{n}}\left(\frac{c}{2}+\ln(\frac{\bar{v}_\mathrm{n}+|\bar{v}_\mathrm{t}|}{\alpha_t})\right)\right) \\ & + \mathcal{E}_0\left(\alpha_s + \frac{\alpha_t}{\bar{v}_\mathrm{n}+|\bar{v}_\mathrm{t}|}\right)\Bigg]\end{aligned} \tag{14}$$

*where $\bar{v}_\mathrm{t}$, $\bar{v}_\mathrm{n}$ are the tangential and normal component of the mean relative velocity with respect to the $(\mathbf{t},\bar{\mathbf{v}})$-induced fiber basis of Sec 1.1 and $c = \int_0^1 (1-\cos\iota)/\iota\, d\iota$.*

The limit $\alpha_i \to 0$, $i = s,t$ describes the smoothing over the whole $\mathbb{R}^2$. This is unrealistic as the fiber length $l$ prescribes a natural upper bound for the spatial smoothing parameter $\alpha_s$. Thus, $\alpha_s = l_\mathrm{T}/l$ is certainly a reasonable value for the macroscopic description of the turbulent flow effects on the fiber. The temporal flow and fiber scales are related to the spatial ones by the respective velocities $\bar{u}$ and $W$ which motivates the choice of $\alpha_t = t_\mathrm{A}W/l = \alpha_s W/\bar{u}$.

Inserting the typical parameter values of Tab 1 yields for the non-dimensionalized quantities $\alpha_s \sim 10^{-2}$, $\alpha_t \sim 10^{-3}$, $\mathcal{S} \sim 1$ and $\mathcal{E}_0 \sim k^4/\epsilon^2 \sim 10^{-2}$ according to Eq (10). The order of the relative velocity can be approximated by $\bar{v} \sim 10^2$ which implies $|\bar{v}_\mathrm{t}| \in [0,10^2]$ and $\bar{v}_\mathrm{n} \in [0,10^2]$. Thus, quantitative similarity estimates in SI-units depend drastically on the relation between fiber direction $\mathbf{t} = \partial_s \mathbf{r}$ and mean relative velocity $\bar{\mathbf{v}}$ as they are expressed by

$$\mathcal{I}_{\mathcal{L}^2}^2 \lesssim 10^{-10}\,\bar{v}_\mathrm{n}^{-2} + 10^{-6}\,\bar{v}_\mathrm{n}^{-4}, \qquad \mathcal{I}_{\mathcal{L}^\infty} \lesssim 10^{-8}\,\bar{v}_\mathrm{n}^{-1} + 10^{-6}\,\bar{v}_\mathrm{n}^{-2}.$$

with $\mathbf{n} = (\bar{\mathbf{v}} - (\bar{\mathbf{v}}\cdot\mathbf{t})\mathbf{t})/\|\bar{\mathbf{v}} - (\bar{\mathbf{v}}\cdot\mathbf{t})\mathbf{t}\|_2$. In case of $\mathbf{t} \perp \bar{\mathbf{v}}$, we have $\bar{v}_\mathrm{n} \sim 10^2$ such that $\mathcal{I}_{\mathcal{L}^2} \lesssim 10^{-7}$ and $\mathcal{I}_{\mathcal{L}^\infty} \lesssim 10^{-10}$ indicate very good approximation properties. But even for smaller normal velocity components – down to $\bar{v}_\mathrm{n}^{crit} \sim 10^{-1}$ – the uncorrelated force is a good substitute for the correlated one, since the deviations are little, i.e. $\mathcal{I}_{\mathcal{L}^2} \lesssim 10^{-1}$, $\mathcal{I}_{\mathcal{L}^\infty} \lesssim 10^{-4}$. In fact, $\bar{v}_{\mathrm{n}} \sim 1$ in general, and the events $\bar{v}_{\mathrm{n}} < \bar{v}_{\mathrm{n}}^{crit}$ might be viewed as elements of a nullset, because the perturbing influence of turbulence and fiber inertia prevents the fiber from moving continuously within the mean streamlines. However, the further numerical realization requires also their treatment so that we will deal with the arising singularity for $\bar{v}_{\mathrm{n}} \to 0$ in Sec 3.3 which results from the definition of the force amplitude $\mathbf{D}$, Eq (7).

# 3 Air Drag Model and its Consequences

The numerical simulations of the fiber dynamics imposed by the correlated and/or uncorrelated aerodynamic force rely essentially on the choice of an appropriate air drag model $\mathbf{f}$ and the derivation of the corresponding linear drag operator $\mathbf{L}^{\mathbf{f}}$. We particularly distinguish between linear and quadratic drag relations and discuss their applicability as well as their consequences for our application.

## 3.1 Choice of Drag Model

**Stokes Drag for Turbulent Flow**

For slow viscous flows with $\mathrm{Re} < 1$, Cox [4] has developed an insightful analytical series approximation for the force distribution along the length $l$ of a straight fiber. As Reynolds number based on the fiber diameter $d$ approaches zero, the drag force per unit length along the fiber is proportional to the relative velocity between fluid and fiber $\mathbf{v}(s,t) = \mathbf{u}(\mathbf{r}(s,t),t) - \partial_t \mathbf{r}(s,t)$ at fiber point $s$ and time $t$. So,

$$\mathbf{f}(\mathbf{v},\mathbf{t}) = \mathbf{C}^{drag}(\mathbf{t})\ \mathbf{v}, \qquad \mathbf{C}^{drag}(\mathbf{t}) = c_{\mathrm{t}}\, \mathbf{t} \otimes \mathbf{t} + c_{\mathrm{n}}\, (\mathbf{I} - \mathbf{t} \otimes \mathbf{t}) \tag{15}$$

gives the linear Stokes drag relation, where the drag tensor $\mathbf{C}^{drag}$ depends on the fiber orientation $\mathbf{t} = \partial_s \mathbf{r}$ in the surrounding flow. From the Stokes flow approximation, Keller and Rubinow [9] have determined the drag coefficients $c_{\mathrm{n}}$, $c_{\mathrm{t}}$ up to leading order for smooth ellipsoidal filaments which also conform for small surface variations [1]. Götz [7], in contrast, has derived an integral equation model for the drag force by applying a matching principle to the asymptotic expansions of the flow field around slender ellipsoidal and cylindrical fibers of circular cross-sections in the framework of Stokes' and Oseen's equations. Then with $\mu = \rho^{air}\nu$

$$c_{\mathrm{n}}^{ellipsoid} = \frac{8\pi\mu}{\mathrm{Re}} \left( \ln(\frac{2l}{d}) + \frac{1}{2} \right)^{-1}, \qquad c_{\mathrm{t}}^{ellipsoid} = \frac{4\pi\mu}{\mathrm{Re}} \left( \ln(\frac{2l}{d}) - \frac{1}{2} \right)^{-1},$$

$$c_{\mathrm{n}}^{cylinder} = \frac{8\pi\mu}{\mathrm{Re}} \left( \ln(\frac{4l}{d}) - \frac{1}{2} \right)^{-1}, \qquad c_{\mathrm{t}}^{cylinder} = \frac{4\pi\mu}{\mathrm{Re}} \left( \ln(\frac{4l}{d}) - \frac{3}{2} \right)^{-1}.$$

However, there is no slender-body theory that is strictly valid for the turbulent flow with high Re that is of interest here, $\mathrm{Re} \approx 200$. In the analysis of turbulence effects on particles, a linear Stokes drag has successfully been applied to predict particle motions in turbulent flows [14, 15, 17, 19]. Drag relations based on empirical correlations have also been used [3, 13] as well as a modified Stokes drag that takes into account particle oscillations [8]. As a necessary simplification, the form of the drag force, Eq (15), on the fiber under creeping flow conditions is assumed to be retained for high Re turbulent flows. But Eq (15) has been derived for a small Reynolds number flow. Thus, it is only valid for infinitely thin little fibers with $d \leq \eta$ and $l \leq \eta$. Anyhow, the relation is conferrable to longer fibers suspended in turbulent flow by imposing the free-draining approximation which has been used to model flexible fiber motion [16] and polymer dynamics [6]. In this model, the fiber is considered to be composed of a series of elements of length $\Delta_l$, where $\Delta_l \leq \eta$. Each element meets the necessary conditions for Eq (15) to be valid. Assuming hydrodynamic independence of each element allows Eq (15) to be applied to all elements and thus to the entire fiber.

**Taylor Drag**

For high Reynolds number flow indicated by $\mathrm{Re} \in (20, 10^6)$, Taylor [18] has investigated the behavior of drag forces experimentally. Thereby, he has discovered the nonlinear relation between drag and angle $\alpha$ enclosed by flow direction and center line of an immersed straight slender body as well as the influence of the surface roughness on the drag, which Lee [10] has applied successfully to long, flexible fibers within a carding process.

As the drag force $\mathbf{f}$ lies in the plane spanned by the fiber tangent and the relative velocity, it can be split into a tangential $\mathbf{f_t}$ and a normal component $\mathbf{f_n}$ with respect to the fiber orientation, i.e. $\mathbf{t} = \partial_s \mathbf{r}$, $\mathbf{n} = (\mathbf{v} - (\mathbf{v} \cdot \mathbf{t})\mathbf{t})/\|\mathbf{v} - (\mathbf{v} \cdot \mathbf{t})\mathbf{t}\|_2$, cf. Fig 3. Then,

$$\mathbf{f}(\mathbf{v}, \mathbf{t}) = \mathbf{f_n}(\mathbf{v}, \mathbf{t}) + \mathbf{f_t}(\mathbf{v}, \mathbf{t}), \tag{16}$$

where

$$\mathbf{f_n} = 0.5\, \rho^{air}\, d\, \mathbf{v}^2 \left( \sin^2 \alpha + 4 \sqrt{\frac{\sin^3 \alpha}{\mathrm{Re}}} \right) \mathbf{n}, \tag{17}$$

$$\mathbf{f_t} = 0.5\, \rho^{air}\, d\, \mathbf{v}^2 \left( 5.4 \cos \alpha \sqrt{\frac{\sin \alpha}{\mathrm{Re}}} \right) \mathbf{t}, \tag{18}$$

with $\sin \alpha = (\mathbf{v} \cdot \mathbf{n})/\|\mathbf{v}\|_2$, $\cos \alpha = (\mathbf{v} \cdot \mathbf{t})/\|\mathbf{v}\|_2$ and $\mathrm{Re} = dv/\nu$ respectively. Equations (17), (18) suggest that a straight fiber with smooth surface does not feel any drag when it is aligned parallel to the direction of the incoming flow. This does not correspond to the experiments [18] revealing that for small $\alpha$, $\alpha \to 0$, $\mathbf{f_t}$ can be approximated by $\mathbf{f_t}(\alpha^\circ = \pi/36)$. For a rough surface in contrast, this situation of zero drag does not appear because the Taylor expression reads

$$\mathbf{f} = 0.5\, \rho^{air}\, d\, \mathbf{v}^2 \left[ \left( \sin^2 \alpha + \frac{4 \sin \alpha}{\sqrt{\mathrm{Re}}} \right) \mathbf{n} + \cos \alpha\, \mathbf{t} \right] \tag{19}$$

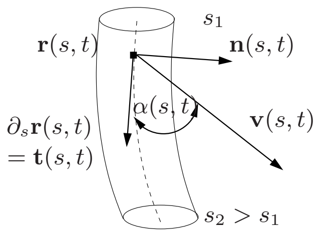


Figure 3: *Drag relevant angle $\alpha \in [0, \pi]$ enclosed by relative velocity $\mathbf{v}$ and fiber tangent $\partial_s \mathbf{r}$*

For technical reasons, we rewrite Eqs (17)-(19) as

$$\mathbf{f_n} = 0.5\, \rho^{air}\, d\, c_\mathrm{n}\, \|\mathbf{v_n}\|_2\, \mathbf{v_n}, \qquad \mathbf{f_t} = 0.5\, \rho^{air}\, d\, c_\mathrm{t}\, \|\mathbf{v_t}\|_2\, \mathbf{v_t}. \tag{20}$$

with the empirical drag coefficients for smooth resp. rough fibers

$$\begin{aligned} c_\mathrm{n}^{smooth} &= 1 + 4\sqrt{\nu/(d\|\mathbf{v_n}\|_2)}, & c_\mathrm{t}^{smooth} &= 5.4\sqrt{\nu\|\mathbf{v_n}\|_2/(d\|\mathbf{v_t}\|_2^2)}, \\ c_\mathrm{n}^{rough} &= 1 + 4\sqrt{\nu\|\mathbf{v}\|_2/(d\|\mathbf{v_n}\|_2^2)}, & c_\mathrm{t}^{rough} &= \|\mathbf{v}\|_2/\|\mathbf{v_t}\|_2. \end{aligned} \tag{21}$$

The high Reynolds number flow and the presence of very small vortices indicated by the relation $\eta < d$ in our application conflicts with the use of the heuristic linear Stokes drag. Hence, we determine the aerodynamic forces on the smooth polymer fiber under consideration by means of the empirically motivated nearly quadratic Taylor drag (20), (21), although this concept is only examined for high Re, but still laminar inflow regime. Additionally, to exclude the zero drag in case of parallelism of $\mathbf{t}$ and $\mathbf{v}$, we suggest a slight modification of the drag coefficient $c_\mathrm{t}^{smooth}$ that provides a better consistence to reality. As a smooth fiber lying parallel to the direction of the relative velocity experiences the same tangential drag force as one being rotated by $\alpha^\circ$ and as $\mathbf{v_n} = \mathbf{v} - (\mathbf{v} \cdot \mathbf{t})\mathbf{t}$, we define

$$\mathbf{v_n^\circ} := \begin{cases} \mathbf{v_n}, & c^\circ \geq \|\mathbf{v_t}\|_2/\|\mathbf{v}\|_2 \\ \mathbf{v} - \mathrm{sgn}(\mathbf{v} \cdot \mathbf{t}) c^\circ \|\mathbf{v}\|_2\, \mathbf{t}, & \text{else} \end{cases} \tag{22}$$

with $c^\circ = \cos \alpha^\circ$. Here, the sign function, $\mathrm{sgn}(x) = 1$ if $x \geq 0$, $\mathrm{sgn}(x) = -1$ else, includes equal and opposite directed vectors $\mathbf{t}$ and $\mathbf{v}$. We have $\|\mathbf{v_n^\circ}\|_2 = 0$, if and only if $\|\mathbf{v}\|_2 = 0$. Setting

$$c_\mathrm{t}^{smooth} = 5.4\sqrt{\nu\|\mathbf{v_n^\circ}\|_2/(d\|\mathbf{v_t}\|_2^2)} \tag{23}$$

yields thus a reasonable tangential drag model that is not only continuous but proves to be also differentiable.

## 3.2 Linear Drag Operator

Proceeding with the derivation of the linear drag operator $\mathbf{L^f}$, we consider a generalized linearization approach for the modified Taylor drag model $\mathbf{f}$

$$\mathbf{f}(\bar{\mathbf{v}} + \mathbf{u}', \mathbf{t}) \approx \mathbf{f}(\bar{\mathbf{v}}, \mathbf{t}) + \mathbf{L^f}(\bar{\mathbf{v}}, \mathbf{t}, k)\ \mathbf{u}', \tag{24}$$

with mean relative velocity between fluid and fiber $\bar{\mathbf{v}}$ and random Gaussian fluctuation of the flow velocity $\mathbf{u}'$. In the context of Eqs (3), (4), the first term represents the deterministic part of the aerodynamic forces and the second term the stochastic one.

**Model for Linear Drag Operator**
*Let $\mathbf{f} : \mathbb{R}^3 \times \mathbb{R}^2 \to \mathbb{R}^3$ be the modified Taylor drag model of Eqs (20)-(23). Then construct the linear drag operator $\mathbf{L^f}$ as continuous composition*

$$\mathbf{L^f}(\bar{\mathbf{v}}, \mathbf{t}, k) = \begin{cases} \nabla_{\mathbf{v}} \mathbf{f}(\bar{\mathbf{v}}, \mathbf{t}), & \varpi > 1 \\ \Big((1-\varpi)\big(a_{\mathrm{n}_0}(k)\ (\mathbf{I} - \mathbf{P_t}) +\ a_{\mathrm{t}_0}(k)\ \mathbf{P_t}\big) \\ +\varpi\ \nabla_{\mathbf{v}} \mathbf{f}(\varpi^{-1}\,\bar{\mathbf{v}}, \mathbf{t}), & \varpi \leq 1 \end{cases} \tag{25}$$

*with $\varpi = \|\bar{\mathbf{v}}\|_2\,(2k)^{-1/2}$. The parameters are given by*

$$a_{\mathrm{n}_0}(k) = \big(2a_{\mathrm{n}_1}^2 k + 5\sqrt{2^5}/\sqrt{3^{3/2}\pi}\,\mathrm{gam}(5/4) a_{\mathrm{n}_1} a_{\mathrm{n}_2} k^{3/4} + 16/\sqrt{3\pi}\, a_{\mathrm{n}_2}^2 k^{1/2}\big)^{1/2} \tag{26}$$

$$a_{\mathrm{t}_0}(k) = \sqrt{8/(3\pi)^{1/2}}\, a_{\mathrm{t}} k^{1/4} \tag{27}$$

*with $a_{\mathrm{n}_1} = 0.5\rho^{air} d$, $a_{\mathrm{n}_2} = \rho^{air}\sqrt{d\nu}$, $a_{\mathrm{t}} = 1.35 a_{\mathrm{n}_2}$, $c^\circ = \cos\alpha^\circ$ and gamma function* gam.

Let the projectors on fiber tangent $\mathbf{t} = \partial_s \mathbf{r}$, normal $\mathbf{n} = (\bar{\mathbf{v}} - (\bar{\mathbf{v}}\cdot\mathbf{t})\mathbf{t})/\|\bar{\mathbf{v}} - (\bar{\mathbf{v}}\cdot\mathbf{t})\mathbf{t}\|_2$ and binormal $\mathbf{b} = \mathbf{t}\times\mathbf{n}$ be described by $\mathbf{P}_{[\mathbf{x},\mathbf{y}]} = \mathbf{x}\otimes\mathbf{y}$. In particular, we abbreviate $\mathbf{P_x} := \mathbf{P}_{[\mathbf{x},\mathbf{x}]}$ and $\mathbf{P}_{\mathbf{x},\mathbf{y}} := \mathbf{P_x} + \mathbf{P_y}$, $\mathbf{x},\mathbf{y} \in \mathbb{R}^3$. Then, the operator $\nabla_{\mathbf{v}}\mathbf{f}$ resulting from Eqs (20)-(23) reads

$$\begin{aligned} \nabla_{\mathbf{v}}\mathbf{f}(\bar{\mathbf{v}}, \mathbf{t}) &= (a_{\mathrm{n}_1}\|\bar{\mathbf{v}}_\mathbf{n}\|_2 + 2a_{\mathrm{n}_2}\|\bar{\mathbf{v}}_\mathbf{n}\|_2^{1/2})\ \mathbf{P}_{\mathbf{n},\mathbf{b}} +\ (a_{\mathrm{n}_1}\|\bar{\mathbf{v}}_\mathbf{n}\|_2 + a_{\mathrm{n}_2}\|\bar{\mathbf{v}}_\mathbf{n}\|_2^{1/2})\ \mathbf{P_n} \\ &+ 2a_{\mathrm{t}}\|\bar{\mathbf{v}}_\mathbf{n}^\circ\|_2^{1/2}\ \mathbf{P_t} +\ a_{\mathrm{t}}\|\bar{\mathbf{v}}_\mathbf{n}^\circ\|_2^{-1/2}(\bar{\mathbf{v}}\cdot\mathbf{t})\,\mathbf{P}_{[\mathbf{t},\,\bar{\mathbf{v}}_\mathbf{n}^\circ\|\bar{\mathbf{v}}_\mathbf{n}^\circ\|^{-1}]} \\ &+ \chi(\bar{\mathbf{v}}, \mathbf{t})\, a_{\mathrm{t}}\|\bar{\mathbf{v}}_\mathbf{n}^\circ\|_2^{-3/2}\, c^\circ(c^\circ - \|\bar{\mathbf{v}}_\mathbf{t}\|_2\|\bar{\mathbf{v}}\|_2^{-1})(\|\bar{\mathbf{v}}_\mathbf{t}\|_2^2\ \mathbf{P_t} + (\bar{\mathbf{v}}\cdot\mathbf{t})\|\bar{\mathbf{v}}_\mathbf{n}\|_2\ \mathbf{P}_{[\mathbf{t},\mathbf{n}]}) \end{aligned}$$

Though the use of the indicator function $\chi(\bar{\mathbf{v}}, \mathbf{t}) = 1$ for $(\|\bar{\mathbf{v}}_\mathbf{t}\|_2\|\bar{\mathbf{v}}\|_2^{-1}) \geq c^\circ$ and $\chi(\bar{\mathbf{v}}, \mathbf{t}) = 0$ else, the introduction of $\mathbf{v}_\mathbf{n}^\circ$ in Eq (22) yields a continuous Gateaux derivative. In the limit to $\mathbf{t}\|\bar{\mathbf{v}}$, it stays additionally bounded which is a big difference to an ansatz based on Taylor's original zero drag model with missing tangential component.

The Gateaux derivative $\nabla_{\mathbf{v}}\mathbf{f}(\bar{\mathbf{v}}, \mathbf{t})\,\mathbf{u}'$ is a good representative for the stochastic part in Eq (24) if the mean relative velocity is much higher than the fluctuations that are characterized by the turbulent kinetic energy $k$, i.e. $\|\bar{\mathbf{v}}\|_2^2 \gg \mathbb{E}[\mathbf{u}'^2] = 2k$. In case of $\bar{\mathbf{v}} = \mathbf{0}$ in contrast, it would provide a zero drag, since

$$\mathbf{f}(\bar{\mathbf{v}} + \mathbf{u}', \mathbf{t})|_{\bar{\mathbf{v}}=\mathbf{0}} = \mathbf{f}(\mathbf{0}, \mathbf{t}) + \nabla_{\mathbf{v}}\mathbf{f}(\mathbf{0}, \mathbf{t})\,\mathbf{u}' + \mathcal{O}((\mathbf{u}')^2) = \mathbf{0} + \mathcal{O}((\mathbf{u}')^2),$$

which is absurd as the velocity fluctuations affect the fiber though vanishing mean relative velocity

$$\mathbf{f}(\mathbf{u}', \mathbf{t}) = (a_{\mathrm{n}_1}\|\mathbf{u}_\mathbf{n}'\|_2 + 2a_{\mathrm{n}_2}\|\mathbf{u}_\mathbf{n}'\|_2^{1/2})\ \mathbf{u}_\mathbf{n}' + 2a_{\mathrm{t}}\|\mathbf{u}_\mathbf{n}'^{\,\circ}\|_2^{1/2}\ \mathbf{u}_\mathbf{t}'. \tag{28}$$

Note that in Eq (28) the direction $\mathbf{n}$ is exceptionally determined by $\mathbf{u}'$, i.e. $\mathbf{u}_\mathbf{n}' = \mathbf{u}' - \mathbf{u}_\mathbf{t}'$. The fact that the expectations of drag and velocity fluctuations are equal, i.e. $\mathbb{E}[\mathbf{f}(\mathbf{u}', \mathbf{t})] = \mathbb{E}[\mathbf{u}'] = \mathbf{0}$, motivates the stated extension of the linearized approach for $\bar{\mathbf{v}} = \mathbf{0}$. Keeping the directional vectors $\mathbf{u}_\mathbf{n}'$, $\mathbf{u}_\mathbf{t}'$, the coefficients with the specific norms are replaced by the respective averaged quantity expressed by the kinetic energy $k$ such that the variance is correctly reproduced. Abbreviate therefor $\mathbf{f} := \mathbf{f}(\mathbf{u}', \mathbf{t})$ and consider

$$\begin{aligned} \mathbb{E}[\mathbf{f}\otimes\mathbf{f}] = \mathbb{E}[(\mathbf{f}\cdot\mathbf{t})^2]\,\mathbf{t}\otimes\mathbf{t} &+ \mathbb{E}[(\mathbf{f}\cdot\mathbf{n_1})^2]\,\mathbf{n_1}\otimes\mathbf{n_1} + \mathbb{E}[(\mathbf{f}\cdot\mathbf{n_2})^2]\,\mathbf{n_2}\otimes\mathbf{n_2} \\ &+ \mathbb{E}[(\mathbf{f}\cdot\mathbf{t})\ \ (\mathbf{f}\cdot\mathbf{n_1})]\ \ (\mathbf{t}\otimes\mathbf{n_1} + \mathbf{n_1}\otimes\mathbf{t}) \\ &+ \mathbb{E}[(\mathbf{f}\cdot\mathbf{t})\ \ (\mathbf{f}\cdot\mathbf{n_2})]\ \ (\mathbf{t}\otimes\mathbf{n_2} + \mathbf{n_2}\otimes\mathbf{t}) \\ &+ \mathbb{E}[(\mathbf{f}\cdot\mathbf{n_1})\,(\mathbf{f}\cdot\mathbf{n_2})]\ \ (\mathbf{n_1}\otimes\mathbf{n_2} + \mathbf{n_2}\otimes\mathbf{n_1}) \end{aligned}$$

with arbitrarily chosen orthogonal normal vectors $\mathbf{n_1}$, $\mathbf{n_2}$. The mixed expectations vanish thereby due to the independence and odd appearance of the underlying velocity components, as for $\mathbb{E}[\mathbf{f}]$ above. Because of the identical distribution of the drag in the normal plane, we have $\mathbb{E}[(\mathbf{f}\cdot\mathbf{n_1})^2] = \mathbb{E}[(\mathbf{f}\cdot\mathbf{n_2})^2]$ such that it is sufficient to consider $\mathbb{E}[(\mathbf{f}\cdot\mathbf{n})^2]$. Using $\mathbb{E}[\mathbf{u'}^2] = 2k$ and the identical distribution of the velocity components yields their variance $\mathbb{E}[(\mathbf{u'}\cdot\mathbf{e})^2] = \sigma^2 = 2k/3$ with unit vector $\mathbf{e}$. The general (centered) moments are prescribed by the gamma function according to $\mathbb{E}[|\mathbf{u'}\cdot\mathbf{e}|^{2m}] = (2\pi\sigma^2)^{-1/2}\int x^{2m}e^{-x^2/(2\sigma^2)}\,dx = (2\sigma^2)^m\,\mathrm{gam}(m+1/2)/\sqrt{\pi}$, $m\in\mathbb{R}^+$. Then,

$$\mathbb{E}[(\mathbf{f}\cdot\mathbf{t})^2] = 4a_{\mathrm{t}}^2\,\mathbb{E}[|\mathbf{u'}\cdot\mathbf{n}^\circ|]\,\mathbb{E}[(\mathbf{u'}\cdot\mathbf{t})^2] = (a_{\mathrm{t}_0}(k)\,\sigma)^2$$

$$\mathbb{E}[(\mathbf{f}\cdot\mathbf{n})^2] = a_{\mathrm{n}_1}^2\mathbb{E}[(\mathbf{u'}\cdot\mathbf{n})^4] + 4a_{\mathrm{n}_1}a_{\mathrm{n}_2}\mathbb{E}[|\mathbf{u'}\cdot\mathbf{n}|^{7/2}] + 4a_{\mathrm{n}_2}^2\mathbb{E}[|\mathbf{u'}\cdot\mathbf{n}|^3] = (a_{\mathrm{n}_0}(k)\,\sigma)^2,$$

by means of Eqs (26), (27), such that

$$\mathbf{f}_0(\mathbf{u'},\mathbf{t},k) := a_{\mathrm{n}_0}(k)\,\mathbf{u'_n} + a_{\mathrm{t}_0}(k)\,\mathbf{u'_t} = a_{\mathrm{n}_0}(k)\,(\mathbf{u'}-\mathbf{u'_t}) + a_{\mathrm{t}_0}(k)\,\mathbf{u'_t}$$

describes a Gaussian random variable that has the same stochastic parameters, i.e. expectation and variance, as the original drag of Eq (28). Moreover, it is linear in $\mathbf{u'}$, though the suggestion of its coefficients depending on $k$. The turbulent kinetic energy has to be viewed as input parameter for the generation of the flow fluctuations in the context of this work. Hence, $\mathbf{L^f}(\bar{\mathbf{v}},\mathbf{t},k) = a_{\mathrm{n}_0}(k)\,(\mathbf{I}-\mathbf{P_t}) + a_{\mathrm{t}_0}(k)\,\mathbf{P_t}$ is taken as drag operator in the case $\bar{\mathbf{v}} = \mathbf{0}$.

For the secant complement that combines the two determined drag operators, all functional dependencies of $\varpi$ might be imaginable, e.g. squared, linear or quadratic in $\|\bar{\mathbf{v}}\|_2$. But because of the lack of information about this intermediate domain, i.e. $\|\bar{\mathbf{v}}\|_2^2\in(0,2k)$, they are mathematically and physically as less motivated as our proposed linear ansatz in Eq (25).

## 3.3 Technical Modification of Force Amplitude

Since the defined drag operator $\mathbf{L^f}$ has a finite, non-vanishing limit for $\bar{v}_{\mathrm{n}}\to 0$, it is unable to balance the arising singularity of the force amplitude in Eq (7)

$$\mathbf{D} = \left(\frac{2\pi}{\bar{v}_{\mathrm{n}}}\int_0^\infty \frac{E(\kappa)}{\kappa^2}d\kappa\right)^{1/2}\mathbf{P_{t,n}} \overset{(11)}{\approx} \left(\frac{2\pi F_2}{\bar{v}_{\mathrm{n}}}\right)^{1/2}\frac{k^2}{\epsilon}\,\mathbf{P_{t,n}}.$$

Consequently, the uncorrelated aerodynamic force $\mathbf{f}_{uc}^{air}$ diverges in case of linear dependence of $\mathbf{t}$ and $\bar{\mathbf{v}}$, whereas the correlated one $\mathbf{f}_{cc}^{air}$ stays bounded, as we have already seen in the similarity estimates (13), (14). Although the occurrence of this single discrepancy is negligibly small, the further numerical realization requires its handling. Thus, we suggest a slight technical modification of the amplitude that has no influence on the proved approximation quality of the uncorrelated force. Replace $\mathbf{D}$ by

$$\check{\mathbf{D}} = (2\pi F_2)^{1/2}\,\frac{k^2}{\epsilon}\begin{cases}\bar{v}_{\mathrm{n}}^{-1/2}\,\mathbf{P_{t,n}}, & \omega > 1\\ (1-\omega)\,(\bar{v}_{\mathrm{n}}^{crit})^{-1/2}\,(\mathbf{P_t}+(\mathbf{I}-\mathbf{P_t})/2) + \omega\,\bar{v}_{\mathrm{n}}^{-1/2}\,\mathbf{P_{t,n}}, & \omega\le 1\end{cases} \qquad (29)$$

with $\omega = \bar{v}_{\mathrm{n}}/\bar{v}_{\mathrm{n}}^{crit}$, then

$$\lim_{\bar{v}_{\mathrm{n}}\to 0}\mathbf{f}_{uc}^{air} = \mathbf{f} + \left(\frac{2\pi F_2}{\bar{v}_{\mathrm{n}}^{crit}}\right)^{1/2}\frac{k^2}{\epsilon}\begin{cases} l^{||}\,\mathbf{P_t}\,\mathbf{p}, & \varpi > 1\\ ((1-\varpi)\,(a_{\mathrm{n}_0}(k)/2\;(\mathbf{I}-\mathbf{P_t}) + a_{\mathrm{t}_0}(k)\;\mathbf{P_t}) \\ \quad +\varpi\, l^{||}\,\mathbf{P_t})\;\mathbf{p}, & \varpi\le 1\end{cases}$$

coincides with the limit of the correlated force regarding the formal structure of the terms. Here, the deterministic force part given by the modified Taylor drag, Eqs (20), (23), reads $\mathbf{f} = \mathbf{f_t}$ for $\|\bar{\mathbf{v}}\|_2 \neq 0$ and $\mathbf{f} = \mathbf{0}$ else, and furthermore

$$l^{||} := a_{\mathrm{t}}\left(2\bar{v}_{\mathrm{n}}^{\circ\,1/2} + \frac{\bar{v}_{\mathrm{t}}}{\bar{v}_{\mathrm{n}}^{\circ\,1/2}} + \frac{(c^{\circ\,2}-c^\circ)\bar{v}_{\mathrm{t}}^2}{\bar{v}_{\mathrm{n}}^{\circ\,3/2}}\right)$$

with $\bar{v}_{\mathrm{n}}^\circ = (1-\mathrm{sgn}(\bar{\mathbf{v}}\cdot\mathbf{t})c^\circ)\|\bar{\mathbf{v}}\|_2 < \infty$. The modification in Eq (29) can be interpreted as cutting the amplitude $\mathbf{D}$ at the critical velocity $\bar{v}_{\mathrm{n}} = \bar{v}_{\mathrm{n}}^{crit}$ and matching it continuously with a linear extension. As the underlying $(\mathbf{t},\bar{\mathbf{v}})$-induced set $\{\mathbf{t},\mathbf{n},\mathbf{b}\}$ looses its basis properties in the limit $\bar{v}_{\mathrm{n}} = 0$, we distinguish between the tangential and the remaining projectors and introduce the normal independent splitting $(\mathbf{P_t} + (\mathbf{I} - \mathbf{P_t})/2)$ instead of the original $(\mathbf{P_t} + \mathbf{P_n})$. Thus, the direction of $\mathbf{f}_{uc}^{air}$ is not longer specified by the mean relative velocity for $\varpi \to 0$ as already indicated by $\mathbf{f}_{cc}^{air}$.

The needed technical modification of the amplitude reveals the deficiency of the modeled fluctuation velocity fields $\mathbf{w}_f^{\sigma,\tau}$ whose dynamics is based on locally frozen turbulence pattern. Hence, the fiber experiences no temporal change of the correlations, if it moves within the mean streamlines, i.e. $\bar{v}_{\rm n} = 0$. Alternatively to the modification, one might question the underlying concept of frozen turbulence that neglects the natural decay of vortices because of its large time $t_{\rm T}$ and slow turbulent velocity scale $u_{\rm T} = k^{1/2}$ in comparison to the advection scales of the mean flow $t_{\rm A}$, $\bar{u}$. However, for a fiber suspended in turbulence, the actual temporal change of the experienced turbulent coherences is prescribed by the velocity $v_{\rm T}^f = \max\{\bar{v}_{\rm n}, u_{\rm T}\}$. This could be incorporated in the definition of the flow-dependent force amplitude $\breve{\mathbf{D}}$ by substituting $\bar{v}_{\rm n}^{crit}$ by $u_{\rm T}$. Then the characteristic turbulent fiber time reads $\tau_{\rm T}^f = \min\{l_{\rm T}/\bar{v}_{\rm n}, t_{\rm T}\}$. The consequences of the choice of the parameter $\bar{v}_{\rm n}^{crit}$ are illustrated in the numerical results of the next section.

# 4 Numerical Simulations

The input flow data for the following numerical simulations of the fiber dynamics stem from $k$-$\epsilon$ computations of FLUENT 6.1 that has been adapted with user-specific procedures to reflect the realistic turbulent flow behavior of a melt-spinning process. The implementation of the fiber system (1), (2) is based on a standard method of lines. The use of spatial finite differences of higher order yields thereby the appropriate approximation of the algebraic constraint (2). The time integration is realized by a semi-implicit Euler method where an adaptive time step control ensures stability and accuracy. The arising nonlinear system of equations is iteratively solved by a modified Newton-Raphson method. As the Jacobian matrices show a band structure, the computational effect of an iteration step is proportional to the number of fiber points. Note that the aerodynamic forces are explicitly included. Their quality depends crucially on the available flow data that is linearly interpolated on the spatial and temporal fiber grid.

In the following, we briefly present the numerical algorithms for the realization of the correlated and uncorrelated aerodynamic forces, before we then compare their effects on the fiber dynamics by means of an introduced curvature measure.

## 4.1 Algorithms

Let $I_m^n = \{l \in \mathbb{N}_0 \,|\, m \leq l \leq n\}$. Let the spatial and temporal fiber discretization be given by $s_i = i\Delta s$ and $t_j = t_{j-1} + \Delta t_{j-1}$, $t_0 = 0$ with fixed space increment $\Delta s$ and adaptive time step $\Delta t_j$, $(i,j) \in I_0^n \times I_0^m$. Then denote the respective function values at the fiber point $s_i$ at time $t_j$ with subscript $_i$ and superscript $^j$, e.g. $\mathbf{r}_i^j = \mathbf{r}(s_i, t_j)$.

The numerical generation of the correlated aerodynamic force $\mathbf{f}_{cc}^{air}$ utilizes ARMA processes [2] for the centered, homogeneous independent local fluctuation velocity fields $\mathbf{w}_f^{\sigma,\tau}$ along the fiber, whereas the implementation of the uncorrelated force $\mathbf{f}_{uc}^{air}$ is exclusively based on Gaussian white noise $\mathbf{p}$,

$$\lim_{(\Delta s, \Delta t_j) \to \mathbf{0}} (\Delta s \Delta t_j)^{1/2}\, \mathbf{p}_i^j \sim \mathcal{N}(\mathbf{0}, \mathbf{I}).$$

**Algorithm 1 (Computation of Correlated Force)**
*Choose $l_{\rm T}$ and $t_{\rm T}$ as characteristic turbulent large scales of the problem. Consider a fixed fiber and time point that is indicated by the index tuple $(i,j) \in I_0^n \times I_0^m$.*

1. *Determine its corresponding index set $N_i^j$*

$$N_i^j = \{(\phi,\tau) \,|\, \|\mathbf{r}_i^j - \mathbf{r}_\phi^\tau - \bar{\mathbf{u}}_i^j \sum_{q=1}^{j-\tau} \Delta t_{j+1-q}\|_2 \leq l_{\rm T} \wedge \sum_{q=1}^{j-\tau} \Delta t_{j+1-q} \leq t_{\rm T}\}$$

   *with feasible tuples $(\phi,\tau) \in (I_0^n \times I_0^{j-1}) \cup (I_0^i \times I_j^j)$.*

2. *Compute the centered homogeneous local fluctuations $(\mathbf{w}_f^{\boldsymbol{\ell}})_i^j$ for all $\boldsymbol{\ell} = (\ell_1, \ell_2) \in N_i^j$. For this purpose, consider a fixed $\boldsymbol{\ell}$:*

   (a) *Set the turbulent fine scale length $\lambda_{\rm T}^{\boldsymbol{\ell}} = (20 k^{\boldsymbol{\ell}} \nu / \epsilon^{\boldsymbol{\ell}})^{1/2}$.*

(b) *Determine the correlation index set* $(J^{\boldsymbol{\ell}})_i^j$

$$(J^{\boldsymbol{\ell}})_i^j = \{(\phi,\tau) \,|\, \|\mathbf{r}_i^j - \mathbf{r}_\phi^\tau - \bar{\mathbf{u}}^{\boldsymbol{\ell}} \sum_{q=1}^{j-\tau} \Delta t_{j+1-q}\|_2 \leq \lambda_{\mathrm{T}}^{\boldsymbol{\ell}}\}$$

*with feasible tuples*

$$(\phi,\tau) \in \begin{cases} I_{\ell_1}^{i-1} \times I_{\ell_2}^{\ell_2}, & \ell_2 = j,\ \ell_1 < i \\ (I_{\ell_1}^{n} \times I_{\ell_2}^{\ell_2}) \cup (I_0^{i-1} \times I_j^j), & \ell_2 = j-1 \\ (I_{\ell_1}^{n} \times I_{\ell_2}^{\ell_2}) \cup (I_0^{n} \times I_{\ell_2+1}^{j-1}) \cup (I_0^{i-1} \times I_j^j), & \ell_2 < j-1 \\ \emptyset, & \textit{otherwise.} \end{cases}$$

(c) *If* $(J^{\boldsymbol{\ell}})_i^j \neq \emptyset$,
*then:*

i. *Define a bijective mapping* $\rho : \{1,...,|(J^{\boldsymbol{\ell}})_i^j|\} \to (J^{\boldsymbol{\ell}})_i^j$ *and set* $\rho(0) = (i,j)$.

ii. *Consider the vectorial ARMA process*

$$(\mathbf{w}_f^{\boldsymbol{\ell}})_i^j = (\mathbf{w}_f^{\boldsymbol{\ell}})_{\rho(0)} = \sum_{q=1}^{|(J^{\boldsymbol{\ell}})_i^j|} \mathbf{A}_q (\mathbf{w}_f^{\boldsymbol{\ell}})_{\rho(q)} + (\boldsymbol{\xi}^{\boldsymbol{\ell}})_i^j \tag{30}$$

*with unknown coefficients* $\mathbf{A}_q \in \mathbb{R}^{3\times 3}$ *and noise* $(\boldsymbol{\xi}^{\boldsymbol{\ell}})_i^j \sim \mathcal{N}(\mathbf{0},\mathbf{K})$ *that is assumed to be independent of* $(\mathbf{w}_f^{\boldsymbol{\ell}})_{\rho(q)}$.

iii. *Define* $\mathbf{C}_{(p,q)} := \mathbb{E}[(\mathbf{w}_f^{\boldsymbol{\ell}})_{\rho(p)} \otimes (\mathbf{w}_f^{\boldsymbol{\ell}})_{\rho(q)}]$ *for* $p,q = 0,...,|(J^{\boldsymbol{\ell}})_i^j|$, *by means of the correlation tensor* $\boldsymbol{\gamma}_0^{\boldsymbol{\ell}}$ *in the canonical basis representation. Then particularly,* $\mathbf{C}_{(p,p)} = \boldsymbol{\gamma}_0^{\boldsymbol{\ell}}(\mathbf{0})$ *and* $\mathbf{C}_{(p,q)} = \mathbf{C}_{(q,p)}$ *hold.*

iv. *Approximate the lateral correlation function of* $\boldsymbol{\gamma}_0^{\boldsymbol{\ell}}$ *by* $c_1^{\boldsymbol{\ell}}(z) = 2k^{\boldsymbol{\ell}}/3 - \epsilon^{\boldsymbol{\ell}} z^2/(30\nu)$, *i.e.* $\boldsymbol{\gamma}_0^{\boldsymbol{\ell}}(\mathbf{z}) = (c_1(z) + z\partial_z c_1(z)/2)\mathbf{I} - \partial_z c_1(z)/(2z)\mathbf{z}\otimes\mathbf{z}$, $z = \|\mathbf{z}\|_2$ *[12].*

v. *Compute the coefficients* $\mathbf{A}_q$ *by solving*

$$\sum_{q=1}^{|(J^{\boldsymbol{\ell}})_i^j|} \mathbf{C}_{(p,q)}\ \mathbf{A}_q = \mathbf{C}_{(p,0)}, \qquad p = 0,...,|(J^{\boldsymbol{\ell}})_i^j| - 1. \tag{31}$$

vi. *Calculate the covariance* $\mathbf{K}$ *of the noise term* $(\boldsymbol{\xi}^{\boldsymbol{\ell}})_i^j$ *from*

$$\begin{aligned} \mathbf{K} = \mathbf{C}_{(0,0)} &- \sum_{p=1}^{|(J^{\boldsymbol{\ell}})_i^j|} \mathbf{A}_p \mathbf{C}_{(p,p)} \mathbf{A}_p^T \\ &- \sum_{p=1}^{|(J^{\boldsymbol{\ell}})_i^j|-1} \sum_{q=p+1}^{|(J^{\boldsymbol{\ell}})_i^j|} \mathbf{A}_p \mathbf{C}_{(p,q)} \mathbf{A}_q^T - \sum_{p=1}^{|(J^{\boldsymbol{\ell}})_i^j|-1} \sum_{q=p+1}^{|(J^{\boldsymbol{\ell}})_i^j|} \mathbf{A}_q \mathbf{C}_{(q,p)} \mathbf{A}_p^T. \end{aligned}$$

vii. *Generate the correlated noise term* $(\boldsymbol{\xi}^{\boldsymbol{\ell}})_i^j = (\xi_1,\xi_2,\xi_3)$ *according to its covariance* $\mathbf{K} = (K_{pq})_{p,q=1,2,3}$ *and the following ansatz*

$$\begin{aligned} &\xi_1 \sim \mathcal{N}(0, K_{11}) \\ &\xi_2 = \alpha\xi_1 + \xi_2' \\ &\xi_3 = \beta_1\xi_1 + \beta_2\xi_2 + \xi_3', \end{aligned} \tag{32}$$

*where the parameters* $\alpha, \beta_1, \beta_2$ *and the independent random numbers* $\xi_2'$, $\xi_3'$ *are prescribed by*
$\alpha = K_{22}/K_{12}$ *and* $\sum_{q=1}^2 K_{pq}\,\beta_q = K_{p3}$, *for* $p = 2,3$,
$\xi_2' \sim \mathcal{N}(0, K_{22} - \alpha^2 K_{11})$,
$\xi_3' \sim \mathcal{N}(0, K_{33} - \beta_1^2 K_{11} - \beta_2^2 K_{22} - 2\beta_1\beta_2 K_{12})$.

viii. *Plug the determined coefficients* $\mathbf{A}_q$ *of Eq (31) and the correlated noise* $(\boldsymbol{\xi}^{\boldsymbol{\ell}})_i^j$ *of Eq (32) into the ARMA process, Eq (30).*

*else,* $(J^{\boldsymbol{\ell}})_i^j = \emptyset$:
*Set*

$$(\mathbf{w}_f^{\boldsymbol{\ell}})_i^j = \left(\frac{2k^{\boldsymbol{\ell}}}{3}\right)^{1/2} (\boldsymbol{\xi}^{\boldsymbol{\ell}})_i^j, \qquad \textit{with } (\boldsymbol{\xi}^{\boldsymbol{\ell}})_i^j \sim \mathcal{N}(\mathbf{0},\mathbf{I}). \tag{33}$$

3. *Determine the correlated aerodynamic force*

$$(\mathbf{f}_{cc}^{air})_i^j = \mathbf{f}(\bar{\mathbf{v}}_i^j, \mathbf{t}_i^j) + \mathbf{L}^{air}(\bar{\mathbf{v}}_i^j, \mathbf{t}_i^j, k_i^j)\ |N_i^j|^{-1/2} \sum_{\boldsymbol{\ell}\in N_i^j} (\mathbf{w}_f^{\boldsymbol{\ell}})_i^j. \tag{34}$$

**Algorithm 2 (Computation of Uncorrelated Force)**
*Consider a fixed fiber and time point that is indicated by the index tuple $(i,j) \in I_0^n \times I_0^m$. Set $\varpi_i^j = \|\bar{\mathbf{v}}_i^j\|_2/(2k_i^j)^{1/2}$, $\omega_i^j = (\bar{v}_\mathrm{n})_i^j/\bar{v}_\mathrm{n}^{crit}$ and let the projectors $\mathbf{P}$ depend on space and time discretization. Then, the uncorrelated aerodynamic force is determined by*

$$(\mathbf{f}_{uc}^{air})_i^j = \mathbf{f}(\bar{\mathbf{v}}_i^j, \mathbf{t}_i^j) + \sqrt{\frac{2\pi F_2}{\Delta s \Delta t_j}}\ \frac{(k_i^j)^2}{\epsilon_i^j\ \sqrt{(\bar{v}_\mathrm{n})_i^j}}\ \boldsymbol{\phi}_i^j \tag{35}$$

*where*

$$\boldsymbol{\phi}_i^j = \begin{cases} \nabla_\mathbf{v}\mathbf{f}(\bar{\mathbf{v}}_i^j, \mathbf{t}_i^j)\ \mathbf{P}_{(\mathbf{t},\mathbf{n})_i^j}\ \boldsymbol{\xi}_i^j, & \varpi_i^j > 1, \omega_i^j > 1 \\[1em] \nabla_\mathbf{v}\mathbf{f}(\bar{\mathbf{v}}_i^j, \mathbf{t}_i^j)\ \left[(1-\omega_i^j)\sqrt{\omega_i^j}\ \left(\mathbf{P}_{\mathbf{t}_i^j} + (\mathbf{I}-\mathbf{P}_{\mathbf{t}_i^j})/2\right) + \omega_i^j\ \mathbf{P}_{(\mathbf{t},\mathbf{n})_i^j}\right]\ \boldsymbol{\xi}_i^j, & \\ & \varpi_i^j > 1, \omega_i^j \leq 1 \\[1em] \left[(1-\varpi_i^j)\left(a_{\mathrm{t}_0}(k_i^j)\ \mathbf{P}_{\mathbf{t}_i^j} + a_{\mathrm{n}_0}(k_i^j)\ \mathbf{P}_{\mathbf{n}_i^j}\right)\right. & \\ \quad \left. +\varpi_i^j\ \nabla_\mathbf{v}\mathbf{f}((\varpi_i^j)^{-1}\,\bar{\mathbf{v}}_i^j, \mathbf{t}_i^j)\ \mathbf{P}_{(\mathbf{t},\mathbf{n})_i^j}\right]\ \boldsymbol{\xi}_i^j, & \varpi_i^j \leq 1, \omega_i^j > 1 \\[1em] \left[\left[(1-\varpi_i^j)\, a_{\mathrm{t}_0}(k_i^j)\ \mathbf{I} + \varpi_i^j\ \nabla_\mathbf{v}\mathbf{f}((\varpi_i^j)^{-1}\,\bar{\mathbf{v}}_i^j, \mathbf{t}_i^j)\right](1-\omega_i^j)\sqrt{\omega_i^j}\ \mathbf{P}_{\mathbf{t}_i^j}\right. & \\ \quad +(1-\varpi_i^j)\, a_{\mathrm{t}_0}(k_i^j)\, \omega_i^j\ \mathbf{P}_{\mathbf{t}_i^j} & \\ \quad +\left[(1-\varpi_i^j)\, a_{\mathrm{n}_0}(k_i^j)\ \mathbf{I} + \varpi_i^j\ \nabla_\mathbf{v}\mathbf{f}((\varpi_i^j)^{-1}\,\bar{\mathbf{v}}_i^j, \mathbf{t}_i^j)\right] & \\ \quad\quad \left.\left[(1-\omega_i^j)\sqrt{\omega_i^j}\ (\mathbf{I}-\mathbf{P}_{\mathbf{t}_i^j})/2 + \omega_i^j\ \mathbf{P}_{(\mathbf{t},\mathbf{n})_i^j}\right]\right]\ \boldsymbol{\xi}_i^j, & \varpi_i^j \leq 1, \omega_i^j \leq 1 \end{cases}$$

*and $\boldsymbol{\xi}_i^j \sim \mathcal{N}(\mathbf{0},\mathbf{I})$, i.e. the components $(\xi_l)_i^j \sim \mathcal{N}(0,1)$, $l = 1,2,3$, are independent and normally distributed.*

Regarding memory and computational effort, Alg 1 is extremely costly. Apart from the two searching procedures in Step 1 and 2.b, it requires in general the solving of $|N|$ linear systems of $3|J|$ equations for each fiber and time point specified by $(i,j)$, Step 2.c.v. Thereby, the cardinal numbers $|N|$ and $|J|$ depend not only on the fiber dynamics at $(i,j)$, but also crucially on the spatial and temporal grid size which should be chosen to be a compromise between computational capacity and desirable accuracy of the correlation structures to be realized. The required $3|N|$ Gaussian deviates for Step 2.c.vii are here generated by the Box-Muller Method [5]. In comparison to Alg 1, Alg 2 is obviously enormously cheaper and faster. Its evaluation is independent of the chosen discretization and needs only 3 Gaussian deviates per fiber and time point.

In case of large-scale resolution, where $N_i^j = \{(i,j)\}$ and $(J^{\boldsymbol{\ell}})_i^j = \emptyset$ for all $(i,j)$ in Alg 1, the correlated aerodynamic force $\mathbf{f}_{cc}^{air}$ is obviously approximated numerically by the uncorrelated $\mathbf{f}_{uc}^{air}$, since Eqs (33), (34) correspond to the white noise approach of Alg 2 with $\Delta s \sim l_\mathrm{T}$ and $\Delta t \sim t_\mathrm{T}$ in Eq (35). But, also for fine-scale resolution, the respective numerical representatives match very well as far as their effects on the fiber dynamics are concerned. To show the statistical coincidence of their influence, we analyze the imposed fiber dynamics by means of a curvature measure in the following. Thereby, we restrict the comparison exemplarily on a fixed appropriate fiber discretization because of the extremely long run-time and the enormous memory demands of Alg 1.

## 4.2 Results

Simulating the motion of an inextensible slender fiber swinging freely in a turbulent flow field, we show the similarity of the macroscopic effects on the fiber that are caused by the correlated and uncorrelated force model. For this purpose, we introduce the following curvature measure.

**Definition 1 (Curvature Measure)**
*Let $\mathbf{r}_i^j$, $(i,j) \in \mathcal{I}_0^n \times \mathcal{I}_0^m$ be the spatially and temporally discretized fiber line that is imposed by the*

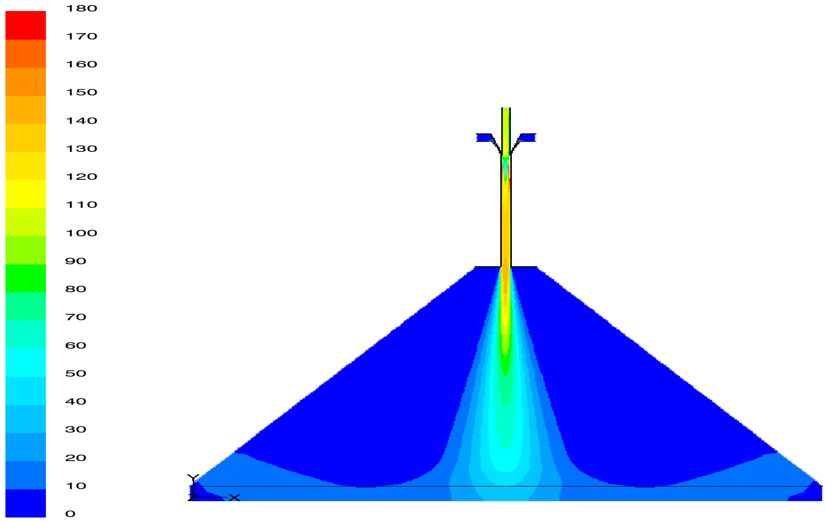


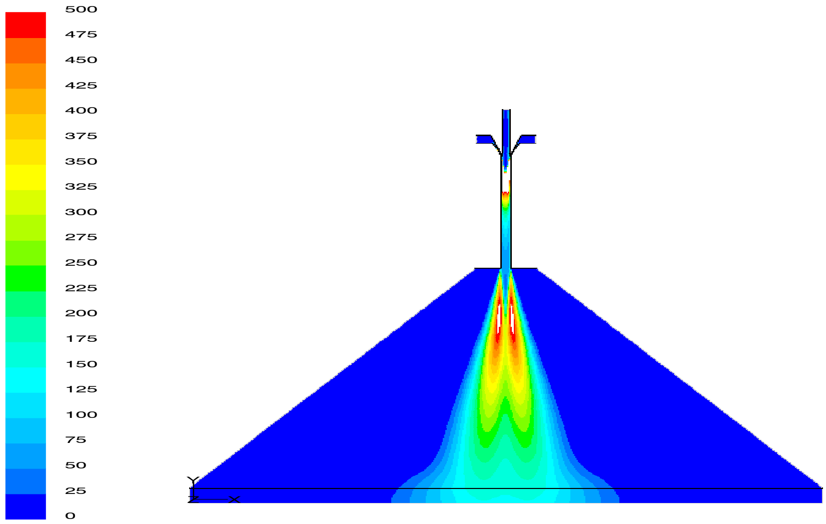


Figure 4: $k$-$\epsilon$ simulation results for turbulent flow. Top to bottom: Stationary 2D vertical mean stream $\|\bar{\mathbf{u}}\|_2$, kinetic energy $k$ in SI-units

*aerodynamic forces according to Eqs (1), (2). Then, its curvature measure at time $t_j$ is defined by*

$$\mathcal{K}^j = \frac{1}{n-1}\sum_{i=1}^{n-1} \|\Delta_{ss}\mathbf{r}_i^j\|_2$$

*using the central difference $\Delta_{ss}\mathbf{r}_i^j = (\mathbf{r}_{i+1}^j - 2\mathbf{r}_i^j + \mathbf{r}_{i-1}^j)/\Delta s^2$.*

Evaluating the fiber line over a certain time interval gives statistically comparable parameters for $\mathcal{K}$, i.e. its mean $\mu$ and its standard deviation $\sigma$.

Apart from the similarity, the curvature measure states the significance of the turbulent aerodynamic force for entanglement and loop forming of the fiber. To illustrate these effects, we consider a fiber that is initially hanging in the symmetry axis of a stationary, vertically directed two-dimensional mean flow field $\bar{\mathbf{u}}$ (cf. Fig 4). The turbulent fluctuations are prescribed by the stationary kinetic energy $k$ and dissipation rate $\epsilon$. Then, the resulting deterministic force part $\bar{\mathbf{f}}$ is mainly vertically directed and the stochastic part $\mathbf{f}'$ determine almost exclusively the small horizontal fiber oscillations. Hence, under neglect of the turbulent influence, the fiber is not excited out of its position of rest. It has the characteristic curvature properties $\mu = 0$ and $\sigma = 0$ which will prescribe our reference state. The used underlying flow data represent a realistic turbulent stream as it might be expected in the deposition region of a melt-spinning process. Note that the illustrated geometry in Fig 4 is distorted in width to stress the flow behavior around the symmetry axis, $\mathbf{e_3}$-axis.

Exposing the fiber to the stochastic force models, we obtain the representatives of a momentary fiber position that are visualized in Fig 6. Apart from the correlated force, we distinguish hereby between the uncorrelated force effects by choosing two variants for $\bar{v}_\mathrm{n}^{crit}$, i.e. $\bar{v}_\mathrm{n}^{crit} = 10^{-3}$ m/s and $\bar{v}_\mathrm{n}^{crit} = (2k)^{1/2}$. On the first glance, the behavior of the fibers seems to be straight and meaningless due to the chosen draw ratio of meters. But, indeed, all three representatives show similar curvatures which becomes evident by zooming into the two-dimensional fiber projections, Fig 6 (right). Near the mounting, they hang down almost straight for the first $2 \cdot 10^{-1}$ m before they start to form loops. The observed oscillations have then a typical range of $10^{-3}$ up to $10^{-2}$ m which corresponds with our asymptotic analysis of Sec 2.2, Fig 2. Considering the respective fiber motions for a period of $5 \cdot 10^{-2}$ s, further results are provided by the curvature measures $\mathcal{K}$ that are plotted and statistically evaluated for comparable samples of 500 time points, see Fig 5 and Tab 2. Thereby, all temporal evolutions turn out to be normally distributed. The mean curvature measure of the uncorrelated force, $\bar{v}_\mathrm{n}^{crit} = 10^{-3}$ m/s, differs less than 1% from the one of the correlated force. And also, the standard deviations fit very well, we obtain only differences of 2%. This is an incredibly good coincidence. This choice of $\bar{v}_\mathrm{n}^{crit}$ overcomes simply the singularity stemming from the underlying correlated frozen turbulence pattern and yields therefore better approximation properties than the other variant that incorporates additionally the decay of the vortices.

Summing up, the uncorrelated force model is undeniably a good substitute for the correlated one on the macroscopic fiber scale. Causing a statistically similar fiber behavior, it requires – instead of days – only a few minutes of computational time for the simulation of $5 \cdot 10^{-2}$ s real time motion. Thus, it makes long-time fiber studies possible which is essential for the practical application. Note that the bisection of CPU-time for the deterministic reference case that is listed in Tab 2 comes not only from the skip of Alg 2 and but also from an increase of the (adaptive) time step of one order, up to $\Delta t \sim 10^{-5}$ s. All calculations have been performed on an Intel Xeon processor, 2.8 GHz.

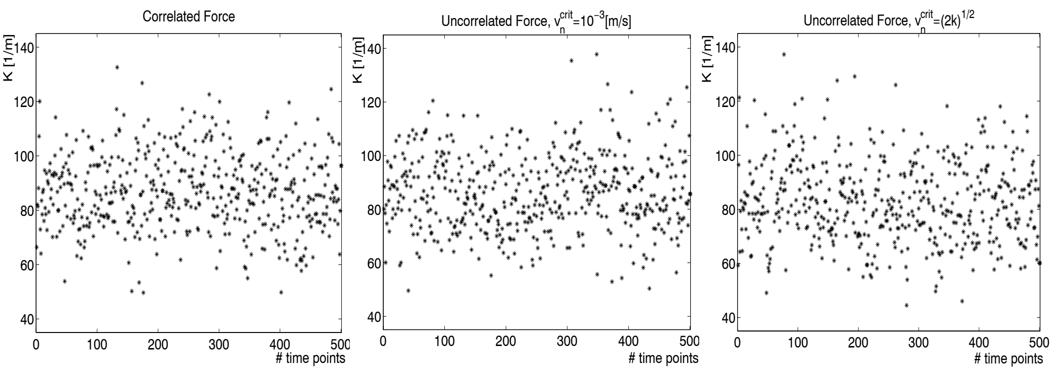


Figure 5: Curvature measures $\mathcal{K}$ over 500 time points for fiber exposed to stochastic forces for $5 \cdot 10^{-2}$ s. From left to right: Results for $\mathbf{f}_{cc}^{air}$, $\mathbf{f}_{uc}^{air}$ with $\bar{v}_\mathrm{n}^{crit} = 10^{-3}$ m/s resp. $\bar{v}_\mathrm{n}^{crit} = (2k)^{1/2}$

| Stochastic Force | Correlated | Uncorrelated | | Without |
|---|---|---|---|---|
| | | $\bar{v}_\mathrm{n}^{crit} = 10^{-3}$[m/s] | $\bar{v}_\mathrm{n}^{crit} = (2k)^{1/2}$ | |
| $\mathcal{K}$ [1/m] | | | | |
| $\mu$ | 86.93 (100%) | 86.33 (−0.69%) | 82.99 (−4.53%) | 0 |
| $\sigma$ | 13.83 (100%) | 14.10 (+2.00%) | 14.94 (+8.03%) | 0 |
| CPU-time | days | ∼4.5 min | ∼4 min | ∼1.5 min |

Table 2: Statistic parameters for the curvature measures $\mathcal{K}$ of Fig 5

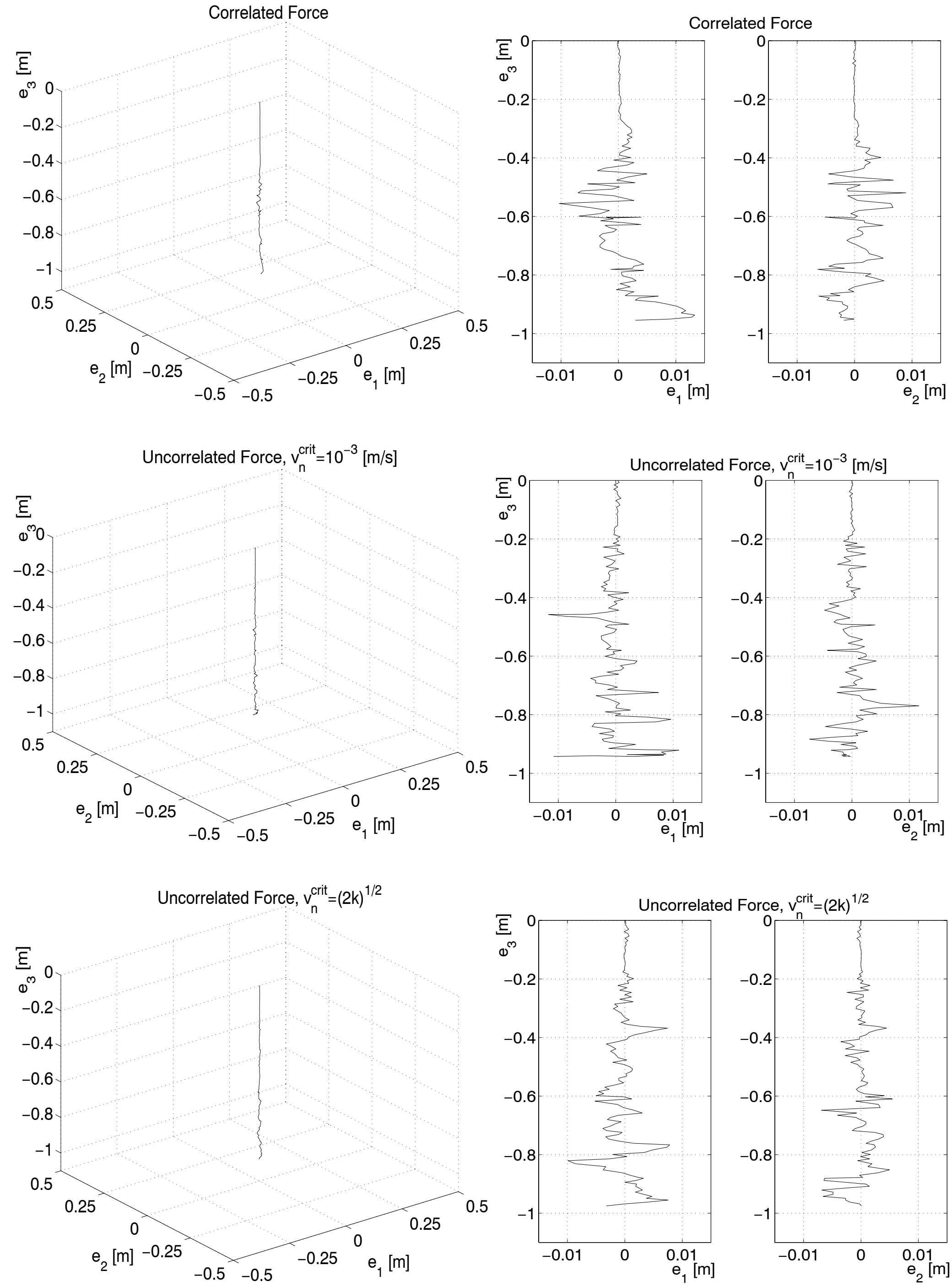


Figure 6: From top to bottom: Fiber exposed to $\mathbf{f}_{cc}^{air}$ and $\mathbf{f}_{uc}^{air}$ with $\bar{v}_{\mathrm{n}}^{crit} = 10^{-3}\,\mathrm{m/s}$ resp. $\bar{v}_{\mathrm{n}}^{crit} = (2k)^{1/2}$. Left: Instantaneous fiber dynamics. Right: Two-dimensional projections zoomed in

# 5 Conclusions and Outlook

In [12], a general aerodynamic force concept is derived on basis of a stochastic $k$-$\epsilon$ turbulence model for the flow field. The turbulence effects on the dynamics of a long slender elastic fiber are modeled by a correlated Gaussian force and in its asymptotic limit on a macroscopic fiber scale by Gaussian white noise with flow-dependent amplitude. Choosing a specific Taylor drag model, this paper has shown the applicability of the force concept for the handling of the complex fiber-turbulence interactions as they occur in a typical melt-spinning process of nonwoven materials. Moreover, it has stated the very good theoretical and numerical approximation properties of the uncorrelated force. The introduction of the uncorrelated aerodynamic force changes the character of the perturbation term into a localized linear integrator such that the fiber dynamics is described by a system of partial differential equations with additive Gaussian white noise. This enables not only a theoretical analysis but also an efficient numerical realization. Adapting the fiber system with appropriate boundary and initial conditions, one can parallelize the presented algorithm and simulate the turbulent deposition region of a melt-spinning process with hundreds of individual endless fibers. However, for this purpose, other aspects have to be taken into account, like fiber-fiber interactions, sticky fiber bunches, conveyor belt effects or the affection of the turbulence by higher concentrated fiber curtains.

# References


[1] G. K. Batchelor, *Slender-body theory for particles of arbitrary cross-section in Stokes flow*, Journal of Fluid Mechanics, 44 (1970), pp. 419–440.

[2] P. J. Brockwell and R. A. Davis, *Time Series: Theory and Methods*, Springer Verlag, Berlin, 1987.

[3] C. Call and J. Kennedy, *Measurements and simulations of particle dispersion in a turbulent flow*, International Journal of Multiphase Flow, 18 (1992), pp. 891–903.

[4] R. G. Cox, *The motion of long slender bodies in a viscous fluid. Part 1. General theory*, Journal of Fluid Mechanics, 44 (1970), pp. 791–810.

[5] L. Devroye, *Non-uniform Random Variate Generation*, Springer Verlag, New York, 1986.

[6] M. Doi and D. Chen, *Simulation of aggregating coilloids in shear flow*, Journal of Chemical Physics, 90 (1989), pp. 5271–5279.

[7] T. Götz and A. Unterreiter, *Analysis and numerics of an integral equation model for slender bodies in low-Reynolds-number flow*, Journal of Integral Equations and Applications, 12 (2000), pp. 225–270.

[8] O. Hinze, *Turbulence*, McGraw-Hill, New York, 2 ed., 1975.

[9] J. B. Keller and S. I. Rubinow, *Slender-body theory for slow viscous flow*, Journal of Fluid Mechanics, 75 (1976), pp. 705–714.

[10] M. E. M. Lee, *Mathematical Models of the Carding Process*, PhD thesis, University of Oxford, 2001.

[11] N. Marheineke, *Turbulent Fibers – On the Motion of Long, Flexible Fibers in Turbulent Flows*, PhD thesis, Technische Universität Kaiserslautern, 2005.

[12] N. Marheineke and R. Wegener, *Fiber dynamics in tubulent flows I: General modeling framework*. Fraunhofer-ITWM, Preprint, 2005.

[13] R. Mei, *Effect of turbulence on the particle settling velocity in the non-linear drag range*, International Journal of Multiphase Flow, 20 (1994), pp. 273–284.

[14] J. A. Olsen and R. J. Kerekes, *The motion of fibres in turbulent flow*, Journal of Fluid Mechanics, 337 (1998), pp. 47–64.

[15] L. M. Pismen and A. Nir, *On the motion of suspended particles in stationary homogeneous turbulence*, Journal of Fluid Mechanics, 84 (1978), pp. 193–206.

[16] F. R. Russel and D. J. Klingenberg, *Dynamic simulation of flexible fibers composed of linked rigid bodies*, Journal of Chemical Physics, 105 (1997), pp. 2949–2960.

[17] T. H. Shih and J. L. Lumley, *Second-order modelling of particle dispersion in a turbulent flow*, Journal of Fluid Mechanics, 163 (1986), pp. 349–363.

[18] G. I. Taylor, *Analysis of the swimming of long and narrow animals*, Proceedings of the Royal Society London, A, 214 (1952), pp. 158–183.

[19] B. Underwood, *Random-walk modeling of turbulent impaction to a smooth wall*, International Journal of Multiphase Flow, 19 (1993), pp. 485–500.

# Published reports of the Fraunhofer ITWM

The PDF-files of the following reports are available under:
***www.itwm.fraunhofer.de/de/zentral__berichte/berichte***

1. D. Hietel, K. Steiner, J. Struckmeier

***A Finite - Volume Particle Method for Compressible Flows***

We derive a new class of particle methods for conservation laws, which are based on numerical flux functions to model the interactions between moving particles. The derivation is similar to that of classical Finite-Volume methods; except that the fixed grid structure in the Finite-Volume method is substituted by so-called mass packets of particles. We give some numerical results on a shock wave solution for Burgers equation as well as the well-known one-dimensional shock tube problem.
(19 pages, 1998)

2. M. Feldmann, S. Seibold

***Damage Diagnosis of Rotors: Application of Hilbert Transform and Multi-Hypothesis Testing***

In this paper, a combined approach to damage diagnosis of rotors is proposed. The intention is to employ signal-based as well as model-based procedures for an improved detection of size and location of the damage. In a first step, Hilbert transform signal processing techniques allow for a computation of the signal envelope and the instantaneous frequency, so that various types of non-linearities due to a damage may be identified and classified based on measured response data. In a second step, a multi-hypothesis bank of Kalman Filters is employed for the detection of the size and location of the damage based on the information of the type of damage provided by the results of the Hilbert transform.
*Keywords: Hilbert transform, damage diagnosis, Kalman filtering, non-linear dynamics*
(23 pages, 1998)

3. Y. Ben-Haim, S. Seibold

***Robust Reliability of Diagnostic Multi-Hypothesis Algorithms: Application to Rotating Machinery***

Damage diagnosis based on a bank of Kalman filters, each one conditioned on a specific hypothesized system condition, is a well recognized and powerful diagnostic tool. This multi-hypothesis approach can be applied to a wide range of damage conditions. In this paper, we will focus on the diagnosis of cracks in rotating machinery. The question we address is: how to optimize the multi-hypothesis algorithm with respect to the uncertainty of the spatial form and location of cracks and their resulting dynamic effects. First, we formulate a measure of the reliability of the diagnostic algorithm, and then we discuss modifications of the diagnostic algorithm for the maximization of the reliability. The reliability of a diagnostic algorithm is measured by the amount of uncertainty consistent with no-failure of the diagnosis. Uncertainty is quantitatively represented with convex models.
*Keywords: Robust reliability, convex models, Kalman filtering, multi-hypothesis diagnosis, rotating machinery, crack diagnosis*
(24 pages, 1998)

4. F.-Th. Lentes, N. Siedow

***Three-dimensional Radiative Heat Transfer in Glass Cooling Processes***

For the numerical simulation of 3D radiative heat transfer in glasses and glass melts, practically applicable mathematical methods are needed to handle such problems optimal using workstation class computers. Since the exact solution would require super-computer capabilities we concentrate on approximate solutions with a high degree of accuracy. The following approaches are studied: 3D diffusion approximations and 3D ray-tracing methods.
(23 pages, 1998)

5. A. Klar, R. Wegener

***A hierarchy of models for multilane vehicular traffic***
***Part I: Modeling***

In the present paper multilane models for vehicular traffic are considered. A microscopic multilane model based on reaction thresholds is developed. Based on this model an Enskog like kinetic model is developed. In particular, care is taken to incorporate the correlations between the vehicles. From the kinetic model a fluid dynamic model is derived. The macroscopic coefficients are deduced from the underlying kinetic model. Numerical simulations are presented for all three levels of description in [10]. Moreover, a comparison of the results is given there.
(23 pages, 1998)

***Part II: Numerical and stochastic investigations***

In this paper the work presented in [6] is continued. The present paper contains detailed numerical investigations of the models developed there. A numerical method to treat the kinetic equations obtained in [6] are presented and results of the simulations are shown. Moreover, the stochastic correlation model used in [6] is described and investigated in more detail.
(17 pages, 1998)

6. A. Klar, N. Siedow

***Boundary Layers and Domain Decomposition for Radiative Heat Transfer and Diffusion Equations: Applications to Glass Manufacturing Processes***

In this paper domain decomposition methods for radiative transfer problems including conductive heat transfer are treated. The paper focuses on semi-transparent materials, like glass, and the associated conditions at the interface between the materials. Using asymptotic analysis we derive conditions for the coupling of the radiative transfer equations and a diffusion approximation. Several test cases are treated and a problem appearing in glass manufacturing processes is computed. The results clearly show the advantages of a domain decomposition approach. Accuracy equivalent to the solution of the global radiative transfer solution is achieved, whereas computation time is strongly reduced.
(24 pages, 1998)

7. I. Choquet

***Heterogeneous catalysis modelling and numerical simulation in rarified gas flows***
***Part I: Coverage locally at equilibrium***

A new approach is proposed to model and simulate numerically heterogeneous catalysis in rarefied gas flows. It is developed to satisfy all together the following points:
1) describe the gas phase at the microscopic scale, as required in rarefied flows,
2) describe the wall at the macroscopic scale, to avoid prohibitive computational costs and consider not only crystalline but also amorphous surfaces,
3) reproduce on average macroscopic laws correlated with experimental results and
4) derive analytic models in a systematic and exact way. The problem is stated in the general framework of a non static flow in the vicinity of a catalytic and non porous surface (without aging). It is shown that the exact and systematic resolution method based on the Laplace transform, introduced previously by the author to model collisions in the gas phase, can be extended to the present problem. The proposed approach is applied to the modelling of the EleyRideal and LangmuirHinshelwood recombinations, assuming that the coverage is locally at equilibrium. The models are developed considering one atomic species and extended to the general case of several atomic species. Numerical calculations show that the models derived in this way reproduce with accuracy behaviors observed experimentally.
(24 pages, 1998)

8. J. Ohser, B. Steinbach, C. Lang

***Efficient Texture Analysis of Binary Images***

A new method of determining some characteristics of binary images is proposed based on a special linear filtering. This technique enables the estimation of the area fraction, the specific line length, and the specific integral of curvature. Furthermore, the specific length of the total projection is obtained, which gives detailed information about the texture of the image. The influence of lateral and directional resolution depending on the size of the applied filter mask is discussed in detail. The technique includes a method of increasing directional resolution for texture analysis while keeping lateral resolution as high as possible.
(17 pages, 1998)

9. J. Orlik

***Homogenization for viscoelasticity of the integral type with aging and shrinkage***

A multiphase composite with periodic distributed inclusions with a smooth boundary is considered in this contribution. The composite component materials are supposed to be linear viscoelastic and aging (of the nonconvolution integral type, for which the Laplace transform with respect to time is not effectively applicable) and are subjected to isotropic shrinkage. The free shrinkage deformation can be considered as a fictitious temperature deformation in the behavior law. The procedure presented in this paper proposes a way to determine average (effective homogenized) viscoelastic and shrinkage (temperature) composite properties and the homogenized stressfield from known properties of the components. This is done by the extension of the asymptotic homogenization technique known for pure elastic nonhomogeneous bodies to the nonhomogeneous thermoviscoelasticity of the integral nonconvolution type. Up to now, the homogenization theory has not covered viscoelasticity of the integral type. SanchezPalencia (1980), Francfort & Suquet (1987) (see [2], [9]) have considered homogenization for viscoelasticity of the differential form and only up to the first derivative order. The integralmodeled viscoelasticity is more general then the differential one and includes almost all known differential models. The homogenization procedure is based on the construction of an asymptotic solution with respect to a period of the composite structure. This reduces the original problem to some auxiliary boundary value problems of elasticity and viscoelasticity on the unit periodic cell, of the same type as the original non-homogeneous problem. The existence and uniqueness results for such problems were obtained for kernels satisfying some constrain conditions. This is done by the extension of the Volterra integral operator theory to the Volterra operators with respect to the time, whose 1 kernels are space linear operators for any fixed time variables. Some ideas of such approach were proposed in [11] and [12], where the Volterra operators with kernels depending additionally on parameter were considered. This manuscript delivers results of the same nature for the case of the spaceoperator kernels.
(20 pages, 1998)

10. J. Mohring

***Helmholtz Resonators with Large Aperture***

The lowest resonant frequency of a cavity resonator is usually approximated by the classical Helmholtz formula. However, if the opening is rather large and the front wall is narrow this formula is no longer valid. Here we present a correction which is of third order in the ratio of the diameters of aperture and cavity. In addition to the high accuracy it allows to estimate the damping due to radiation. The result is found by applying the method of matched asymptotic expansions. The correction contains form factors describing the shapes of opening and cavity. They are computed for a number of standard geometries. Results are compared with numerical computations.
(21 pages, 1998)

11. H. W. Hamacher, A. Schöbel

***On Center Cycles in Grid Graphs***

Finding “good” cycles in graphs is a problem of great interest in graph theory as well as in locational analysis. We show that the center and median problems are NP hard in general graphs. This result holds both for the variable cardinality case (i.e. all cycles of the graph are considered) and the fixed cardinality case (i.e. only cycles with a given cardinality p are feasible). Hence it is of interest to investigate special cases where the problem is solvable in polynomial time. In grid graphs, the variable cardinality case is, for instance, trivially solvable if the shape of the cycle can be chosen freely. If the shape is fixed to be a rectangle one can analyze rectangles in grid graphs with, in sequence, fixed dimension, fixed cardinality, and variable cardinality. In all cases a complete characterization of the optimal cycles and closed form expressions of the optimal objective values are given, yielding polynomial time algorithms for all cases of center rectangle problems. Finally, it is shown that center cycles can be chosen as rectangles for small cardinalities such that the center cycle problem in grid graphs is in these cases completely solved.
(15 pages, 1998)

12. H. W. Hamacher, K.-H. Küfer

***Inverse radiation therapy planning - a multiple objective optimisation approach***

For some decades radiation therapy has been proved successful in cancer treatment. It is the major task of clinical radiation treatment planning to realize on the one hand a high level dose of radiation in the cancer tissue in order to obtain maximum tumor control. On the other hand it is obvious that it is absolutely necessary to keep in the tissue outside the tumor, particularly in organs at risk, the unavoidable radiation as low as possible.
No doubt, these two objectives of treatment planning - high level dose in the tumor, low radiation outside the tumor - have a basically contradictory nature. Therefore, it is no surprise that inverse mathematical models with dose distribution bounds tend to be infeasible in most cases. Thus, there is need for approximations compromising between overdosing the organs at risk and underdosing the target volume.
Differing from the currently used time consuming iterative approach, which measures deviation from an ideal (non-achievable) treatment plan using recursively trial-and-error weights for the organs of interest, we go a new way trying to avoid a priori weight choices and consider the treatment planning problem as a multiple objective linear programming problem: with each organ of interest, target tissue as well as organs at risk, we associate an objective function measuring the maximal deviation from the prescribed doses.
We build up a data base of relatively few efficient solutions representing and approximating the variety of Pareto solutions of the multiple objective linear programming problem. This data base can be easily scanned by physicians looking for an adequate treatment plan with the aid of an appropriate online tool.
(14 pages, 1999)

13. C. Lang, J. Ohser, R. Hilfer

***On the Analysis of Spatial Binary Images***

This paper deals with the characterization of microscopically heterogeneous, but macroscopically homogeneous spatial structures. A new method is presented which is strictly based on integral-geometric formulae such as Crofton’s intersection formulae and Hadwiger’s recursive definition of the Euler number. The corresponding algorithms have clear advantages over other techniques. As an example of application we consider the analysis of spatial digital images produced by means of Computer Assisted Tomography.
(20 pages, 1999)

14. M. Junk

***On the Construction of Discrete Equilibrium Distributions for Kinetic Schemes***

A general approach to the construction of discrete equilibrium distributions is presented. Such distribution functions can be used to set up Kinetic Schemes as well as Lattice Boltzmann methods. The general principles are also applied to the construction of Chapman Enskog distributions which are used in Kinetic Schemes for compressible Navier-Stokes equations.
(24 pages, 1999)

15. M. Junk, S. V. Raghurame Rao

***A new discrete velocity method for Navier-Stokes equations***

The relation between the Lattice Boltzmann Method, which has recently become popular, and the Kinetic Schemes, which are routinely used in Computational Fluid Dynamics, is explored. A new discrete velocity model for the numerical solution of Navier-Stokes equations for incompressible fluid flow is presented by combining both the approaches. The new scheme can be interpreted as a pseudo-compressibility method and, for a particular choice of parameters, this interpretation carries over to the Lattice Boltzmann Method.
(20 pages, 1999)

16. H. Neunzert

***Mathematics as a Key to Key Technologies***

The main part of this paper will consist of examples, how mathematics really helps to solve industrial problems; these examples are taken from our Institute for Industrial Mathematics, from research in the Technomathematics group at my university, but also from ECMI groups and a company called TecMath, which originated 10 years ago from my university group and has already a very successful history.
(39 pages (4 PDF-Files), 1999)

17. J. Ohser, K. Sandau

***Considerations about the Estimation of the Size Distribution in Wicksell’s Corpuscle Problem***

Wicksell’s corpuscle problem deals with the estimation of the size distribution of a population of particles, all having the same shape, using a lower dimensional sampling probe. This problem was originary formulated for particle systems occurring in life sciences but its solution is of actual and increasing interest in materials science. From a mathematical point of view, Wicksell’s problem is an inverse problem where the interesting size distribution is the unknown part of a Volterra equation. The problem is often regarded ill-posed, because the structure of the integrand implies unstable numerical solutions. The accuracy of the numerical solutions is considered here using the condition number, which allows to compare different numerical methods with different (equidistant) class sizes and which indicates, as one result, that a finite section thickness of the probe reduces the numerical problems. Furthermore, the relative error of estimation is computed which can be split into two parts. One part consists of the relative discretization error that increases for increasing class size, and the second part is related to the relative statistical error which increases with decreasing class size. For both parts, upper bounds can be given and the sum of them indicates an optimal class width depending on some specific constants.
(18 pages, 1999)

18. E. Carrizosa, H. W. Hamacher, R. Klein, S. Nickel

***Solving nonconvex planar location problems by finite dominating sets***

It is well-known that some of the classical location problems with polyhedral gauges can be solved in polynomial time by finding a finite dominating set, i. e. a finite set of candidates guaranteed to contain at least one optimal location.
In this paper it is first established that this result holds for a much larger class of problems than currently considered in the literature. The model for which this result can be proven includes, for instance, location problems with attraction and repulsion, and location-allocation problems.
Next, it is shown that the approximation of general gauges by polyhedral ones in the objective function of our general model can be analyzed with regard to the subsequent error in the optimal objective value. For the approximation problem two different approaches are described, the sandwich procedure and the greedy algorithm. Both of these approaches lead - for fixed epsilon - to polynomial approximation algorithms with accuracy epsilon for solving the general model considered in this paper.
*Keywords: Continuous Location, Polyhedral Gauges, Finite Dominating Sets, Approximation, Sandwich Algorithm, Greedy Algorithm*
(19 pages, 2000)

19. A. Becker

***A Review on Image Distortion Measures***

Within this paper we review image distortion measures. A distortion measure is a criterion that assigns a “quality number” to an image. We distinguish between mathematical distortion measures and those distortion measures in-cooperating a priori knowledge about the imaging devices ( e. g. satellite images), image processing algorithms or the human physiology. We will consider representative examples of different kinds of distortion measures and are going to discuss them.
*Keywords: Distortion measure, human visual system*
(26 pages, 2000)

20. H. W. Hamacher, M. Labbé, S. Nickel, T. Sonneborn

***Polyhedral Properties of the Uncapacitated Multiple Allocation Hub Location Problem***

We examine the feasibility polyhedron of the uncapacitated hub location problem (UHL) with multiple allocation, which has applications in the fields of air passenger and cargo transportation, telecommunication and postal delivery services. In particular we determine the dimension and derive some classes of facets of this polyhedron. We develop some general rules about lifting facets from the uncapacitated facility location (UFL) for UHL and projecting facets from UHL to UFL. By applying these rules we get a new class of facets for UHL which dominates the inequalities in the original formulation. Thus we get a new formulation of UHL whose constraints are all facet–defining. We show its superior computational performance by benchmarking it on a well known data set.
*Keywords: integer programming, hub location, facility location, valid inequalities, facets, branch and cut*
(21 pages, 2000)

21. H. W. Hamacher, A. Schöbel

***Design of Zone Tariff Systems in Public Transportation***

Given a public transportation system represented by its stops and direct connections between stops, we consider two problems dealing with the prices for the customers: The fare problem in which subsets of stops are already aggregated to zones and “good” tariffs have to be found in the existing zone system. Closed form solutions for the fare problem are presented for three objective functions. In the zone problem the design of the zones is part of the problem. This problem is NP hard and we therefore propose three heuristics which prove to be very successful in the redesign of one of Germany’s transportation systems.
(30 pages, 2001)

22. D. Hietel, M. Junk, R. Keck, D. Teleaga

***The Finite-Volume-Particle Method for Conservation Laws***

In the Finite-Volume-Particle Method (FVPM), the weak formulation of a hyperbolic conservation law is discretized by restricting it to a discrete set of test functions. In contrast to the usual Finite-Volume approach, the test functions are not taken as characteristic functions of the control volumes in a spatial grid, but are chosen from a partition of unity with smooth and overlapping partition functions (the particles), which can even move along pre- scribed velocity fields. The information exchange between particles is based on standard numerical flux functions. Geometrical information, similar to the surface area of the cell faces in the Finite-Volume Method and the corresponding normal directions are given as integral quantities of the partition functions. After a brief derivation of the Finite-Volume-Particle Method, this work focuses on the role of the geometric coefficients in the scheme.
(16 pages, 2001)

23. T. Bender, H. Hennes, J. Kalcsics, M. T. Melo, S. Nickel

***Location Software and Interface with GIS and Supply Chain Management***

The objective of this paper is to bridge the gap between location theory and practice. To meet this objective focus is given to the development of software capable of addressing the different needs of a wide group of users. There is a very active community on location theory encompassing many research fields such as operations research, computer science, mathematics, engineering, geography, economics and marketing. As a result, people working on facility location problems have a very diverse background and also different needs regarding the software to solve these problems. For those interested in non-commercial applications (e. g. students and researchers), the library of location algorithms (LoLA can be of considerable assistance. LoLA contains a collection of efficient algorithms for solving planar, network and discrete facility location problems. In this paper, a detailed description of the functionality of LoLA is presented. In the fields of geography and marketing, for instance, solving facility location problems requires using large amounts of demographic data. Hence, members of these groups (e. g. urban planners and sales managers) often work with geographical information too s. To address the specific needs of these users, LoLA was inked to a geographical information system (GIS) and the details of the combined functionality are described in the paper. Finally, there is a wide group of practitioners who need to solve large problems and require special purpose software with a good data interface. Many of such users can be found, for example, in the area of supply chain management (SCM). Logistics activities involved in strategic SCM include, among others, facility location planning. In this paper, the development of a commercial location software tool is also described. The too is embedded in the Advanced Planner and Optimizer SCM software developed by SAP AG, Walldorf, Germany. The paper ends with some conclusions and an outlook to future activities.
*Keywords: facility location, software development, geographical information systems, supply chain management*
(48 pages, 2001)

24. H. W. Hamacher, S. A. Tjandra

***Mathematical Modelling of Evacuation Problems: A State of Art***

This paper details models and algorithms which can be applied to evacuation problems. While it concentrates on building evacuation many of the results are applicable also to regional evacuation. All models consider the time as main parameter, where the travel time between components of the building is part of the input and the overall evacuation time is the output. The paper distinguishes between macroscopic and microscopic evacuation models both of which are able to capture the evacuees' movement over time.
Macroscopic models are mainly used to produce good lower bounds for the evacuation time and do not consider any individual behavior during the emergency situation. These bounds can be used to analyze existing buildings or help in the design phase of planning a building. Macroscopic approaches which are based on dynamic network flow models (minimum cost dynamic flow, maximum dynamic flow, universal maximum flow, quickest path and quickest flow) are described. A special feature of the presented approach is the fact, that travel times of evacuees are not restricted to be constant, but may be density dependent. Using multicriteria optimization priority regions and blockage due to fire or smoke may be considered. It is shown how the modelling can be done using time parameter either as discrete or continuous parameter.
Microscopic models are able to model the individual evacuee's characteristics and the interaction among evacuees which influence their movement. Due to the corresponding huge amount of data one uses simulation approaches. Some probabilistic laws for individual evacuee's movement are presented. Moreover ideas to model the evacuee's movement using cellular automata (CA) and resulting software are presented.
In this paper we will focus on macroscopic models and only summarize some of the results of the microscopic approach. While most of the results are applicable to general evacuation situations, we concentrate on building evacuation.
(44 pages, 2001)

25. J. Kuhnert, S. Tiwari

***Grid free method for solving the Poisson equation***

A Grid free method for solving the Poisson equation is presented. This is an iterative method. The method is based on the weighted least squares approximation in which the Poisson equation is enforced to be satisfied in every iterations. The boundary conditions can also be enforced in the iteration process. This is a local approximation procedure. The Dirichlet, Neumann and mixed boundary value problems on a unit square are presented and the analytical solutions are compared with the exact solutions. Both solutions matched perfectly.
*Keywords: Poisson equation, Least squares method, Grid free method*
(19 pages, 2001)

26. T. Götz, H. Rave, D. Reinel-Bitzer, K. Steiner, H. Tiemeier

***Simulation of the fiber spinning process***

To simulate the influence of process parameters to the melt spinning process a fiber model is used and coupled with CFD calculations of the quench air flow. In the fiber model energy, momentum and mass balance are solved for the polymer mass flow. To calculate the quench air the Lattice Boltzmann method is used. Simulations and experiments for different process parameters and hole configurations are compared and show a good agreement.
*Keywords: Melt spinning, fiber model, Lattice Boltzmann, CFD*
(19 pages, 2001)

27. A. Zemitis

***On interaction of a liquid film with an obstacle***

In this paper mathematical models for liquid films generated by impinging jets are discussed. Attention is stressed to the interaction of the liquid film with some obstacle. S. G. Taylor [Proc. R. Soc. London Ser. A 253, 313 (1959)] found that the liquid film generated by impinging jets is very sensitive to properties of the wire which was used as an obstacle. The aim of this presentation is to propose a modification of the Taylor's model, which allows to simulate the film shape in cases, when the angle between jets is different from 180°. Numerical results obtained by discussed models give two different shapes of the liquid film similar as in Taylors experiments. These two shapes depend on the regime: either droplets are produced close to the obstacle or not. The difference between two regimes becomes larger if the angle between jets decreases. Existence of such two regimes can be very essential for some applications of impinging jets, if the generated liquid film can have a contact with obstacles.
*Keywords: impinging jets, liquid film, models, numerical solution, shape*
(22 pages, 2001)

28. I. Ginzburg, K. Steiner

***Free surface lattice-Boltzmann method to model the filling of expanding cavities by Bingham Fluids***

The filling process of viscoplastic metal alloys and plastics in expanding cavities is modelled using the lattice Boltzmann method in two and three dimensions. These models combine the regularized Bingham model for viscoplastic with a free-interface algorithm. The latter is based on a modified immiscible lattice Boltzmann model in which one species is the fluid and the other one is considered as vacuum. The boundary conditions at the curved liquid-vacuum interface are met without any geometrical front reconstruction from a first-order Chapman-Enskog expansion. The numerical results obtained with these models are found in good agreement with available theoretical and numerical analysis.
Keywords: Generalized LBE, free-surface phenomena, interface boundary conditions, filling processes, Bingham viscoplastic model, regularized models
(22 pages, 2001)

29. H. Neunzert

***»Denn nichts ist für den Menschen als Menschen etwas wert, was er nicht mit Leidenschaft tun kann«***
***Vortrag anlässlich der Verleihung des Akademiepreises des Landes Rheinland-Pfalz am 21.11.2001***

Was macht einen guten Hochschullehrer aus? Auf diese Frage gibt es sicher viele verschiedene, fachbezogene Antworten, aber auch ein paar allgemeine Gesichtspunkte: es bedarf der »Leidenschaft« für die Forschung (Max Weber), aus der dann auch die Begeisterung für die Lehre erwächst. Forschung und Lehre gehören zusammen, um die Wissenschaft als lebendiges Tun vermitteln zu können. Der Vortrag gibt Beispiele dafür, wie in angewandter Mathematik Forschungsaufgaben aus praktischen Alltagsproblemstellungen erwachsen, die in die Lehre auf verschiedenen Stufen (Gymnasium bis Graduiertenkolleg) einfließen; er leitet damit auch zu einem aktuellen Forschungsgebiet, der Mehrskalenanalyse mit ihren vielfältigen Anwendungen in Bildverarbeitung, Materialentwicklung und Strömungsmechanik über, was aber nur kurz gestreift wird. Mathematik erscheint hier als eine moderne Schlüsseltechnologie, die aber auch enge Beziehungen zu den Geistes- und Sozialwissenschaften hat.
*Keywords: Lehre, Forschung, angewandte Mathematik, Mehrskalenanalyse, Strömungsmechanik*
(18 pages, 2001)

30. J. Kuhnert, S. Tiwari

***Finite pointset method based on the projection method for simulations of the incompressible Navier-Stokes equations***

A Lagrangian particle scheme is applied to the projection method for the incompressible Navier-Stokes equations. The approximation of spatial derivatives is obtained by the weighted least squares method. The pressure Poisson equation is solved by a local iterative procedure with the help of the least squares method. Numerical tests are performed for two dimensional cases. The Couette flow, Poiseuelle flow, decaying shear flow and the driven cavity flow are presented. The numerical solutions are obtained for stationary as well as instationary cases and are compared with the analytical solutions for channel flows. Finally, the driven cavity in a unit square is considered and the stationary solution obtained from this scheme is compared with that from the finite element method.
*Keywords: Incompressible Navier-Stokes equations, Meshfree method, Projection method, Particle scheme, Least squares approximation*
*AMS subject classification: 76D05, 76M28*
(25 pages, 2001)

31. R. Korn, M. Krekel

***Optimal Portfolios with Fixed Consumption or Income Streams***

We consider some portfolio optimisation problems where either the investor has a desire for an a priori specified consumption stream or/and follows a deterministic pay in scheme while also trying to maximize expected utility from final wealth. We derive explicit closed form solutions for continuous and discrete monetary streams. The mathematical method used is classical stochastic control theory.
Keywords: Portfolio optimisation, stochastic control, HJB equation, discretisation of control problems.
(23 pages, 2002)

32. M. Krekel

***Optimal portfolios with a loan dependent credit spread***

If an investor borrows money he generally has to pay higher interest rates than he would have received, if he had put his funds on a savings account. The classical model of continuous time portfolio optimisation ignores this effect. Since there is obviously a connection between the default probability and the total

percentage of wealth, which the investor is in debt, we study portfolio optimisation with a control dependent interest rate. Assuming a logarithmic and a power utility function, respectively, we prove explicit formulae of the optimal control.
*Keywords: Portfolio optimisation, stochastic control, HJB equation, credit spread, log utility, power utility, non-linear wealth dynamics*
(25 pages, 2002)

33. J. Ohser, W. Nagel, K. Schladitz

***The Euler number of discretized sets - on the choice of adjacency in homogeneous lattices***

Two approaches for determining the Euler-Poincaré characteristic of a set observed on lattice points are considered in the context of image analysis { the integral geometric and the polyhedral approach. Information about the set is assumed to be available on lattice points only. In order to retain properties of the Euler number and to provide a good approximation of the true Euler number of the original set in the Euclidean space, the appropriate choice of adjacency in the lattice for the set and its background is crucial. Adjacencies are defined using tessellations of the whole space into polyhedrons. In R 3 , two new 14 adjacencies are introduced additionally to the well known 6 and 26 adjacencies. For the Euler number of a set and its complement, a consistency relation holds. Each of the pairs of adjacencies (14:1; 14:1), (14:2; 14:2), (6; 26), and (26; 6) is shown to be a pair of complementary adjacencies with respect to this relation. That is, the approximations of the Euler numbers are consistent if the set and its background (complement) are equipped with this pair of adjacencies. Furthermore, sufficient conditions for the correctness of the approximations of the Euler number are given. The analysis of selected microstructures and a simulation study illustrate how the estimated Euler number depends on the chosen adjacency. It also shows that there is not a uniquely best pair of adjacencies with respect to the estimation of the Euler number of a set in Euclidean space.
*Keywords: image analysis, Euler number, neighborhod relationships, cuboidal lattice*
(32 pages, 2002)

34. I. Ginzburg, K. Steiner

***Lattice Boltzmann Model for Free-Surface flow and Its Application to Filling Process in Casting***

A generalized lattice Boltzmann model to simulate free-surface is constructed in both two and three dimensions. The proposed model satisfies the interfacial boundary conditions accurately. A distinctive feature of the model is that the collision processes is carried out only on the points occupied partially or fully by the fluid. To maintain a sharp interfacial front, the method includes an anti-diffusion algorithm. The unknown distribution functions at the interfacial region are constructed according to the first order Chapman-Enskog analysis. The interfacial boundary conditions are satisfied exactly by the coefficients in the Chapman-Enskog expansion. The distribution functions are naturally expressed in the local interfacial coordinates. The macroscopic quantities at the interface are extracted from the least-square solutions of a locally linearized system obtained from the known distribution functions. The proposed method does not require any geometric front construction and is robust for any interfacial topology. Simulation results of realistic filling process are presented: rectangular cavity in two dimensions and Hammer box, Campbell box, Sheffield box, and Motorblock in three dimensions. To enhance the stability at high Reynolds numbers, various upwind-type schemes are developed. Free-slip and no-slip boundary conditions are also discussed.
*Keywords: Lattice Boltzmann models; free-surface phenomena; interface boundary conditions; filling processes; injection molding; volume of fluid method; interface boundary conditions; advection-schemes; upwind-schemes*
(54 pages, 2002)

35. M. Günther, A. Klar, T. Materne, R. Wegener

***Multivalued fundamental diagrams and stop and go waves for continuum traffic equations***

In the present paper a kinetic model for vehicular traffic leading to multivalued fundamental diagrams is developed and investigated in detail. For this model phase transitions can appear depending on the local density and velocity of the flow. A derivation of associated macroscopic traffic equations from the kinetic equation is given. Moreover, numerical experiments show the appearance of stop and go waves for highway traffic with a bottleneck.
*Keywords: traffic flow, macroscopic equations, kinetic derivation, multivalued fundamental diagram, stop and go waves, phase transitions*
(25 pages, 2002)

36. S. Feldmann, P. Lang, D. Prätzel-Wolters

***Parameter influence on the zeros of network determinants***

To a network N(q) with determinant D(s;q) depending on a parameter vector q Î Rr via identification of some of its vertices, a network N^ (q) is assigned. The paper deals with procedures to find N^ (q), such that its determinant D^ (s;q) admits a factorization in the determinants of appropriate subnetworks, and with the estimation of the deviation of the zeros of D^ from the zeros of D. To solve the estimation problem state space methods are applied.
*Keywords: Networks, Equicofactor matrix polynomials, Realization theory, Matrix perturbation theory*
(30 pages, 2002)

37. K. Koch, J. Ohser, K. Schladitz

***Spectral theory for random closed sets and estimating the covariance via frequency space***

A spectral theory for stationary random closed sets is developed and provided with a sound mathematical basis. Definition and proof of existence of the Bartlett spectrum of a stationary random closed set as well as the proof of a Wiener-Khintchine theorem for the power spectrum are used to two ends: First, well known second order characteristics like the covariance can be estimated faster than usual via frequency space. Second, the Bartlett spectrum and the power spectrum can be used as second order characteristics in frequency space. Examples show, that in some cases information about the random closed set is easier to obtain from these characteristics in frequency space than from their real world counterparts.
*Keywords: Random set, Bartlett spectrum, fast Fourier transform, power spectrum*
(28 pages, 2002)

38. D. d'Humières, I. Ginzburg

***Multi-reflection boundary conditions for lattice Boltzmann models***

We present a unified approach of several boundary conditions for lattice Boltzmann models. Its general framework is a generalization of previously introduced schemes such as the bounce-back rule, linear or quadratic interpolations, etc. The objectives are two fold: first to give theoretical tools to study the existing boundary conditions and their corresponding accuracy; secondly to design formally third- order accurate boundary conditions for general flows. Using these boundary conditions, Couette and Poiseuille flows are exact solution of the lattice Boltzmann models for a Reynolds number Re = 0 (Stokes limit).
Numerical comparisons are given for Stokes flows in periodic arrays of spheres and cylinders, linear periodic array of cylinders between moving plates and for Navier-Stokes flows in periodic arrays of cylinders for Re < 200. These results show a significant improvement of the overall accuracy when using the linear interpolations instead of the bounce-back reflection (up to an order of magnitude on the hydrodynamics fields). Further improvement is achieved with the new multi-reflection boundary conditions, reaching a level of accuracy close to the quasi-analytical reference solutions, even for rather modest grid resolutions and few points in the narrowest channels. More important, the pressure and velocity fields in the vicinity of the obstacles are much smoother with multi-reflection than with the other boundary conditions.
Finally the good stability of these schemes is highlighted by some simulations of moving obstacles: a cylinder between flat walls and a sphere in a cylinder.
*Keywords: lattice Boltzmann equation, boudary condistions, bounce-back rule, Navier-Stokes equation*
(72 pages, 2002)

39. R. Korn

***Elementare Finanzmathematik***

Im Rahmen dieser Arbeit soll eine elementar gehaltene Einführung in die Aufgabenstellungen und Prinzipien der modernen Finanzmathematik gegeben werden. Insbesondere werden die Grundlagen der Modellierung von Aktienkursen, der Bewertung von Optionen und der Portfolio-Optimierung vorgestellt. Natürlich können die verwendeten Methoden und die entwickelte Theorie nicht in voller Allgemeinheit für den Schulunterricht verwendet werden, doch sollen einzelne Prinzipien so heraus gearbeitet werden, dass sie auch an einfachen Beispielen verstanden werden können.
*Keywords: Finanzmathematik, Aktien, Optionen, Portfolio-Optimierung, Börse, Lehrerweiterbildung, Mathematikunterricht*
(98 pages, 2002)

40. J. Kallrath, M. C. Müller, S. Nickel

***Batch Presorting Problems: Models and Complexity Results***

In this paper we consider short term storage systems. We analyze presorting strategies to improve the effiency of these storage systems. The presorting task is called Batch PreSorting Problem (BPSP). The BPSP is a variation of an assigment problem, i. e., it has an assigment problem kernel and some additional constraints. We present different types of these presorting problems, introduce mathematical programming formulations and prove the NP-completeness for one type of the BPSP. Experiments are carried out in order to compare the different model formulations and to investigate the behavior of these models.
*Keywords: Complexity theory, Integer programming, Assigment, Logistics*
(19 pages, 2002)

41. J. Linn

***On the frame-invariant description of the phase space of the Folgar-Tucker equation***

The Folgar-Tucker equation is used in flow simulations of fiber suspensions to predict fiber orientation depending on the local flow. In this paper, a complete, frame-invariant description of the phase space of this differential equation is presented for the first time.
*Key words: fiber orientation, Folgar-Tucker equation, injection molding*
(5 pages, 2003)

42. T. Hanne, S. Nickel

***A Multi-Objective Evolutionary Algorithm for Scheduling and Inspection Planning in Software Development Projects***

In this article, we consider the problem of planning inspections and other tasks within a software development (SD) project with respect to the objectives quality (no. of defects), project duration, and costs. Based on a discrete-event simulation model of SD processes comprising the phases coding, inspection, test, and rework, we present a simplified formulation of the problem as a multiobjective optimization problem. For solving the problem (i. e. finding an approximation of the efficient set) we develop a multiobjective evolutionary algorithm. Details of the algorithm are discussed as well as results of its application to sample problems.
*Key words: multiple objective programming, project management and scheduling, software development, evolutionary algorithms, efficient set*
(29 pages, 2003)

43. T. Bortfeld , K.-H. Küfer, M. Monz, A. Scherrer, C. Thieke, H. Trinkaus

***Intensity-Modulated Radiotherapy - A Large Scale Multi-Criteria Programming Problem -***

Radiation therapy planning is always a tight rope walk between dangerous insufficient dose in the target volume and life threatening overdosing of organs at risk. Finding ideal balances between these inherently contradictory goals challenges dosimetrists and physicians in their daily practice. Today's planning systems are typically based on a single evaluation function that measures the quality of a radiation treatment plan. Unfortunately, such a one dimensional approach cannot satisfactorily map the different backgrounds of physicians and the patient dependent necessities. So, too often a time consuming iteration process between evaluation of dose distribution and redefinition of the evaluation function is needed.
In this paper we propose a generic multi-criteria approach based on Pareto's solution concept. For each entity of interest - target volume or organ at risk a structure dependent evaluation function is defined measuring deviations from ideal doses that are calculated from statistical functions. A reasonable bunch of clinically meaningful Pareto optimal solutions are stored in a data base, which can be interactively searched by physicians. The system guarantees dynamical planning as well as the discussion of tradeoffs between different entities.
Mathematically, we model the upcoming inverse problem as a multi-criteria linear programming problem. Because of the large scale nature of the problem it is not possible to solve the problem in a 3D-setting without adaptive reduction by appropriate approximation schemes.
Our approach is twofold: First, the discretization of the continuous problem is based on an adaptive hierarchical clustering process which is used for a local refinement of constraints during the optimization procedure. Second, the set of Pareto optimal solutions is approximated by an adaptive grid of representatives that are found by a hybrid process of calculating extreme compromises and interpolation methods.
*Keywords: multiple criteria optimization, representative systems of Pareto solutions, adaptive triangulation, clustering and disaggregation techniques, visualization of Pareto solutions, medical physics, external beam radiotherapy planning, intensity modulated radiotherapy*
(31 pages, 2003)

44. T. Halfmann, T. Wichmann

***Overview of Symbolic Methods in Industrial Analog Circuit Design***

Industrial analog circuits are usually designed using numerical simulation tools. To obtain a deeper circuit understanding, symbolic analysis techniques can additionally be applied. Approximation methods which reduce the complexity of symbolic expressions are needed in order to handle industrial-sized problems.
This paper will give an overview to the field of symbolic analog circuit analysis. Starting with a motivation, the state-of-the-art simplification algorithms for linear as well as for nonlinear circuits are presented. The basic ideas behind the different techniques are described, whereas the technical details can be found in the cited references. Finally, the application of linear and nonlinear symbolic analysis will be shown on two example circuits.
*Keywords: CAD, automated analog circuit design, symbolic analysis, computer algebra, behavioral modeling, system simulation, circuit sizing, macro modeling, differential-algebraic equations, index*
(17 pages, 2003)

45. S. E. Mikhailov, J. Orlik

***Asymptotic Homogenisation in Strength and Fatigue Durability Analysis of Composites***

Asymptotic homogenisation technique and two-scale convergence is used for analysis of macro-strength and fatigue durability of composites with a periodic structure under cyclic loading. The linear damage accumulation rule is employed in the phenomenological micro-durability conditions (for each component of the composite) under varying cyclic loading. Both local and non-local strength and durability conditions are analysed. The strong convergence of the strength and fatigue damage measure as the structure period tends to zero is proved and their limiting values are estimated.
*Keywords: multiscale structures, asymptotic homogenization, strength, fatigue, singularity, non-local conditions*
(14 pages, 2003)

46. P. Domínguez-Marín, P. Hansen, N. Mladenović , S. Nickel

***Heuristic Procedures for Solving the Discrete Ordered Median Problem***

We present two heuristic methods for solving the Discrete Ordered Median Problem (DOMP), for which no such approaches have been developed so far. The DOMP generalizes classical discrete facility location problems, such as the p-median, p-center and Uncapacitated Facility Location problems. The first procedure proposed in this paper is based on a genetic algorithm developed by Moreno Vega [MV96] for p-median and p-center problems. Additionally, a second heuristic approach based on the Variable Neighborhood Search metaheuristic (VNS) proposed by Hansen & Mladenovic [HM97] for the p-median problem is described. An extensive numerical study is presented to show the efficiency of both heuristics and compare them.
*Keywords: genetic algorithms, variable neighborhood search, discrete facility location*
(31 pages, 2003)

47. N. Boland, P. Domínguez-Marín, S. Nickel, J. Puerto

***Exact Procedures for Solving the Discrete Ordered Median Problem***

The Discrete Ordered Median Problem (DOMP) generalizes classical discrete location problems, such as the N-median, N-center and Uncapacitated Facility Location problems. It was introduced by Nickel [16], who formulated it as both a nonlinear and a linear integer program. We propose an alternative integer linear programming formulation for the DOMP, discuss relationships between both integer linear programming formulations, and show how properties of optimal solutions can be used to strengthen these formulations. Moreover, we present a specific branch and bound procedure to solve the DOMP more efficiently. We test the integer linear programming formulations and this branch and bound method computationally on randomly generated test problems.
*Keywords: discrete location, Integer programming*
(41 pages, 2003)

48. S. Feldmann, P. Lang

***Padé-like reduction of stable discrete linear systems preserving their stability***

A new stability preserving model reduction algorithm for discrete linear SISO-systems based on their impulse response is proposed. Similar to the Padé approximation, an equation system for the Markov parameters involving the Hankel matrix is considered, that here however is chosen to be of very high dimension. Although this equation system therefore in general cannot be solved exactly, it is proved that the approximate solution, computed via the Moore-Penrose inverse, gives rise to a stability preserving reduction scheme, a property that cannot be guaranteed for the Padé approach. Furthermore, the proposed algorithm is compared to another stability preserving reduction approach, namely the balanced truncation method, showing comparable performance of the reduced systems. The balanced truncation method however starts from a state space description of the systems and in general is expected to be more computational demanding.
*Keywords: Discrete linear systems, model reduction, stability, Hankel matrix, Stein equation*
(16 pages, 2003)

49. J. Kallrath, S. Nickel

***A Polynomial Case of the Batch Presorting Problem***

This paper presents new theoretical results for a special case of the batch presorting problem (BPSP). We will show tht this case can be solved in polynomial time. Offline and online algorithms are presented for solving the BPSP. Competetive analysis is used for comparing the algorithms.
*Keywords: batch presorting problem, online optimization, competetive analysis, polynomial algorithms, logistics*
(17 pages, 2003)

50. T. Hanne, H. L. Trinkaus

***knowCube for MCDM – Visual and Interactive Support for Multicriteria Decision Making***

In this paper, we present a novel multicriteria decision support system (MCDSS), called knowCube, consisting of components for knowledge organization, generation, and navigation. Knowledge organization rests upon a database for managing qualitative and quantitative criteria, together with add-on information. Knowledge generation serves filling the database via e.g. identification, optimization, classification or simulation. For "finding needles in haycocks", the knowledge navigation component supports graphical database retrieval and interactive, goal-oriented problem solving. Navigation "helpers" are, for instance, cascading criteria aggregations, modifiable metrics, ergonomic interfaces, and customizable visualizations. Examples from real-life projects, e.g. in industrial engineering and in the life sciences, illustrate the application of our MCDSS.
*Key words: Multicriteria decision making, knowledge management, decision support systems, visual interfaces, interactive navigation, real-life applications.*
(26 pages, 2003)

51. O. Iliev, V. Laptev

***On Numerical Simulation of Flow Through Oil Filters***

This paper concerns numerical simulation of flow through oil filters. Oil filters consist of filter housing (filter box), and a porous filtering medium, which completely separates the inlet from the outlet. We discuss mathematical models, describing coupled flows in the pure liquid subregions and in the porous filter media, as well as interface conditions between them. Further, we reformulate the problem in fictitious regions method manner, and discuss peculiarities of the numerical algorithm in solving the coupled system. Next, we show numerical results, validating the model and the algorithm. Finally, we present results from simulation of 3-D oil flow through a real car filter.
*Keywords: oil filters, coupled flow in plain and porous media, Navier-Stokes, Brinkman, numerical simulation*
(8 pages, 2003)

52. W. Dörfler, O. Iliev, D. Stoyanov, D. Vassileva

***On a Multigrid Adaptive Refinement Solver for Saturated Non-Newtonian Flow in Porous Media***

A multigrid adaptive refinement algorithm for non-Newtonian flow in porous media is presented. The saturated flow of a non-Newtonian fluid is described by the continuity equation and the generalized Darcy law. The resulting second order nonlinear elliptic equation is discretized by a finite volume method on a cell-centered grid. A nonlinear full-multigrid, full-approximation-storage algorithm is implemented. As a smoother, a single grid solver based on Picard linearization and Gauss-Seidel relaxation is used. Further, a local refinement multigrid algorithm on a composite grid is developed. A residual based error indicator is used in the adaptive refinement criterion. A special implementation approach is used, which allows us to perform unstructured local refinement in conjunction with the finite volume discretization. Several results from numerical experiments are presented in order to examine the performance of the solver.
*Keywords: Nonlinear multigrid, adaptive refinement, non-Newtonian flow in porous media*
(17 pages, 2003)

53. S. Kruse
***On the Pricing of Forward Starting Options under Stochastic Volatility***
We consider the problem of pricing European forward starting options in the presence of stochastic volatility. By performing a change of measure using the asset price at the time of strike determination as a numeraire, we derive a closed-form solution based on Heston's model of stochastic volatility.
*Keywords: Option pricing, forward starting options, Heston model, stochastic volatility, cliquet options*
(11 pages, 2003)

54. O. Iliev, D. Stoyanov
***Multigrid – adaptive local refinement solver for incompressible flows***
A non-linear multigrid solver for incompressible Navier-Stokes equations, exploiting finite volume discretization of the equations, is extended by adaptive local refinement. The multigrid is the outer iterative cycle, while the SIMPLE algorithm is used as a smoothing procedure. Error indicators are used to define the refinement subdomain. A special implementation approach is used, which allows to perform unstructured local refinement in conjunction with the finite volume discretization. The multigrid - adaptive local refinement algorithm is tested on 2D Poisson equation and further is applied to a lid-driven flows in a cavity (2D and 3D case), comparing the results with bench-mark data. The software design principles of the solver are also discussed.
*Keywords: Navier-Stokes equations, incompressible flow, projection-type splitting, SIMPLE, multigrid methods, adaptive local refinement, lid-driven flow in a cavity*
(37 pages, 2003)

55. V. Starikovicius
***The multiphase flow and heat transfer in porous media***
In first part of this work, summaries of traditional Multiphase Flow Model and more recent Multiphase Mixture Model are presented. Attention is being paid to attempts include various heterogeneous aspects into models. In second part, MMM based differential model for two-phase immiscible flow in porous media is considered. A numerical scheme based on the sequential solution procedure and control volume based finite difference schemes for the pressure and saturation-conservation equations is developed. A computer simulator is built, which exploits object-oriented programming techniques. Numerical result for several test problems are reported.
*Keywords: Two-phase flow in porous media, various formulations, global pressure, multiphase mixture model, numerical simulation*
(30 pages, 2003)

56. P. Lang, A. Sarishvili, A. Wirsen
***Blocked neural networks for knowledge extraction in the software development process***
One of the main goals of an organization developing software is to increase the quality of the software while at the same time to decrease the costs and the duration of the development process. To achieve this, various decisions e.ecting this goal before and during the development process have to be made by the managers. One appropriate tool for decision support are simulation models of the software life cycle, which also help to understand the dynamics of the software development process. Building up a simulation model requires a mathematical description of the interactions between di.erent objects involved in the development process. Based on experimental data, techniques from the .eld of knowledge discovery can be used to quantify these interactions and to generate new process knowledge based on the analysis of the determined relationships. In this paper blocked neuronal networks and related relevance measures will be presented as an appropriate tool for quanti.cation and validation of qualitatively known dependencies in the software development process.
*Keywords: Blocked Neural Networks, Nonlinear Regression, Knowledge Extraction, Code Inspection*
(21 pages, 2003)

57. H. Knaf, P. Lang, S. Zeiser
***Diagnosis aiding in Regulation Thermography using Fuzzy Logic***
The objective of the present article is to give an overview of an application of Fuzzy Logic in Regulation Thermography, a method of medical diagnosis support. An introduction to this method of the complementary medical science based on temperature measurements – so-called thermograms – is provided. The process of modelling the physician's thermogram evaluation rules using the calculus of Fuzzy Logic is explained.
*Keywords: fuzzy logic,knowledge representation, expert system*
(22 pages, 2003)

58. M.T. Melo, S. Nickel, F. Saldanha da Gama
***Largescale models for dynamic multi-commodity capacitated facility location***
In this paper we focus on the strategic design of supply chain networks. We propose a mathematical modeling framework that captures many practical aspects of network design problems simultaneously but which have not received adequate attention in the literature. The aspects considered include: dynamic planning horizon, generic supply chain network structure, external supply of materials, inventory opportunities for goods, distribution of commodities, facility configuration, availability of capital for investments, and storage limitations. Moreover, network configuration decisions concerning the gradual relocation of facilities over the planning horizon are considered. To cope with fluctuating demands, capacity expansion and reduction scenarios are also analyzed as well as modular capacity shifts. The relation of the proposed modeling framework with existing models is discussed. For problems of reasonable size we report on our computational experience with standard mathematical programming software. In particular, useful insights on the impact of various factors on network design decisions are provided.
*Keywords: supply chain management, strategic planning, dynamic location, modeling*
(40 pages, 2003)

59. J. Orlik
***Homogenization for contact problems with periodically rough surfaces***
We consider the contact of two elastic bodies with rough surfaces at the interface. The size of the micropeaks and valleys is very small compared with the macrosize of the bodies' domains. This makes the direct application of the FEM for the calculation of the contact problem prohibitively costly. A method is developed that allows deriving a macrocontact condition on the interface. The method involves the twoscale asymptotic homogenization procedure that takes into account the microgeometry of the interface layer and the stiffnesses of materials of both domains. The macrocontact condition can then be used in a FEM model for the contact problem on the macrolevel. The averaged contact stiffness obtained allows the replacement of the interface layer in the macromodel by the macrocontact condition.
*Keywords: asymptotic homogenization, contact problems*
(28 pages, 2004)

60. A. Scherrer, K.-H. Küfer, M. Monz, F. Alonso, T. Bortfeld
***IMRT planning on adaptive volume structures – a significant advance of computational complexity***
In intensity-modulated radiotherapy (IMRT) planning the oncologist faces the challenging task of finding a treatment plan that he considers to be an ideal compromise of the inherently contradictive goals of delivering a sufficiently high dose to the target while widely sparing critical structures. The search for this a priori unknown compromise typically requires the computation of several plans, i.e. the solution of several optimization problems. This accumulates to a high computational expense due to the large scale of these problems - a consequence of the discrete problem formulation. This paper presents the adaptive clustering method as a new algorithmic concept to overcome these difficulties. The computations are performed on an individually adapted structure of voxel clusters rather than on the original voxels leading to a decisively reduced computational complexity as numerical examples on real clinical data demonstrate. In contrast to many other similar concepts, the typical trade-off between a reduction in computational complexity and a loss in exactness can be avoided: the adaptive clustering method produces the optimum of the original problem. This flexible method can be applied to both single- and multi-criteria optimization methods based on most of the convex evaluation functions used in practice.
*Keywords: Intensity-modulated radiation therapy (IMRT), inverse treatment planning, adaptive volume structures, hierarchical clustering, local refinement, adaptive clustering, convex programming, mesh generation, multi-grid methods*
(24 pages, 2004)

61. D. Kehrwald
***Parallel lattice Boltzmann simulation of complex flows***
After a short introduction to the basic ideas of lattice Boltzmann methods and a brief description of a modern parallel computer, it is shown how lattice Boltzmann schemes are successfully applied for simulating fluid flow in microstructures and calculating material properties of porous media. It is explained how lattice Boltzmann schemes compute the gradient of the velocity field without numerical differentiation. This feature is then utilised for the simulation of pseudo-plastic fluids, and numerical results are presented for a simple benchmark problem as well as for the simulation of liquid composite moulding.
*Keywords: Lattice Boltzmann methods, parallel computing, microstructure simulation, virtual material design, pseudo-plastic fluids, liquid composite moulding*
(12 pages, 2004)

62. O. Iliev, J. Linn, M. Moog, D. Niedziela, V. Starikovicius
***On the Performance of Certain Iterative Solvers for Coupled Systems Arising in Discretization of Non-Newtonian Flow Equations***
Iterative solution of large scale systems arising after discretization and linearization of the unsteady non-Newtonian Navier–Stokes equations is studied. cross WLF model is used to account for the non-Newtonian behavior of the fluid. Finite volume method is used to discretize the governing system of PDEs. Viscosity is treated explicitely (e.g., it is taken from the previous time step), while other terms are treated implicitly. Different preconditioners (block–diagonal, block–triangular, relaxed incomplete LU factorization, etc.) are used in conjunction with advanced iterative methods, namely, BiCGStab, CGS, GMRES. The action of the preconditioner in fact requires inverting different blocks. For this purpose, in addition to preconditioned BiCGStab, CGS, GMRES, we use also algebraic multigrid method (AMG). The performance of the iterative solvers is studied with respect to the number of unknowns, characteristic velocity in the basic flow, time step, deviation from Newtonian behavior, etc. Results from numerical experiments are presented and discussed.
*Keywords: Performance of iterative solvers, Preconditioners, Non-Newtonian flow*
(17 pages, 2004)

63. R. Ciegis, O. Iliev, S. Rief, K. Steiner
***On Modelling and Simulation of Different Regimes for Liquid Polymer Moulding***
In this paper we consider numerical algorithms for solving a system of nonlinear PDEs arising in modeling of liquid polymer injection. We investigate the particular case when a porous preform is located within the mould, so that the liquid polymer flows through a porous medium during the filling stage. The nonlinearity of the governing system of PDEs is due to the non-Newtonian behavior of the polymer, as well as due to the moving free boundary. The latter is related to the penetration front and a Stefan type problem is formulated to account for it. A finite-volume method is used

to approximate the given differential problem. Results of numerical experiments are presented.
We also solve an inverse problem and present algorithms for the determination of the absolute preform permeability coefficient in the case when the velocity of the penetration front is known from measurements. In both cases (direct and inverse problems) we emphasize on the specifics related to the non-Newtonian behavior of the polymer. For completeness, we discuss also the Newtonian case. Results of some experimental measurements are presented and discussed.
*Keywords: Liquid Polymer Moulding, Modelling, Simulation, Infiltration, Front Propagation, non-Newtonian flow in porous media*
(43 pages, 2004)

64. T. Hanne, H. Neu

***Simulating Human Resources in Software Development Processes***

In this paper, we discuss approaches related to the explicit modeling of human beings in software development processes. While in most older simulation models of software development processes, esp. those of the system dynamics type, humans are only represented as a labor pool, more recent models of the discrete-event simulation type require representations of individual humans. In that case, particularities regarding the person become more relevant. These individual effects are either considered as stochastic variations of productivity, or an explanation is sought based on individual characteristics, such as skills for instance. In this paper, we explore such possibilities by recurring to some basic results in psychology, sociology, and labor science. Various specific models for representing human effects in software process simulation are discussed.
*Keywords: Human resource modeling, software process, productivity, human factors, learning curve*
(14 pages, 2004)

65. O. Iliev, A. Mikelic, P. Popov

***Fluid structure interaction problems in deformable porous media: Toward permeability of deformable porous media***

In this work the problem of fluid flow in deformable porous media is studied. First, the stationary fluid-structure interaction (FSI) problem is formulated in terms of incompressible Newtonian fluid and a linearized elastic solid. The flow is assumed to be characterized by very low Reynolds number and is described by the Stokes equations. The strains in the solid are small allowing for the solid to be described by the Lame equations, but no restrictions are applied on the magnitude of the displacements leading to strongly coupled, nonlinear fluid-structure problem. The FSI problem is then solved numerically by an iterative procedure which solves sequentially fluid and solid subproblems. Each of the two subproblems is discretized by finite elements and the fluid-structure coupling is reduced to an interface boundary condition. Several numerical examples are presented and the results from the numerical computations are used to perform permeability computations for different geometries.
*Keywords: fluid-structure interaction, deformable porous media, upscaling, linear elasticity, stokes, finite elements*
(28 pages, 2004)

66. F. Gaspar, O. Iliev, F. Lisbona, A. Naumovich, P. Vabishchevich

***On numerical solution of 1-D poroelasticity equations in a multilayered domain***

Finite volume discretization of Biot system of poroelasticity in a multilayered domain is presented. Staggered grid is used in order to avoid nonphysical oscillations of the numerical solution, appearing when a collocated grid is used. Various numerical experiments are presented in order to illustrate the accuracy of the finite difference scheme. In the first group of experiments, problems having analytical solutions are solved, and the order of convergence for the velocity, the pressure, the displacements, and the stresses is analyzed. In the second group of experiments numerical solution of real problems is presented.
*Keywords: poroelasticity, multilayered material, finite volume discretization, MAC type grid*
(41 pages, 2004)

67. J. Ohser, K. Schladitz, K. Koch, M. Nöthe

***Diffraction by image processing and its application in materials science***

A spectral theory for constituents of macroscopically homogeneous random microstructures modeled as homogeneous random closed sets is developed and provided with a sound mathematical basis, where the spectrum obtained by Fourier methods corresponds to the angular intensity distribution of x-rays scattered by this constituent. It is shown that the fast Fourier transform applied to three-dimensional images of microstructures obtained by micro-tomography is a powerful tool of image processing. The applicability of this technique is is demonstrated in the analysis of images of porous media.
*Keywords: porous microstructure, image analysis, random set, fast Fourier transform, power spectrum, Bartlett spectrum*
(13 pages, 2004)

68. H. Neunzert

***Mathematics as a Technology: Challenges for the next 10 Years***

No doubt: Mathematics has become a technology in its own right, maybe even a key technology. Technology may be defined as the application of science to the problems of commerce and industry. And science? Science maybe defined as developing, testing and improving models for the prediction of system behavior; the language used to describe these models is mathematics and mathematics provides methods to evaluate these models. Here we are! Why has mathematics become a technology only recently? Since it got a tool, a tool to evaluate complex, "near to reality" models: Computer! The model may be quite old – Navier-Stokes equations describe flow behavior rather well, but to solve these equations for realistic geometry and higher Reynolds numbers with sufficient precision is even for powerful parallel computing a real challenge. Make the models as simple as possible, as complex as necessary – and then evaluate them with the help of efficient and reliable algorithms: These are genuine mathematical tasks.
*Keywords: applied mathematics, technology, modelling, simulation, visualization, optimization, glass processing, spinning processes, fiber-fluid interaction, trubulence effects, topological optimization, multicriteria optimization, Uncertainty and Risk, financial mathematics, Malliavin calculus, Monte-Carlo methods, virtual material design, filtration, bio-informatics, system biology*
(29 pages, 2004)

69. R. Ewing, O. Iliev, R. Lazarov, A. Naumovich

***On convergence of certain finite difference discretizations for 1D poroelasticity interface problems***

Finite difference discretizations of 1D poroelasticity equations with discontinuous coefficients are analyzed. A recently suggested FD discretization of poroelasticity equations with constant coefficients on staggered grid, [5], is used as a basis. A careful treatment of the interfaces leads to harmonic averaging of the discontinuous coefficients. Here, convergence for the pressure and for the displacement is proven in certain norms for the scheme with harmonic averaging (HA). Order of convergence 1.5 is proven for arbitrary located interface, and second order convergence is proven for the case when the interface coincides with a grid node. Furthermore, following the ideas from [3], modified HA discretization are suggested for particular cases. The velocity and the stress are approximated with second order on the interface in this case. It is shown that for wide class of problems, the modified discretization provides better accuracy. Second order convergence for modified scheme is proven for the case when the interface coincides with a displacement grid node. Numerical experiments are presented in order to illustrate our considerations.
*Keywords: poroelasticity, multilayered material, finite volume discretizations, MAC type grid, error estimates*
(26 pages,2004)

70. W. Dörfler, O. Iliev, D. Stoyanov, D. Vassileva

***On Efficient Simulation of Non-Newtonian Flow in Saturated Porous Media with a Multigrid Adaptive Refinement Solver***

Flow of non-Newtonian in saturated porous media can be described by the continuity equation and the generalized Darcy law. Efficient solution of the resulting second order nonlinear elliptic equation is discussed here. The equation is discretized by a finite volume method on a cell-centered grid. Local adaptive refinement of the grid is introduced in order to reduce the number of unknowns. A special implementation approach is used, which allows us to perform unstructured local refinement in conjunction with the finite volume discretization. Two residual based error indicators are exploited in the adaptive refinement criterion. Second order accurate discretization on the interfaces between refined and non-refined subdomains, as well as on the boundaries with Dirichlet boundary condition, are presented here, as an essential part of the accurate and efficient algorithm. A nonlinear full approximation storage multigrid algorithm is developed especially for the above described composite (coarse plus locally refined) grid approach. In particular, second order approximation around interfaces is a result of a quadratic approximation of slave nodes in the multigrid - adaptive refinement (MG-AR) algorithm. Results from numerical solution of various academic and practice-induced problems are presented and the performance of the solver is discussed.
*Keywords: Nonlinear multigrid, adaptive renement, non-Newtonian in porous media*
(25 pages, 2004)

71. J. Kalcsics, S. Nickel, M. Schröder

***Towards a Unified Territory Design Approach – Applications, Algorithms and GIS Integration***

Territory design may be viewed as the problem of grouping small geographic areas into larger geographic clusters called territories in such a way that the latter are acceptable according to relevant planning criteria. In this paper we review the existing literature for applications of territory design problems and solution approaches for solving these types of problems. After identifying features common to all applications we introduce a basic territory design model and present in detail two approaches for solving this model: a classical location–allocation approach combined with optimal split resolution techniques and a newly developed computational geometry based method. We present computational results indicating the efficiency and suitability of the latter method for solving large–scale practical problems in an interactive environment. Furthermore, we discuss extensions to the basic model and its integration into Geographic Information Systems.
*Keywords: territory desgin, political districting, sales territory alignment, optimization algorithms, Geographical Information Systems*
(40 pages, 2005)

72. K. Schladitz, S. Peters, D. Reinel-Bitzer, A. Wiegmann, J. Ohser

***Design of acoustic trim based on geometric modeling and flow simulation for non-woven***

In order to optimize the acoustic properties of a stacked fiber non-woven, the microstructure of the non-woven is modeled by a macroscopically homogeneous random system of straight cylinders (tubes). That is, the fibers are modeled by a spatially stationary random system of lines (Poisson line process), dilated by a sphere. Pressing the non-woven causes anisotropy. In our model, this anisotropy is described by a one parametric distribution of the direction of the fibers. In the present application, the anisotropy parameter has to be estimated from 2d reflected light microscopic images of microsections of the non-woven.
After fitting the model, the flow is computed in digitized realizations of the stochastic geometric model using the lattice Boltzmann method. Based on the flow resistivity, the formulas of Delany and Bazley predict the frequency-dependent acoustic absorption of the non-woven in the impedance tube.

Using the geometric model, the description of a nonwoven with improved acoustic absorption properties is obtained in the following way: First, the fiber thicknesses, porosity and anisotropy of the fiber system are modified. Then the flow and acoustics simulations are performed in the new sample. These two steps are repeatedc for various sets of parameters. Finally, the set of parameters for the geometric model leading to the best acoustic absorption is chosen.
*Keywords: random system of fibers, Poisson line process, flow resistivity, acoustic absorption, Lattice-Boltzmann method, non-woven*
(21 pages, 2005)

73. V. Rutka, A. Wiegmann

### *Explicit Jump Immersed Interface Method for virtual material design of the effective elastic moduli of composite materials*

Virtual material design is the microscopic variation of materials in the computer, followed by the numerical evaluation of the effect of this variation on the material's macroscopic properties. The goal of this procedure is an in some sense improved material. Here, we give examples regarding the dependence of the effective elastic moduli of a composite material on the geometry of the shape of an inclusion. A new approach on how to solve such interface problems avoids mesh generation and gives second order accurate results even in the vicinity of the interface.
The Explicit Jump Immersed Interface Method is a finite difference method for elliptic partial differential equations that works on an equidistant Cartesian grid in spite of non-grid aligned discontinuities in equation parameters and solution. Near discontinuities, the standard finite difference approximations are modified by adding correction terms that involve jumps in the function and its derivatives. This work derives the correction terms for two dimensional linear elasticity with piecewise constant coefficients, i.e. for composite materials. It demonstrates numerically convergence and approximation properties of the method.
*Keywords: virtual material design, explicit jump immersed interface method, effective elastic moduli, composite materials*
(22 pages, 2005)

74. T. Hanne

### *Eine Übersicht zum Scheduling von Baustellen*

Im diesem Dokument werden Aspekte der formalen zeitlichen Planung bzw. des Scheduling für Bauprojekte anhand ausgewählter Literatur diskutiert. Auf allgemeine Aspekte des Scheduling soll dabei nicht eingegangen werden. Hierzu seien als Standard-Referenzen nur Brucker (2004) und Pinedo (1995) genannt. Zu allgemeinen Fragen des Projekt-Managements sei auf Kerzner (2003) verwiesen.
Im Abschnitt 1 werden einige Anforderungen und Besonderheiten der Planung von Baustellen diskutiert. Diese treten allerdings auch in zahlreichen anderen Bereichen der Produktionsplanung und des Projektmanagements auf. In Abschnitt 2 werden dann Aspekte zur Formalisierung von Scheduling-Problemen in der Bauwirtschaft diskutiert, insbesondere Ziele und zu berücksichtigende Restriktionen. Auf eine mathematische Formalisierung wird dabei allerdings verzichtet. Abschnitt 3 bietet eine Übersicht über Verfahren und grundlegende Techniken für die Berechnung von Schedules. In Abschnitt 4 wird ein Überblick über vorhandene Software, zum einen verbreitete Internationale Software, zum anderen deutschsprachige Branchenlösungen, gegeben. Anschließend werden Schlussfolgerungen gezogen und es erfolgt eine Auflistung der Literaturquellen.
*Keywords: Projektplanung, Scheduling, Bauplanung, Bauindustrie*
(32 pages, 2005)

75. J. Linn

### *The Folgar–Tucker Model as a Differential Algebraic System for Fiber Orientation Calculation*

The Folgar–Tucker equation (FTE) is the model most frequently used for the prediction of fiber orientation (FO) in simulations of the injection molding process for short–fiber reinforced thermoplasts. In contrast to its widespread use in injection molding simulations, little is known about the mathematical properties of the FTE: an investigation of e.g. its phase space $M_{FT}$ has been presented only recently [12]. The restriction of the dependent variable of the FTE to the set $M_{FT}$ turns the FTE into a differential algebraic system (DAS), a fact which is commonly neglected when devising numerical schemes for the integration of the FTE. In this article we present some recent results on the problem of trace stability as well as some introductory material which complements our recent paper [12].
*Keywords: fiber orientation, Folgar–Tucker model, invariants, algebraic constraints, phase space, trace stability*
(15 pages, 2005)

76. M. Speckert, K. Dreßler, H. Mauch, A. Lion, G. J. Wierda

### *Simulation eines neuartigen Prüfsystems für Achserprobungen durch MKS-Modellierung einschließlich Regelung*

Testing new suspensions based on real load data is performed on elaborate multi channel test rigs. Usually, wheel forces and moments measured during driving maneuvers are reproduced by the test rig. Because of the complicated interaction between test rig and suspension each new rig configuration has to prove its efficiency with respect to the requirements and the configuration might be subject to optimization.
This paper deals with mathematical and physical modeling of a new concept of a test rig which is based on two hexapods. The model contains the geometric configuration as well as the hydraulics and the controller. It is implemented as an ADAMS/Car template and can be combined with different suspension models to get a complete assembly representing the entire test rig. Using this model, all steps required for a real test run such as controller adaptation, drive file iteration and simulation can be performed. Geometric or hydraulic parameters can be modified easily to improve the setup and adapt the system to the suspension and the given load data.
The model supports and accompanies the introduction of the new rig concept and can be used to prepare real tests on a virtual basis. Using both a front and a rear suspension the approach is described and the potentials coming with the simulation are pointed out.
*Keywords: virtual test rig, suspension testing, multibody simulation, modeling hexapod test rig, optimization of test rig configuration*
(20 pages, 2005)
In deutscher Sprache; bereits erschienen in: VDI-Berichte Nr. 1900, VDI-Verlag GmbH Düsseldorf (2005), Seiten 227-246

77. K.-H. Küfer, M. Monz, A. Scherrer, P. Süss, F. Alonso, A.S.A. Sultan, Th. Bortfeld, D. Craft, Chr. Thieke

### *Multicriteria optimization in intensity modulated radiotherapy planning*

Inverse treatment planning of intensity modulated radiothrapy is a multicriteria optimization problem: planners have to find optimal compromises between a sufficiently highdose intumor tissuethat garantuee a high tumor control, and, dangerous overdosing of critical structures, in order to avoid high normal tissue complcication problems.
The approach presented in this work demonstrates how to state a flexible generic multicriteria model of the IMRT planning problem and how to produce clinically highly relevant Pareto-solutions. The model is imbedded in a principal concept of Reverse Engineering, a general optimization paradigm for design problems. Relevant parts of the Pareto-set are approximated by using extreme compromises as cornerstone solutions, a concept that is always feasible if box constraints for objective funtions are available. A major practical drawback of generic multicriteria concepts trying to compute or approximate parts of the Pareto-set is the high computational effort. This problem can be overcome by exploitation of an inherent asymmetry of the IMRT planning problem and an adaptive approximation scheme for optimal solutions based on an adaptive clustering preprocessing technique. Finally, a coherent approach for calculating and selecting solutions in a real-timeinteractive decision-making process is presented. The paper is concluded with clinical examples and a discussion of ongoing research topics.
*Keywords: multicriteria optimization, extreme solutions, real-time decision making, adaptive approximation schemes, clustering methods, IMRT planning, reverse engineering*
(51 pages, 2005)

78. S. Amstutz, H. Andrä

### *A new algorithm for topology optimization using a level-set method*

The levelset method has been recently introduced in the field of shape optimization, enabling a smooth representation of the boundaries on a fixed mesh and therefore leading to fast numerical algorithms. However, most of these algorithms use a HamiltonJacobi equation to connect the evolution of the levelset function with the deformation of the contours, and consequently they cannot create any new holes in the domain (at least in 2D). In this work, we propose an evolution equation for the levelset function based on a generalization of the concept of topological gradient. This results in a new algorithm allowing for all kinds of topology changes.
*Keywords: shape optimization, topology optimization, topological sensitivity, level-set*
(22 pages, 2005)

79. N. Ettrich

### *Generation of surface elevation models for urban drainage simulation*

Traditional methods fail for the purpose of simulating the complete flow process in urban areas as a consequence of heavy rainfall and as required by the European Standard EN-752 since the bi-directional coupling between sewer and surface is not properly handled. The methodology, developed in the BMBF/EUREKA-project RisUrSim, solves this problem by carrying out the runoff on the basis of shallow water equations solved on high-resolution surface grids. Exchange nodes between the sewer and the surface, like inlets and manholes, are located in the computational grid and water leaving the sewer in case of surcharge is further distributed on the surface.
So far, it has been a problem to get the dense topographical information needed to build models suitable for hydrodynamic runoff calculation in urban areas. Recent airborne data collection methods like laser scanning, however, offer a great chance to economically gather densely sampled input data. This paper studies the potential of such laser-scan data sets for urban water hydrodynamics.
*Keywords: Flooding, simulation, urban elevation models, laser scanning*
(22 pages, 2005)

80. H. Andrä, J. Linn, I. Matei, I. Shklyar, K. Steiner, E. Teichmann

### *OPTCAST – Entwicklung adäquater Strukturoptimierungsverfahren für Gießereien Technischer Bericht (KURZFASSUNG)*

Im vorliegenden Bericht werden die Erfahrungen und Ergebnisse aus dem Projekt OptCast zusammengestellt. Das Ziel dieses Projekts bestand (a) in der Anpassung der Methodik der automatischen Strukturoptimierung für Gussteile und (b) in der Entwicklung und Bereitstellung von gießereispezifischen Optimierungstools für Gießereien und Ingenieurbüros.
Gießtechnische Restriktionen lassen sich nicht auf geometrische Restriktionen reduzieren, sondern sind nur über eine Gießsimulation (Erstarrungssimulation und Eigenspannungsanalyse) adäquat erfassbar, da die lokalen Materialeigenschaften des Gussteils nicht nur von der geometrischen Form des Teils, sondern auch vom verwendeten Material abhängen. Wegen dieser Erkenntnis wurde ein neuartiges iteratives Topologieoptimierungsverfahren unter Verwendung der Level-Set-Technik entwickelt, bei dem keine variable Dichte des Materials eingeführt wird. In jeder Iteration wird ein scharfer Rand des Bauteils berechnet. Somit ist die Gießsimulation in den iterativen Optimierungsprozess integrierbar.
Der Bericht ist wie folgt aufgebaut: In Abschnitt 2 wird der Anforderungskatalog erläutert, der sich aus der Bearbeitung von Benchmark-Problemen in der ersten Projektphase ergab. In Abschnitt 3 werden die Benchmark-Probleme und deren Lösung mit den im Projekt

entwickelten Tools beschrieben. Abschnitt 4 enthält die Beschreibung der neu entwickelten Schnittstellen und die mathematische Formulierung des Topologieoptimierungsproblems. Im letzten Abschnitt wird das neue Topologieoptimierungsverfahren, das die Simulation des Gießprozesses einschließt, erläutert.
*Keywords: Topologieoptimierung, Level-Set-Methode, Gießprozesssimulation, Gießtechnische Restriktionen, CAE-Kette zur Strukturoptimierung*
(77 pages, 2005)

81. N. Marheineke, R. Wegener

***Fiber Dynamics in Turbulent Flows***
***Part I: General Modeling Framework***

The paper at hand deals with the modeling of turbulence effects on the dynamics of a long slender elastic fiber. Independent of the choice of the drag model, a general aerodynamic force concept is derived on the basis of the velocity field for the randomly fluctuating component of the flow. Its construction as centered differentiable Gaussian field complies thereby with the requirements of the stochastic k-ε turbulence model and Kolmogorov's universal equilibrium theory on local isotropy.
*Keywords: fiber-fluid interaction; Cosserat rod; turbulence modeling; Kolmogorov's energy spectrum; double-velocity correlations; differentiable Gaussian fields*

***Part II: Specific Taylor Drag***

In [12], an aerodynamic force concept for a general air drag model is derived on top of a stochastic k-ε description for a turbulent flow field. The turbulence effects on the dynamics of a long slender elastic fiber are particularly modeled by a correlated random Gaussian force and in its asymptotic limit on a macroscopic fiber scale by Gaussian white noise with flow-dependent amplitude. The paper at hand now presents quantitative similarity estimates and numerical comparisons for the concrete choice of a Taylor drag model in a given application.
*Keywords: flexible fibers; k-ε turbulence model; fiber-turbulence interaction scales; air drag; random Gaussian aerodynamic force; white noise; stochastic differential equations; ARMA process*
(38 pages, 2005)

Status quo: September 2005